AD-A063 080 ARMY ENGINEER WATERWAYS EXPERIMENT STATION VICKSBURG MISS F/G 20/4
NUMERICAL SIMULATION OF TIDAL HYDRODYNAMICS, GREAT EGG HARBOR A--ETC(U)
JUN 78 H L BUTLER

UNCLASSIFIED WES-TR-H-78-11 NL

1 OF 2
AD
AD63080

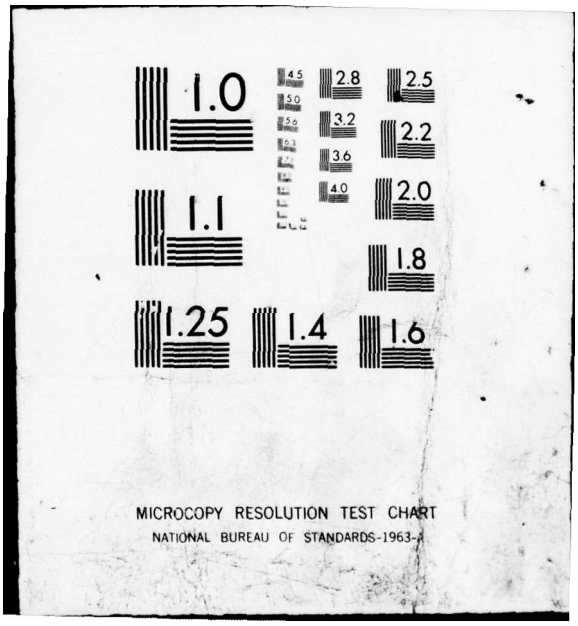
1.0
1.1
1.25
1.4
1.6
1.8
2.0
2.2
2.5
2.8
3.2
3.6
4.0
4.5
5.0
5.6
6.3
MICROCOPY RESOLUTION TEST CHART
NATIONAL BUREAU OF STANDARDS-1963-A

LEVEL II

12

NW

TECHNICAL REPORT H-78-11

NUMERICAL SIMULATION OF TIDAL HYDRODYNAMICS, GREAT EGG HARBOR AND CORSON INLETS, NEW JERSEY

by

H. Lee Butler

Hydraulics Laboratory
U. S. Army Engineer Waterways Experiment Station
P. O. Box 631, Vicksburg, Miss. 39180

June 1978
Final Report

Prepared for U. S. Army Engineer District, Philadelphia
Philadelphia, Pennsylvania 19106

Destroy this report when no longer needed. Do not return it to the originator.

Unclassified

SECURITY CLASSIFICATION OF THIS PAGE (When Data Entered)

REPORT DOCUMENTATION PAGE

READ INSTRUCTIONS BEFORE COMPLETING FORM

1. REPORT NUMBER: Technical Report H-78-11

2. GOVT ACCESSION NO.

3. RECIPIENT'S CATALOG NUMBER

4. TITLE (and Subtitle): NUMERICAL SIMULATION OF TIDAL HYDRODYNAMICS, GREAT EGG HARBOR AND CORSON INLETS, NEW JERSEY.

5. TYPE OF REPORT & PERIOD COVERED: Final report, Mar 75 - Jan 77

6. PERFORMING ORG. REPORT NUMBER

7. AUTHOR(s): H. Lee Butler

8. CONTRACT OR GRANT NUMBER(s)

9. PERFORMING ORGANIZATION NAME AND ADDRESS
U. S. Army Engineer Waterways Experiment Station
Hydraulics Laboratory
P. O. Box 631, Vicksburg, Mississippi 39180

10. PROGRAM ELEMENT, PROJECT, TASK AREA & WORK UNIT NUMBERS

11. CONTROLLING OFFICE NAME AND ADDRESS
U. S. Army Engineer District, Philadelphia
U. S. Custom House, 2nd and Chestnut Street
Philadelphia, Pennsylvania 19106

12. REPORT DATE: June 1978

13. NUMBER OF PAGES: 138

14. MONITORING AGENCY NAME & ADDRESS (if different from Controlling Office)
141p.

15. SECURITY CLASS. (of this report): Unclassified

15a. DECLASSIFICATION/DOWNGRADING SCHEDULE

16. DISTRIBUTION STATEMENT (of this Report)

Approved for public release; distribution unlimited.
WES-TR-H-78-11

17. DISTRIBUTION STATEMENT (of the abstract entered in Block 20, if different from Report)

18. SUPPLEMENTARY NOTES

Appendix E was reproduced in microfiche and is enclosed in an envelope on the back cover of this report.

19. KEY WORDS (Continue on reverse side if necessary and identify by block number)

Corson Inlet	Hydrodynamics	Navigation conditions
Erosion	Inlets (Waterways)	Numerical simulation
Finite difference method	Mathematical models	Tidal hydraulics
Great Egg Harbor Inlet	Navigation channels	Tidal models

20. ABSTRACT (Continue on reverse side if necessary and identify by block number)

Great Egg Harbor Inlet and Corson Inlet, located in southeast New Jersey, have been plagued with hazardous navigation conditions and erosion problems. Numerical techniques were used to investigate the tidal hydrodynamics of the inlet complexes for existing conditions as well as for proposed improvement plans. The physical size and complex geometry of the study areas required a simulation model that could be economically applied. Consequently, an inherent part of the study involved development of a numerical model (WI model) based

(Continued)

DD FORM 1 JAN 73 1473 EDITION OF 1 NOV 65 IS OBSOLETE

Unclassified

SECURITY CLASSIFICATION OF THIS PAGE (When Data Entered)

038 100

LB

79 01 09 042

20. ABSTRACT (Continued)

on an implicit finite difference formulation. The model includes treatment of moving boundaries and subgrid-scale barriers. A comparison study with a well-known explicit finite difference tidal model was performed to assure the implicit model's reliability and cost effectiveness. Having demonstrated the WI model capability, the next phase of the study concerned application of the WI model to Great Egg Harbor and Corson Inlets to quantitatively predict the tidal hydrodynamics (exclusive of salt and sediment transport) for existing conditions and various improvement plans. The basic improvements for each inlet are similar. In general, they provide for:

a. An upcoast jetty with a weir section for navigation protection and beach erosion control. Bayward of the weir section a deposition basin would be dredged to impound sand transported across the weir section. Periodic maintenance dredging of the deposition basin would provide sand for nourishment of adjacent beaches.

b. Construction and maintenance of specified navigation channels.

c. A downcoast bulkhead and jetty system together with an optional development of landfill area adjacent to the bulkhead for public recreational use.

Results of the numerical computations indicated that the systems proposed for Corson Inlet appear to function equally well and no detrimental effects were noted. For Great Egg Harbor Inlet, a concentration of ebb flow toward the upcoast deposition basin and structure was noted, suggesting a potential problem which should be recognized for the proposed plans. Time histories of tide elevations and velocities are presented for selected stations throughout each inlet complex. Circulation patterns at each half hour during a complete tidal cycle are presented in film form for the verification conditions and for each plan.

PREFACE

The numerical model investigation described herein was authorized by the U. S. Army Engineer District, Philadelphia, on 19 February 1975. This study was conducted at the U. S. Army Engineer Waterways Experiment Station (WES) during the period March 1975 to January 1977 in the Wave Dynamics Division (WDD), Hydraulics Laboratory, under the direction of Mr. H. B. Simmons, Chief of the Hydraulics Laboratory, and Dr. R. W. Whalin, Chief of the Wave Dynamics Division.

The investigation was performed and this report prepared by Mr. H. Lee Butler, WDD. A significant contribution to the study was made by Dr. Donald C. Raney, Professor of Engineering Mechanics at the University of Alabama, assigned to WES under terms of the Intergovernmental Personnel Exchange Act. The numerical computations associated with this work were performed on Control Data 6600 and 7600 computers located at the Los Alamos Scientific Laboratory, Los Alamos, New Mexico, through the cooperation of C-Division.

Directors of WES during the course of the investigation and the preparation and publication of this report were COL G. H. Hilt, CE, and COL John L. Cannon, CE. Technical Director was Mr. F. R. Brown.

CONTENTS

CONTENTS

There is no hard copy or Xerox copy of

Appendix E that we can furnish DDC.

CONVERSION FACTORS, U. S. CUSTOMARY TO METRIC (SI) UNITS OF MEASUREMENT

U. S. customary units of measurement used in this report can be converted to metric (SI) units as follows:

Multiply	By	To Obtain
feet	0.3048	metres
miles (U. S. statute)	1.609344	kilometres
cubic feet	0.02831685	cubic metres
feet per second	0.3048	metres per second
square miles (U. S. statute)	2.589988	square kilometres
square feet per second	0.09290304	square metres per second
acres	4046.856	square metres
feet per second per second	0.3048	metres per second per second

NUMERICAL SIMULATION OF TIDAL HYDRODYNAMICS GREAT EGG HARBOR AND CORSON INLETS, NEW JERSEY

PART I: INTRODUCTION

Background

1. Great Egg Harbor Inlet and Corson Inlet (GECI) are natural inlets located in southeast New Jersey (Figure 1) between Absecon Island and Ludlam Beach. The inlets are located in areas where commercial and recreational fishing as well as resort activities are an important part of the economy. Both inlet systems are characterized by large areas of marshland which restrict the flow to a complex system of channels. The Corson back bay area contains two large bodies of water, Ludlam Bay and the very shallow Corson Sound. The southwest portion of the Great Egg complex is characterized primarily by two large water bodies, Great Egg Harbor Bay and Peck Bay. Great Egg Harbor Inlet system joins Absecon Inlet system in the north and Corson Inlet system in the south through a single channel at Roosevelt Bridge. Some freshwater inflow enters the Great Egg system from the west through Great Egg Harbor Bay. Corson Inlet system joins Townsends Inlet system in the south through a single channel at Sea Isle City.

2. Some of the problems which affect the inlet complex are: hazardous navigation conditions, inlet instability, shoal conditions within inlet vicinity, erosion of recreational and protective beaches, and tidal flooding of oceanfront property. To reduce these problems, modifications to Great Egg Harbor and Corson Inlets were proposed in 1966 by the U. S. Army Engineer District, Philadelphia (NAPEN), and subsequently authorized by Congress in 1970. Detailed development of plans to improve the existing conditions at GECI was deferred until completion of this investigation to study the tidal hydrodynamics of existing conditions as well as plans of improvement for each inlet. Improvement plans to be investigated consist of the installation of some type of dual jetty system, including a low-level weir on one jetty, deposition basin, and channel dredging.

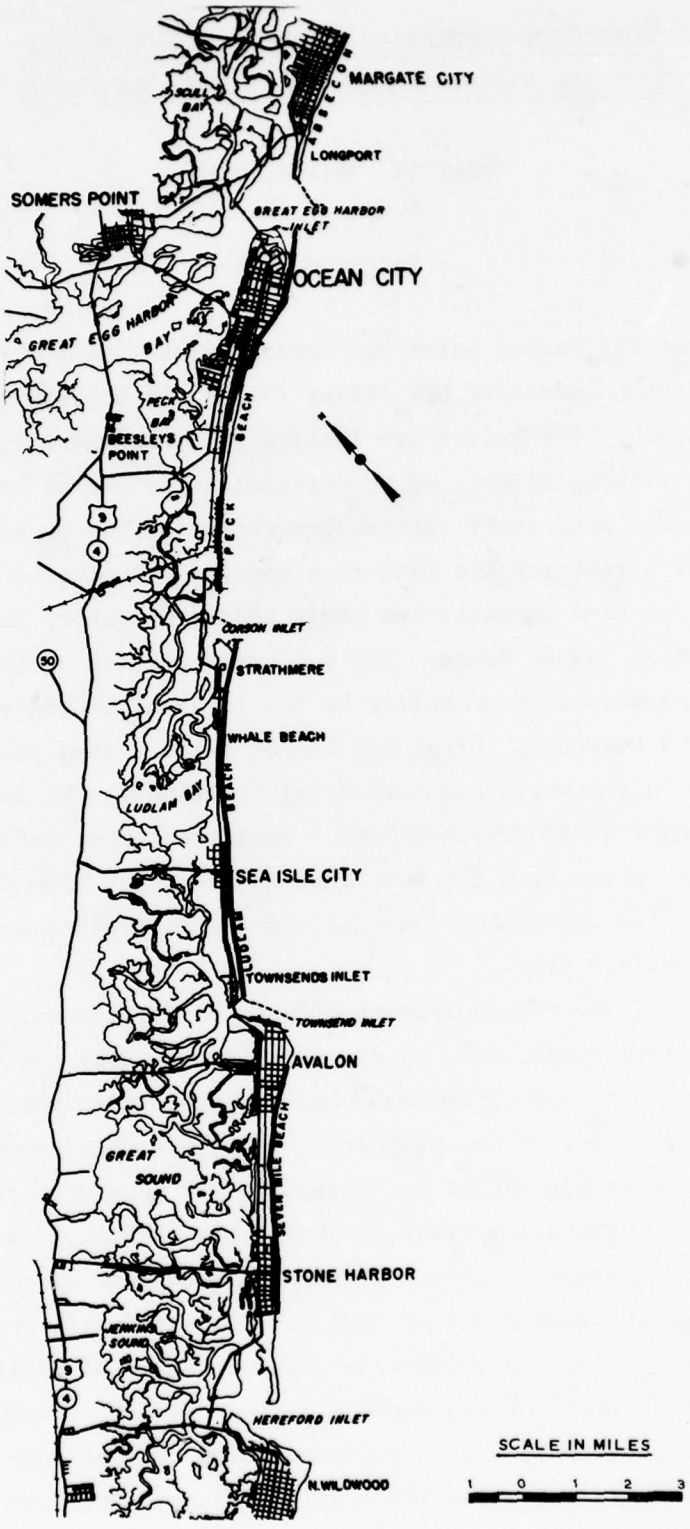

Figure 1. Location of GECI area in southeast New Jersey

3. This study was funded by NAPEN to aid in evaluating proposed modifications. Plans of improvement for New Jersey inlets and beaches were presented by NAPEN in a Navigation and Cooperative Beach Erosion Control Study.[1] No investigative action was taken until a request was made of the U. S. Army Engineer Waterways Experiment Station (WES) in 1973 to provide cost and time estimates for a physical model study of GECI. A meeting between all offices concerned was held to fully explore the problem and issue guidance on a feasible study plan. As a result NAPEN requested a numerical model investigation of the GECI area in order to ascertain tidal hydrodynamic evaluations of the various proposed plans.

4. The first major problem encountered in any numerical simulation study is the selection or development of an algorithm, which is not only capable of simulating the problem under study but can also be economically applied. Most numerical simulations of tidal hydrodynamics associated with inlets and bays have been performed using explicit finite difference models. An explicit scheme is one in which the solution of the difference equation at a given time depends solely on information computed in previous time steps.

5. The first computer code widely recognized for treating such problems used an explicit scheme. The code was developed by Reid and Bodine[2] (termed the RB model) and was used extensively in simulations which include subgrid topographic features and possible flooding of low-lying areas. An extension of Reid and Bodine's work was carried out by Masch, Brandes, and Reagan[3] to help evaluate the degree to which mathematical models can be used to predict the tidal hydrodynamics of an inlet system. A suggestion was made by NAPEN to apply Masch's model to the GECI area; however, past experience within the Wave Dynamics Division (WDD) of WES had shown that explicit models, in many instances, are economically infeasible to apply to real-world engineering problems covering large areas due to stringent stability criteria limiting the calculation time step. In contrast to an explicit scheme, an implicit finite difference formulation is usually not restricted by an associated stability criterion. For an implicit formulation, the solution at a

given point within the study area depends upon unknown values at neighboring points in the grid system as well as upon values computed in previous time steps.

6. Implicit schemes have been applied by WDD to a variety of problems such as tsunami propagation, simplified tidal models, landslide-generated water waves, and storm surge calculations summarized by Butler and Durham.[4] Implicit formulations were used by Leendertse[5,6] in treating problems which included low-lying areas that are inundated only during a portion of the tidal cycle. The principle reason for choosing an implicit formulation is one of economics. A significantly larger time step than in an explicit scheme is used in the calculations since the time and spatial increments are chosen to meet required accuracy in representing topographic features and external forcing functions.

7. For proper application of a numerical scheme to areas as large as either inlet system in the GECI area, an implicit model was deemed essential. Since there were no implicit codes available in the literature which could simulate flooding of low-lying terrain and internal barriers, such as dikes, jettys, weir sections, and similar features, the development of such a code (WES implicit code or WI model) within the scope of this project was considered necessary and was included as an intrinsic element in the study. In order to evaluate the WI model, a comparison study was designed to check its reliability. Both the Masch version of the RB model and the WI model were applied to the Masonboro Inlet area using identical grids, bottom topography, and boundary conditions. Having concluded from the results of this comparison study that the WI model was reliable and economically feasible to apply to a large inlet system, the WI code was selected for application to the GECI area.

Objectives

8. The primary objective of this project was to apply a numerical model to Great Egg Harbor and Corson Inlets, N. J., to predict quantitatively the hydrodynamics (exclusive of salt and sediment transport and

wave action) of the tidal flow through each inlet for various improvement schemes. Having chosen the WI model for application to GECI, the following tasks were accomplished:

a. The WI model was calibrated for existing conditions at each inlet. Tidal elevations and current velocities were calculated and verified by comparison with prototype data collected by the staff at Rutgers University.[7]

b. The calibrated model was applied to various modified conditions at each inlet to predict tides and currents at selected stations. Comparisons are made to indicate the effects of each improvement plan.

In addition, this report includes a discussion of the development of the WI model and a presentation of the comparison study made for the Masonboro Inlet application.

PART II: BASIC EQUATIONS OF FLUID FLOW

Equations of Motion

9. The hydrodynamic equations used in this work are derived from the classical three-dimensional Navier-Stokes equations for an incompressible fluid. The details of the derivation can be found in Dronkers[8] or Leendertse[9] and are not repeated here. By assuming the vertical accelerations are small and the fluid is well mixed, and integrating the flow from the sea bottom to the water surface, the normal two-dimensional depth-averaged form of the equations of momentum and continuity are obtained. Expressed in a Cartesian coordinate system (Figure 2) the integrated equations of motion are given as

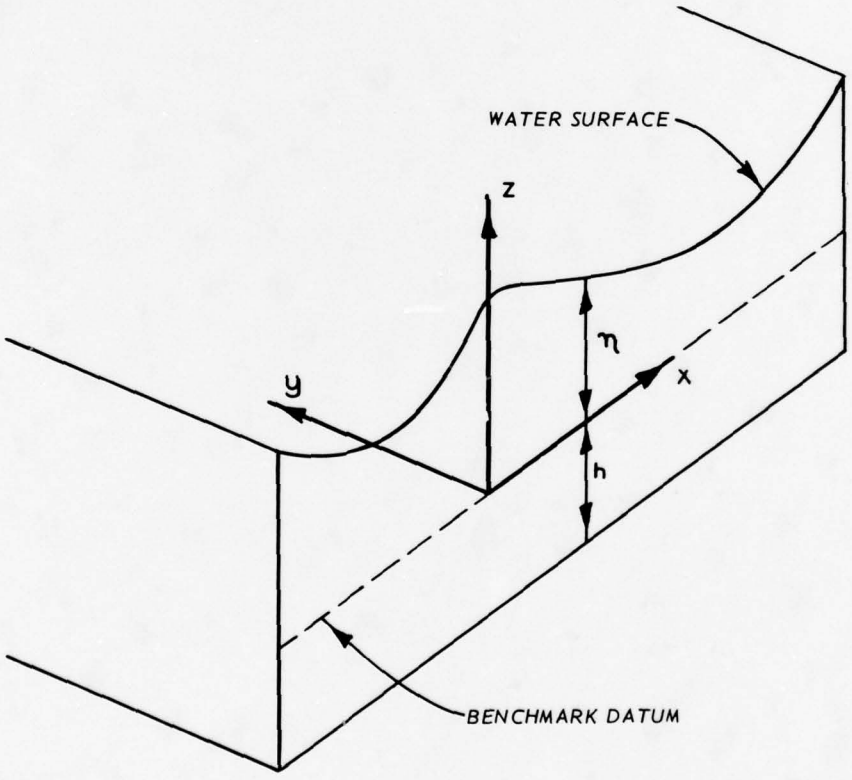

Figure 2. Coordinate system for problem formulation

MOMENTUM

$$\frac{\partial U}{\partial t} + \frac{U}{d}\frac{\partial U}{\partial x} + \frac{V}{d}\frac{\partial U}{\partial y} - fV + gd\frac{\partial \eta}{\partial x} = \frac{-gU}{C^2 d^2}(U^2 + V^2)^{1/2} + F_x \quad (1)$$

$$\frac{\partial V}{\partial t} + \frac{U}{d}\frac{\partial V}{\partial x} + \frac{V}{d}\frac{\partial V}{\partial y} + fU + gd\frac{\partial \eta}{\partial y} = \frac{-gV}{C^2 d^2}(U^2 + V^2)^{1/2} + F_y \quad (2)$$

CONTINUITY

$$\frac{\partial \eta}{\partial t} + \frac{\partial U}{\partial x} + \frac{\partial V}{\partial y} = \xi \quad (3)$$

In these equations U and V are the vertically integrated transports per unit of width (flows) at time t in the x and y directions, respectively; η is the water-surface elevation with respect to the given datum; $d = \eta - h$ is the water depth at (x,y,t); h is the land-surface elevation at (x,y); f is the Coriolis parameter; C is the Chezy frictional coefficient; F_x and F_y are terms representing external forcing functions such as wind effects; g is the acceleration due to gravity; and ξ is a term representing the rate at which additional water is introduced into or taken from the system (for example, through rainfall and evaporation).* The approach used in this model differs from that of Leendertse in that the equations of motion are formulated in terms of flows rather than velocities. In addition, the schemes for handling the flood-dry procedures and subgrid barriers are unique. It should also be pointed out that the convective terms of the form $\frac{U}{d}\frac{\partial U}{\partial x}$ as written are only approximate. A complete derivation of the equations can be found in Wang and Connor.[10] The complete form of the convective terms is significantly more difficult to treat numerically. Numerical tests were carried out using the complete form, and

---

* For convenience, symbols and unusual abbreviations are listed and defined in the Notation (Appendix D).

negligible differences were noted for the types of applications discussed in this report.

Numerical Approach

10. The basic equations of motion (1, 2, and 3) are nonlinear partial differential equations. A typical study region possesses a highly complex geometry and variable boundary conditions exist throughout the system. These features of the problem make a purely analytical approach intractable. In developing a numerical scheme for solving the problem, the differential expressions are replaced with finite difference expressions to operate in spatial and time coordinates on specific points of a grid system. If the grid size approaches zero, the solution of the difference equations must converge to that of the differential equations. The numerical solution schemes presented in the following section satisfy the convergence criteria. Details on questions of convergence and stability can be found in references cited in this report.

11. Two forms of finite difference solutions to the equations of fluid motion are considered: an explicit and an implicit formulation. The same space-staggered computational grid is used in both formulations. A rectilinear mesh is placed over the study area where Δx is the height of a grid cell and Δy is the width. Within each cell, the following assumptions are made: (a) the value of η is considered to be an average over a grid cell centered at $x = M\Delta x$ and $y = N\Delta y$ and at time $t = k\Delta t$; (b) the value of $U_{N,M}$ is given at the center of the lower cell face; and (c) the value of $V_{N,M}$ is given at the center of the right-hand cell face (Figure 3). In addition, the water depth and frictional coefficient (Manning's n or Chezy coefficient C) are also defined at the center of grid cells.

12. The following notations are used in approximating the equations of motion by a system of difference equations.

Functional: $U^{k}_{N,M} = U(M\Delta x, N\Delta y, k\Delta t);\ \Delta x = \Delta y = \Delta$

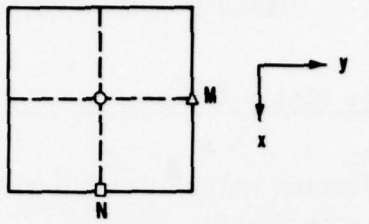

□ — FLOW/UNIT WIDTH IN X-DIRECTION (U)

△ — FLOW/UNIT WIDTH IN Y-DIRECTION (V)

○ — SURFACE ELEVATION (η), WATER DEPTH (d), FRICTIONAL COEFFICIENT (C or n)

Figure 3. Cell definition

Time Differential: $$\frac{\partial U}{\partial t} \rightarrow \frac{U^{k+1/2} - U^{k-1/2}}{\Delta t} \quad \text{at } (N, M, + 1/2)$$

Spatial Differential: $$\frac{\partial U}{\partial t} \rightarrow \left\langle \frac{\partial U}{\partial x} \right\rangle_1 \text{ or } \left\langle \frac{\partial U}{\partial x} \right\rangle_2$$

Average Terms: $$\overline{U}_{N+1/2,M} = U_{N,M+1/2} + U_{N-1,\ M+1/2} + U_{N,M-1/2} + U_{N-1,M-1/2}$$

Angle brackets, $\langle\ \rangle_1$ or $\langle\ \rangle_2$, are used to indicate that terms maintained in differential form are evaluated with centered difference expressions over one or two grid cells, respectively.

PART III: COMPUTATIONAL TECHNIQUES

Explicit Finite Difference Solution

13. The explicit solution method used in the RB model is a time-centered difference scheme involving a procedure of the "leap frog" type for computation of flow and water levels. Using the notations given in the previous section and applying centered differences in time and space, $U^{k+1/2}$, $V^{k+1/2}$, η^{k+1} can be expressed explicitly in terms of functional values calculated at previous time levels. An abbreviated form of the system of difference equations for the RB code can be written as:

MOMENTUM

$$U^{k+1/2} = \left[U^{k-1/2} - \Delta t \frac{\bar{V}^{k-1/2}}{d^*} \left\langle \frac{\partial U}{\partial y} \right\rangle_2^{k-1/2} + \Delta t f \bar{V}^{k-1/2} \right. \tag{4}$$

$$\left. - \Delta t g d^* \left\langle \frac{\partial \eta}{\partial x} \right\rangle_1^k + \Delta t F_x^k \right] \Big/ C_{fx} \text{ AT } (N, M + 1/2)$$

$$V^{k+1/2} = \left[V^{k-1/2} - \Delta t \frac{\bar{U}^{k-1/2}}{d^*} \left\langle \frac{\partial V}{\partial x} \right\rangle_2^{k-1/2} + \Delta t f \bar{U}^{k-1/2} \right. \tag{5}$$

$$\left. - \Delta t g d^* \left\langle \frac{\partial \eta}{\partial y} \right\rangle_1^k + \Delta t F_y^k \right] \Big/ C_{fy} \text{ AT } (N + 1/2, M)$$

WHERE

$$C_{fx} = 1 + \frac{\Delta t}{d^*} \left\langle \frac{\partial U}{\partial x} \right\rangle_2^{k-1/2} + \frac{g n_x^2 \Delta t}{2.21 (d^*)^{4/3}} W_x \tag{6}$$

$$W_x = \left[(U^{k-1/2})^2 + (\bar{V}^{k-1/2})^2 \right]^{1/2} \Big/ d^* \tag{7}$$

$$C_{fy} = 1 + \frac{\Delta t}{d^*} \left\langle \frac{\partial V}{\partial y} \right\rangle_2^{k-1/2} + \frac{g n_y^2 \Delta t}{2.21 (d^*)^{4/3}} W_y \tag{8}$$

$$W_y = \left[(\bar{U}^{k-1/2})^2 + (V^{k-1/2})^2 \right]^{1/2} \Big/ d^* \tag{9}$$

$$d^* = \bar{\eta}^k - \bar{h} \tag{10}$$

CONTINUITY

$$\eta^{k+1} = \eta^k - \Delta t \left[\left\langle \frac{\partial U}{\partial x} \right\rangle_1^{k+1/2} + \left\langle \frac{\partial V}{\partial y} \right\rangle_1^{k+1/2} - \xi^k \right] \tag{11}$$

AT (N, M)

14. The calculations for each time step are divided into two halves: the flows are computed during the first half of the time step and the results are used in the continuity equation to calculate the surface elevations during the second half of the time step. It should be emphasized that the computed flows and water levels are determined one-half time step apart, yet the results are given only at even time levels.

15. The equations presented above are applicable for cells surrounded by free flowing water on all four sides (open cells). However, some boundary conditions within the system may force different approximations to be used for terms such as the advective cross-product terms (e.g., $U\frac{\partial U}{\partial x}$). A detailed discussion of the explicit scheme can be found in Masch, et al.[3] and will not be presented here.

Implicit Finite Difference Solution

16. To solve the governing equations implicitly, the same space-staggered scheme is used. The implicit code employs an alternating-direction technique where calculations are divided into two parts. The first step, or 1/2 cycle, consists in solving for η and U implicitly; the second 1/2 cycle computes η and V implicitly. The omitted transport in each 1/2 cycle is assumed constant for that step. Applying a centered difference operator to the momentum Equation 1, and the continuity Equation 3, along a grid line parallel to the x-axis, results in a system of linear algebraic equations whose coefficient matrix is tridiagonal. The form of the equations for the first 1/2 cycle is given by:

MOMENTUM

$$U^{k+1/2} = U^{k-1/2} + \Delta t\left[f\bar{V}^{k} - \frac{U^{k+1/2}}{d^*}\left\langle\frac{\partial U}{\partial x}\right\rangle_2^{k-1/2} + F_x{}^{k} - \frac{\bar{V}^{k}}{d^*}\left\langle\frac{\partial U}{\partial y}\right\rangle_2^{k-1/2} - gd^*\left\{\frac{\left\langle\frac{\partial \eta}{\partial x}\right\rangle_1^{k+1/2} + \left\langle\frac{\partial \eta}{\partial x}\right\rangle_1^{k-1/2}}{2} + \frac{U^{k+1/2} + U^{k-1/2}}{2(\bar{C}^{k})^2\,(d^*)^3}\left((U^{k-1/2})^2 + (\bar{V}^{k})^2\right)^{1/2}\right\}\right] \quad (12)$$

AT (N, M + 1/2)

CONTINUITY

$$\eta^{k+1/2} = \eta^{k} - \frac{\Delta t}{2}\left[\left\langle\frac{\partial U}{\partial x}\right\rangle_1^{k+1/2} + \left\langle\frac{\partial V}{\partial y}\right\rangle_1^{k}\right] + \frac{\Delta t}{2}\,\xi^{k} \tag{13}$$

AT (N, M)

WHERE $d^* = \bar{\eta}^{k} - \bar{h}$ (14)

The equations for the second 1/2 cycle are similar to those above and are not presented.

17. In this numerical scheme the surface elevations are computed twice within each complete time step; the flows are computed once. Again, these equations are applicable only for open cells. Various approximations must be introduced where boundaries occur. A complete presentation of the difference equations and method of solution is given in Appendix A.

Boundary Conditions

18. Various types of boundary conditions are permissible in the present system of computation for both explicit and implicit codes. In both codes, boundary conditions at the tide computation boundary (open boundary conditions) are accomplished by setting the water levels $\eta_{N,M}$ as prescribed by input tables. Flow rates may be specified instead of water levels. All additional boundary conditions relate the normal component of flow at the boundary to the state of the water level at the boundary. These conditions may be grouped into two classifications: water-land boundaries and subgrid barriers.

Water-land boundaries

19. Such boundaries are prescribed along cell faces, hence this condition is handled by specifying $U = 0$ or $V = 0$ for those cells when impermeable boundaries exist. In estuarine systems with large areas of low-lying terrain and a significant tidal range, many areas alternately dry and flood within each tidal cycle. The behavior is simulated by making the location of the land-water boundary a function

of the current value of the total water depth. By checking the water level in adjacent cells relative to the ground elevation, a determination is made as to the possibility of inundation. If flooding is possible, the boundary face is treated as open and computations for η, U, and V are made for that cell. The drying of cells is simply the inverse process.

Subgrid barriers

20. Subgrid barriers are defined along cell faces and are of three types: exposed, submerged, and overtopping. One characteristic of such barriers is that the surface elevation is computed at the center of the cells on either side of the barriers. A detailed treatment of these barriers in the explicit code can be found in Masch, et al.[3] The following discussion is limited to the way in which these conditions are simulated in the implicit code. Exposed barriers are handled by simply specifying a no-flow condition across the cell face. This type of barrier is used to describe dikes, jetties, and similar features which are impermeable and usually of a width much less than one half the spatial grid step. Submerged barriers are used to simulate flows across such barriers as submerged reefs, dredged material disposal banks, pipelines, etc. The water level on each side of a submerged barrier must always exceed the barrier crest elevation. The flow over a submerged barrier can be controlled in a manner similar to that used by Masch but experience has shown that by defining a special Chezy coefficient for the barrier face, the flow over the barrier can be simulated without introducing unwanted transients.

21. Overtopping barrier is a terminology used to distinguish a barrier which can be submerged during one portion of the tidal cycle and totally exposed in another. Masch used a broadcrested weir formula to describe the overtopping nature of the flow and then the submerged weir formula when appropriate. Since a larger time step is used in the implicit code and the duration time of overtopping is short, a Chezy formulation is again used to simulate the flow across the barrier. When the barrier is exposed, a very small Chezy coefficient (high friction) is used to "stop" the flow. When overtopping occurs, the coefficient

is increased to a specified maximum as a function of the water level over the barrier. As the water level decreases at a later time, the coefficient is decreased accordingly.

22. The approximations necessary to implement these boundary conditions for the implicit code are presented in detail in Appendix B.

Numerical Stability

23. For an explicit solution scheme, the grid size and computational time step are related through a stability criterion. The criterion associated with the explicit scheme presented here is given by the relation

$$\Delta t \leq \frac{\Delta S}{\sqrt{2gd_{max}}} \tag{15}$$

where ΔS is the mesh size and d_{max} is the maximum water depth occurring in the model. This approximate condition was derived from expressions obtained by linearizing the problem. When the nonlinear terms are included, it can be expected that the time step will require further reduction.

24. Again considering the linearized equations, it can be shown that the implicit difference scheme is unconditionally stable. In other words the space and time steps may be chosen to meet required accuracy in representing topographic features and external forcing functions. The inclusion of the nonlinear advective terms (of the form $U \frac{\partial U}{\partial x}$, $V \frac{\partial U}{\partial y}$) into the implicit scheme may result in an inherent instability. All derivatives in the basic equations are approximated with centered differences over a single-grid space with the exception of the advective terms, which are computed over two grid cells. Oscillations of the water level at a grid point (period $4\Delta t$) may occur and grow unbounded.

25. A scheme which proved effective in eliminating these instabilities was the use of a recursive digital filter in the form

$$\eta^{k+1/2} = a\tilde{\eta}^{k+1/2} + b\eta^{k} + c\eta^{k-1/2} \tag{16}$$

where $\tilde{\eta}$ represents the latest computed water level and η the filtered water-level value actually used in further computations; coefficients a, b, c are chosen to damp oscillations with periods on the order of $4\Delta t$ (corresponding to 1/2 the Nyquist frequency), while permitting the longer period wave motion to remain almost undisturbed. The coefficients of the digital filter must also be chosen in such a way as to maintain the stability of the filter. By comparing the results of applying the linearized system with and without a filter it was demonstrated that filtering has a negligible effect on the solution for water levels and flows. For applications presented in this report, values of $a = 0.6$, $b = 0.3$, and $c = 0.1$ were selected after performing a parameter study varying the coefficients over wide range from (a, b, c) = (0.89, 0.1, 0.01) to (0.4, 0.4, 0.2). A more detailed discussion of digital filter techniques is given in Appendix C.

26. An additional instability, which is termed a "secondary flow" phenomenon, may also occur. A discussion of this problem was presented by Vreugdenhil.[11] The scheme normally employed to eliminate this instability is the inclusion of eddy-viscosity terms in the momentum equations of the form

$$\varepsilon\left[\frac{\partial^2 U}{\partial x^2} + \frac{\partial^2 U}{\partial y^2}\right] \tag{17}$$

where ε is taken as a constant eddy-viscosity coefficient. Such a term is actually a representation of the neglected effective-stress terms in the vertical planes. Effective stresses in vertical planes not only contain viscous and turbulent contributions but also contributions from the momentum flux due to nonuniform vertical velocity profiles. The importance of these terms should be investigated for strongly curved flows with considerable divergence or convergence. No conclusive theory has been formulated as to the mechanism of generation of secondary flow and its relation to the nonlinear instabilities involved. One method for determining whether or not the neglect is justified is that of hindcasting; that is, computations are made with and without these terms for a known situation (where prototype data are available). The value of

ε can be estimated for order of magnitude from the relation

$$\varepsilon \simeq 6\sqrt{g(U^2 + V^2)/C} \tag{17}$$

Other estimates for ε have been given by Deardorff.[12] The implementation of the eddy-viscosity terms is discussed in detail in Appendix C.

PART IV: COMPARISON STUDY--MASONBORO INLET APPLICATION

Method of Comparison

27. The method of comparison consists of applying both the RB and WI codes to a 7.5-square-mile* area at Masonboro Inlet, N. C. This application was selected for a number of reasons including:

a. Good prototype data were available.

b. A physical model study of Masonboro Inlet was performed at WES by Sager and Seabergh[13] making available additional data for calibration and verification.

c. Masonboro Inlet and surrounding area is a complex system characterized by a combination of interconnected channels together with a considerable area within the system subject to flooding above mean low water.

d. A jetty-weir system extends seaward from the northern outer barrier island allowing testing of the subgrid barrier features available in both codes.

28. The conditions (grid area, spatial step, boundary conditions, etc.) for application of both codes were identical. Comparisons of agreement of surface elevations and depth-averaged velocities with prototype measurements were made for each scheme. A comparison was also made between the computer-generated circulation patterns and pictures of surface flow patterns taken of the physical model (with the use of confetti particles). This application differs from a coarse grid-fine grid approach used by Masch in simulating the tidal hydrodynamics at Masonboro Inlet.

Description of Computational Area and Input Data

29. In choosing a computational grid for simulating the hydrodynamics at Masonboro Inlet, a number of factors were considered. Seaward open boundaries, at which the ocean tide is applied, had to be set

---

* A table of factors for converting U. S. customary units of measurement to metric (SI) units is presented on page 4.

at a distance from the inlet throat area such that transients developing at the boundary due to numerical approximations would not affect the calculations inland from the entrance channel. Interior forcing boundaries were chosen where prototype or physical model data exist. The grid size had to be chosen small enough to represent the topographic features of the study area with sufficient resolution to permit an accurate simulation of the tidal flows. A 300-ft step size resulting in a grid of dimensions 41 × 57, was chosen for this study as a compromise between a very accurate resolution and excessive computational costs. A map of the inlet system is shown in Figure 4. The resulting number of computational water points was 1721.

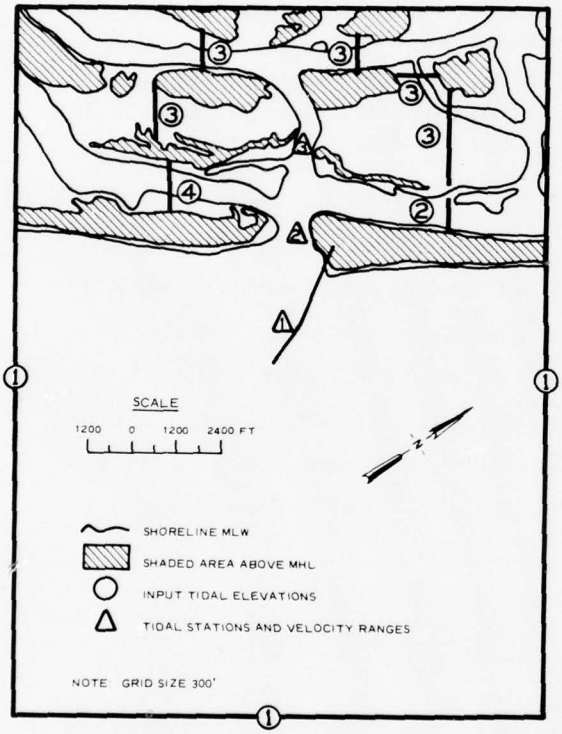

Figure 4. Areal extent of computational grid for Masonboro Inlet, N. C.

30. The jetty system protruding from the outer barrier island is composed of a weir section, with a top elevation of +2 ft mlw (Beaufort datum) and 1000 ft in length, extending from the outer island to near the bend in the jetty. The remainder of the structure is impermeable. Exposed barriers were used to represent very narrow strips of high land

in the system's marsh areas. The seaward model boundaries were set at a distance of 6,000 to 10,000 ft from the inlet throat.

31. Tidal elevations obtained from prototype (survey of 12 Sep 69) and physical model data were imposed at boundary lines denoted by circled numbers in Figure 4. Tidal elevations at boundary 3 within the marsh were taken as approximately the same as those in the innermost channels. Bathymetric surveys of the computational area were digitized. Frictional coefficients were defined by assigning number codes to the various types of terrain and applying known values of Manning's n to these number codes. The program uses the relation

$$C = \frac{1.49}{n} d^{1/6} \tag{19}$$

to calculate the Chezy frictional coefficient as a function of Manning's n and total water depth. Since the prototype data were taken on a calm day, no wind stress was applied in the numerical model. Other parameters were required as input data, including such items as gage locations, printout and plot controls, and other logic control parameters. Eddy-viscosity terms were not required in this simulation to maintain numerical stability. The selection of time-step size is discussed in the next section. The RB and WI codes use essentially the same data but the tabular form of the input data differs. It should be noted that a more compact form for the input data was programmed for the WI code.

Discussion of Results

32. As stated previously, both the WI and RB codes were applied to the identical computational grid approximating Masonboro Inlet and associated estuarine system. The results from both models show good agreement with prototype measurements at all gages. The locations of velocity ranges and tide gages for the 12 Sep 69 prototype survey are given in Figure 5. The time-step sizes used for the calculations were 3 sec for the RB model and 90 sec for the WI model. The stability criterion as given by Equation 15 predicts a 5.5-sec time step for stable

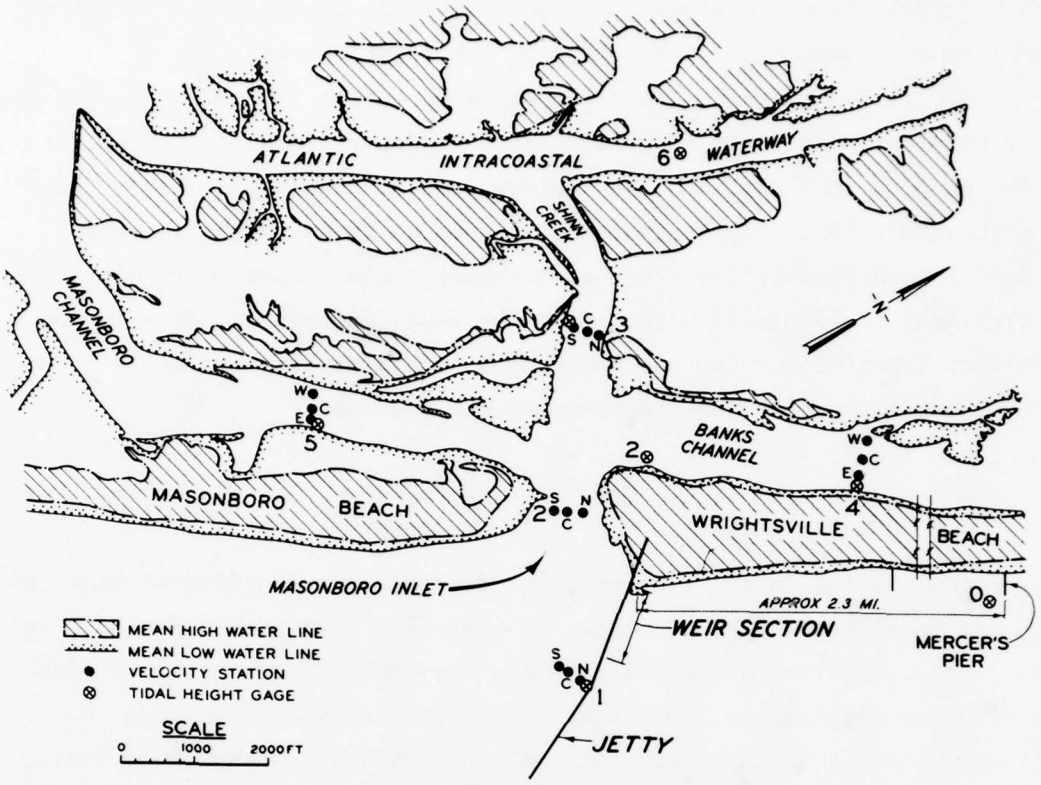

Figure 5. Velocity range and tide gage locations at Masonboro Inlet

computations involving a linearized set of equations. Tests were made with Δt = 5 and 4 sec and instabilities in the deeper ocean area of the grid were noted. Calculations with Δt = 3 sec were stable. The WI model was tested for Δt = 45, 90, and 180 sec; the results for the two smaller time steps were essentially the same and the results for Δt = 180 sec showed some disparity. Plots of the current velocity at a typical gage location for Δt = 45, 90, and 180 sec are given in Figure 6. On the basis of such comparisons a time step of Δt = 90 sec was selected.

33. The computations were begun at 1350 EST and a fold-over occurred at 2000 EST, equating input boundary conditions at this point in time with those at 0730 EST. This procedure may cause some discrepancy in the results but is required since the models must "spin up" from a quiescent state at low tide. It is preferable to begin the computations

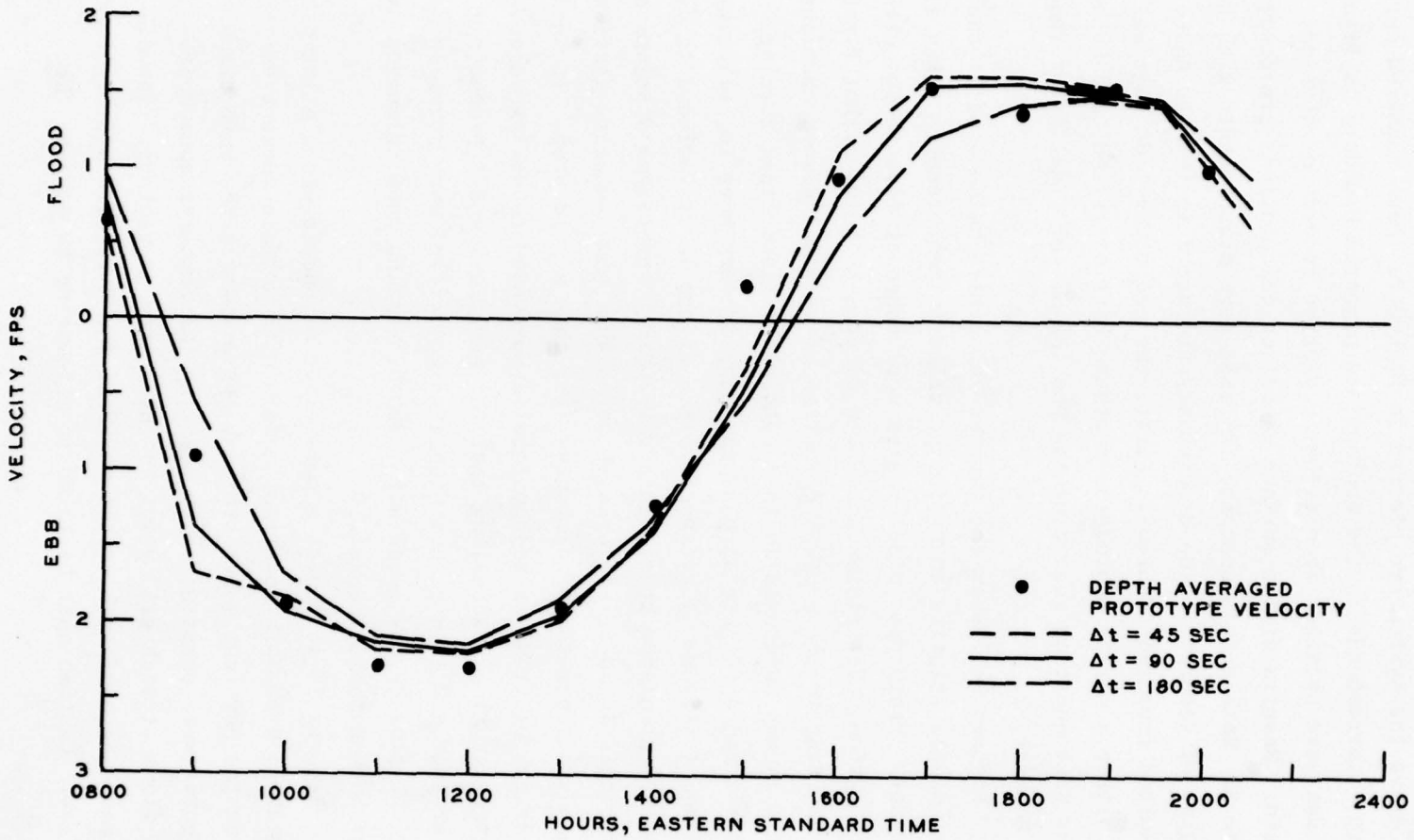

Figure 6. Comparison of typical current velocities for three calculation time steps

at the beginning of the flood phase of the tidal cycle. The four tides used to drive the system are plotted in Figure 7. Each numbered curve in Figure 7 corresponds to the appropriate numbered boundary in Figure 4. These tides were obtained from either prototype records or physical model data. Results of the surface elevation calculations are displayed in Figure 8. Both models describe the tide gage measurements with the same degree of accuracy. The discrepancy at gage 2 in the ebb phase may have resulted from two problems. First, the prototype tide gage was located within a marina behind the northern barrier island; and second, there was some question regarding the phasing of the tidal input specified at boundary 2.

34. Figures 9-11 show the current velocities calculated in the numerical models relative to prototype velocity measurements taken at three depths. Prototype velocity data were taken at five ranges within the inlet system. Velocities have been plotted as being either flood or ebb according to the general direction of movement across each range. Only three ranges were used in this comparison since tidal forcing boundaries 2 and 4 (Figure 4) pass through, or very near to, velocity ranges 5 and 4 (Figure 5), respectively. Figure 12 is included to depict results calculated at stations very near to prototype stations on velocity ranges 4 and 5. It also is noted that some velocity stations on a range are separated by distances less than a grid step. In such cases averages of flows at adjacent cells were used to define velocities at the gage location. Recalling that the numerical model produces a depth-averaged unit flow rate, integrated velocities were obtained by dividing the flow by the local water depth. Again, good agreement was noted for both numerical models.

35. Figures 13-16 depict a comparison of sample circulation patterns obtained from both numerical models with surface current patterns taken from the physical model study at approximately the same times. These figures were constructed by plotting the instantaneous depth-averaged flows at each grid point in the system as vectors. The direction and length of each vector indicate the direction and magnitude of the flow. Caution must be taken in attempting to compare the

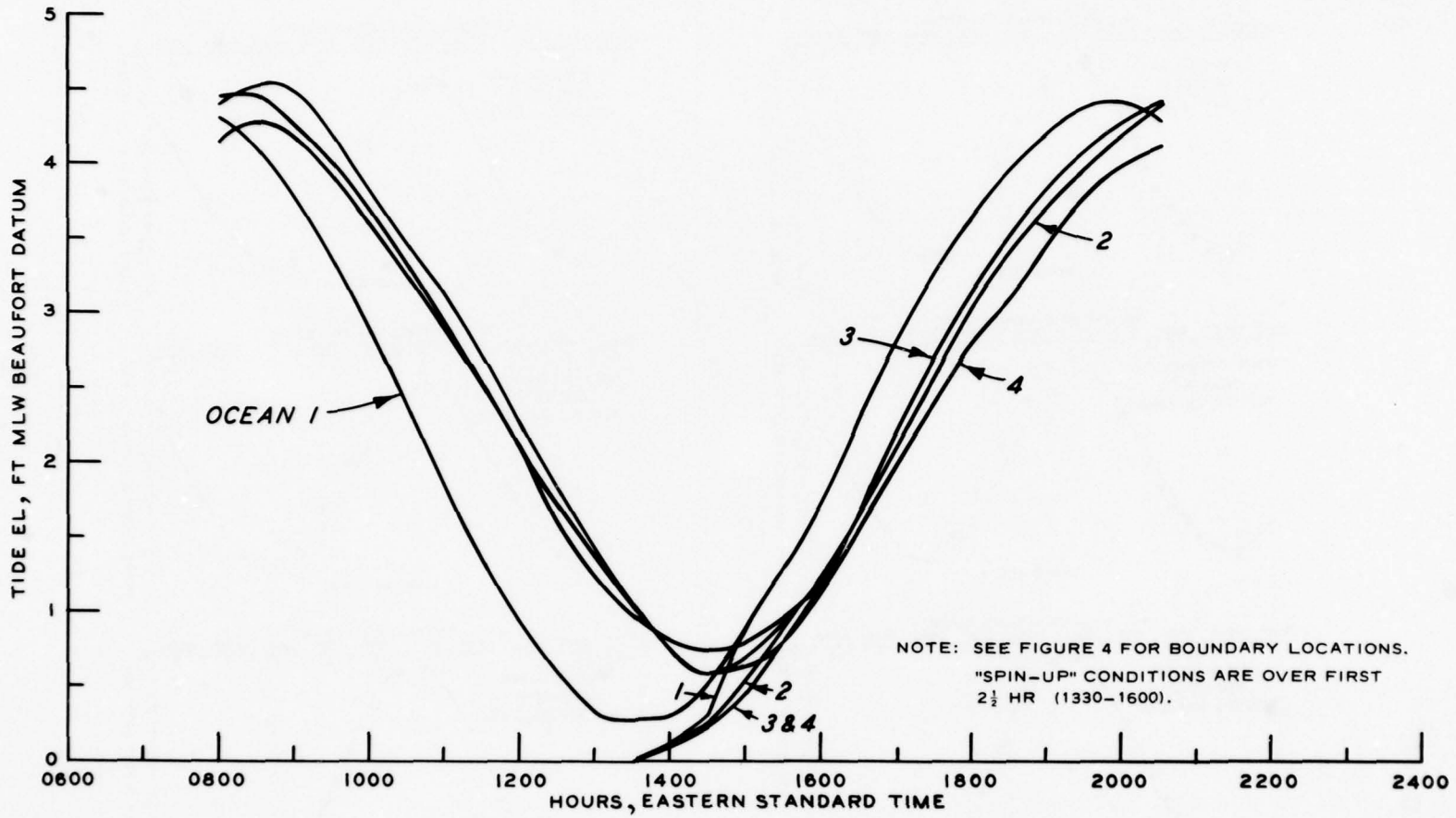

Figure 7. Forcing tides for Masonboro model

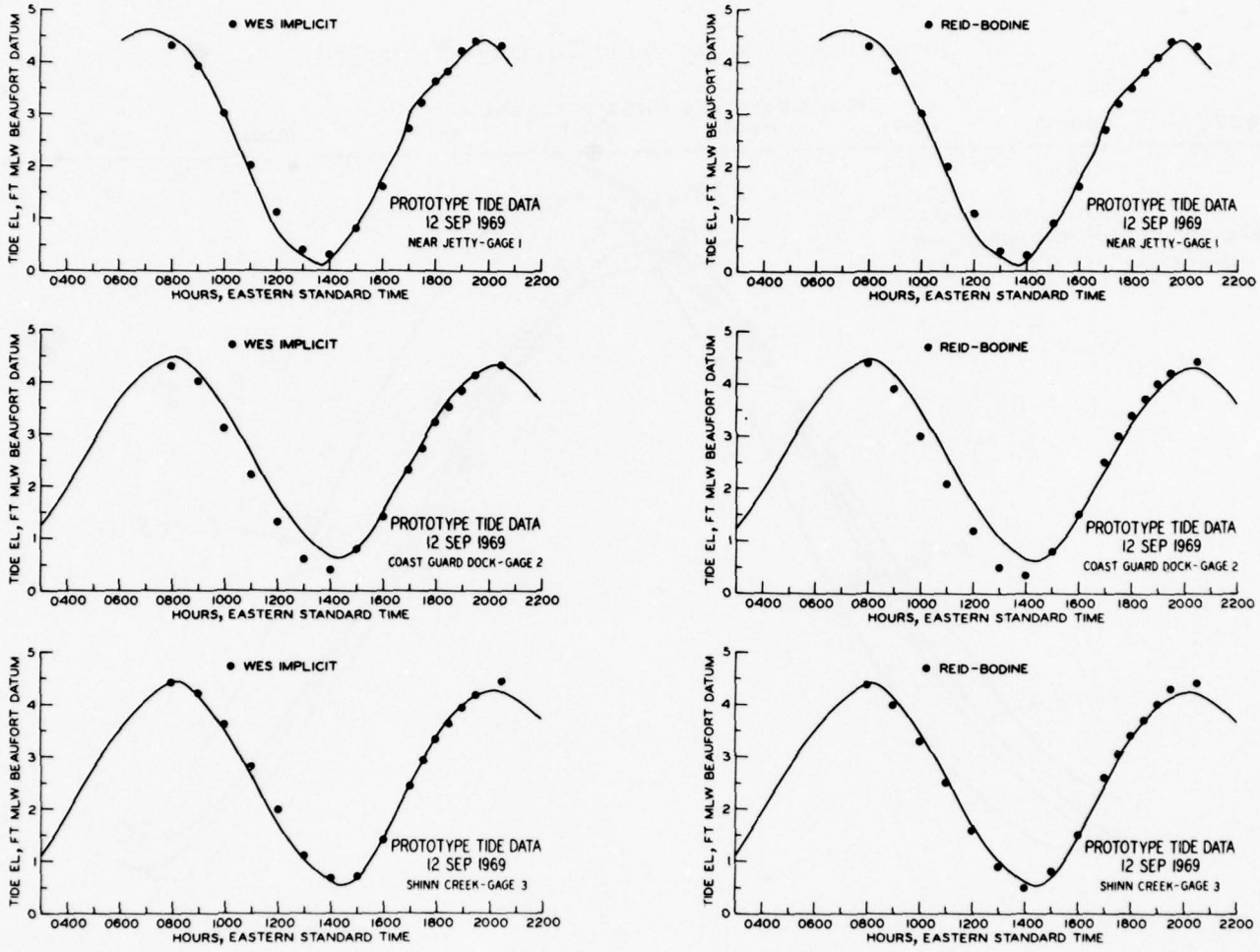

Figure 8. Comparison of surface elevation agreement with prototype for the WI and RB codes

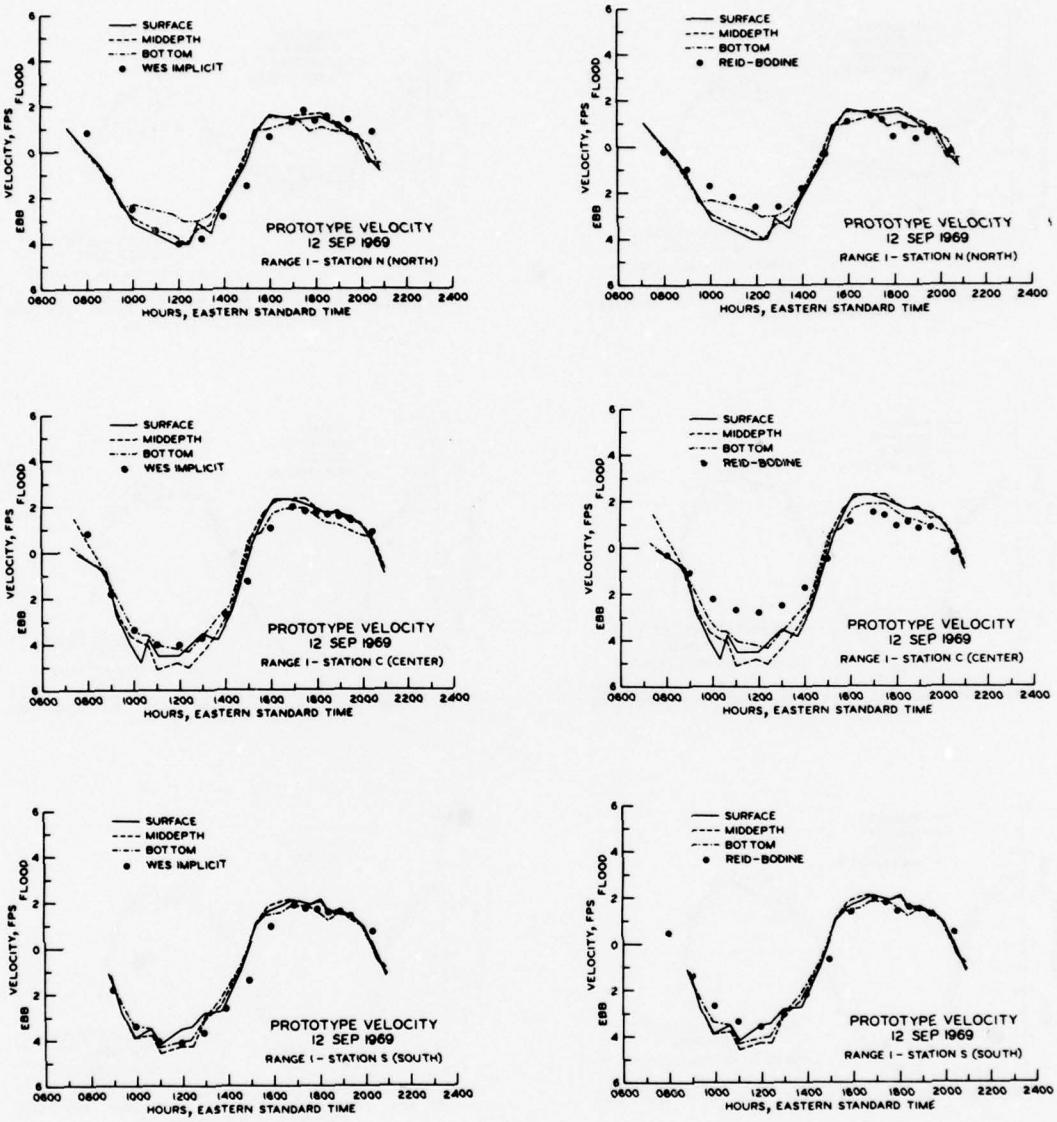

Figure 9. Comparison of current velocity agreement with prototype at range 1 for the WI and RB codes

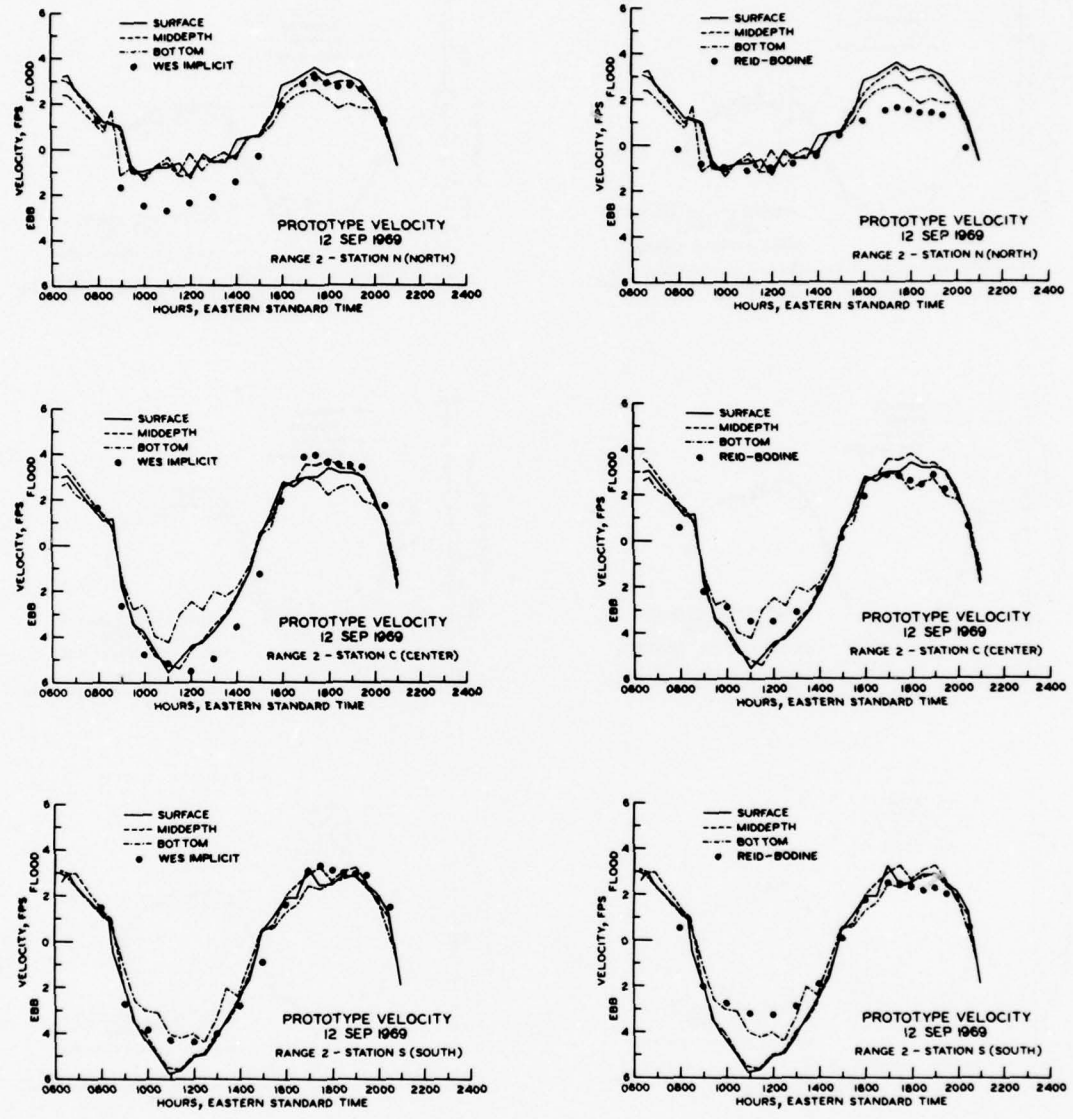

Figure 10. Comparison of current velocity agreement with prototype at range 2 for the WI and RB codes

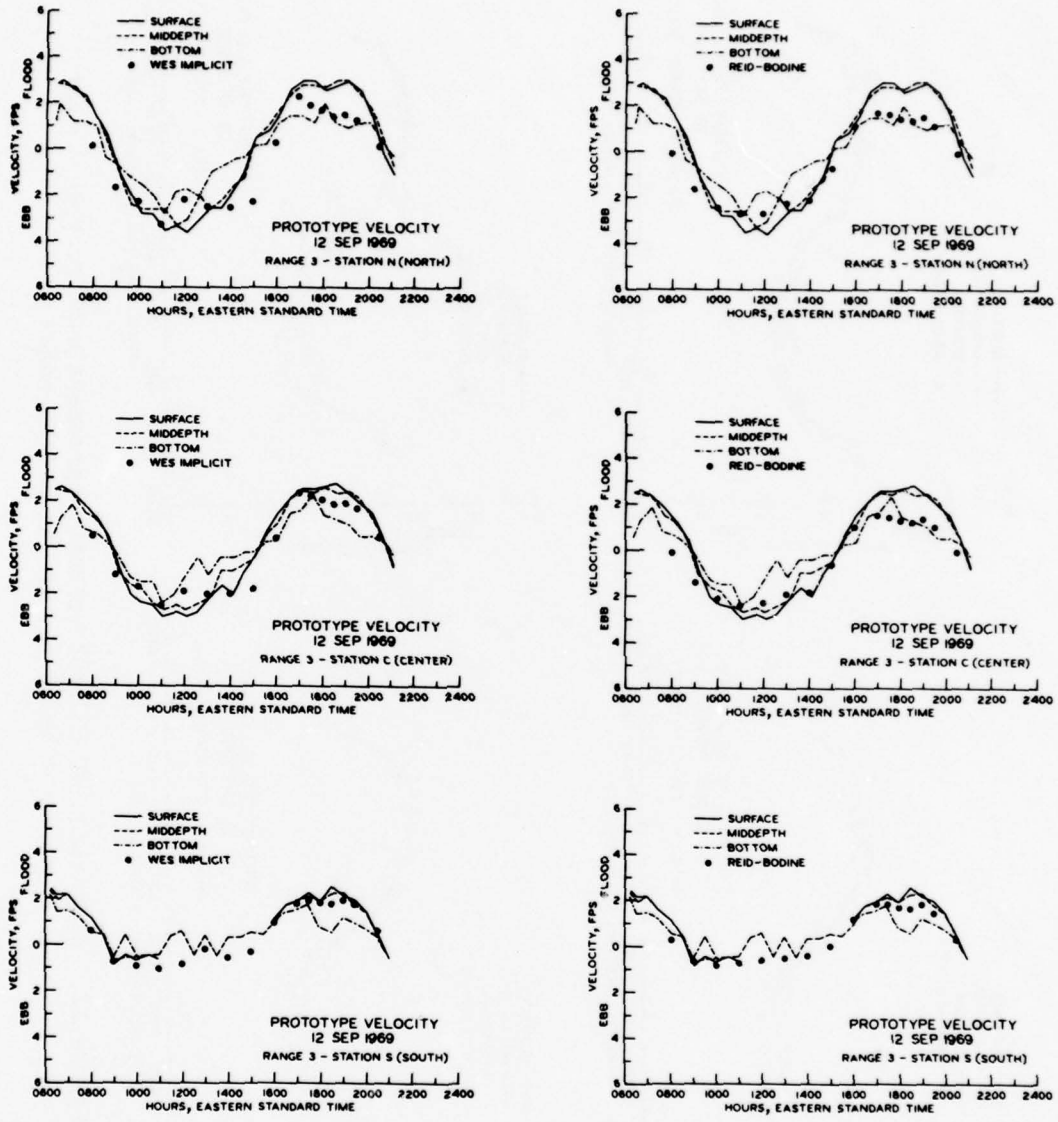

Figure 11. Comparison of current velocity agreement with prototype at range 3 for the WI and RB codes

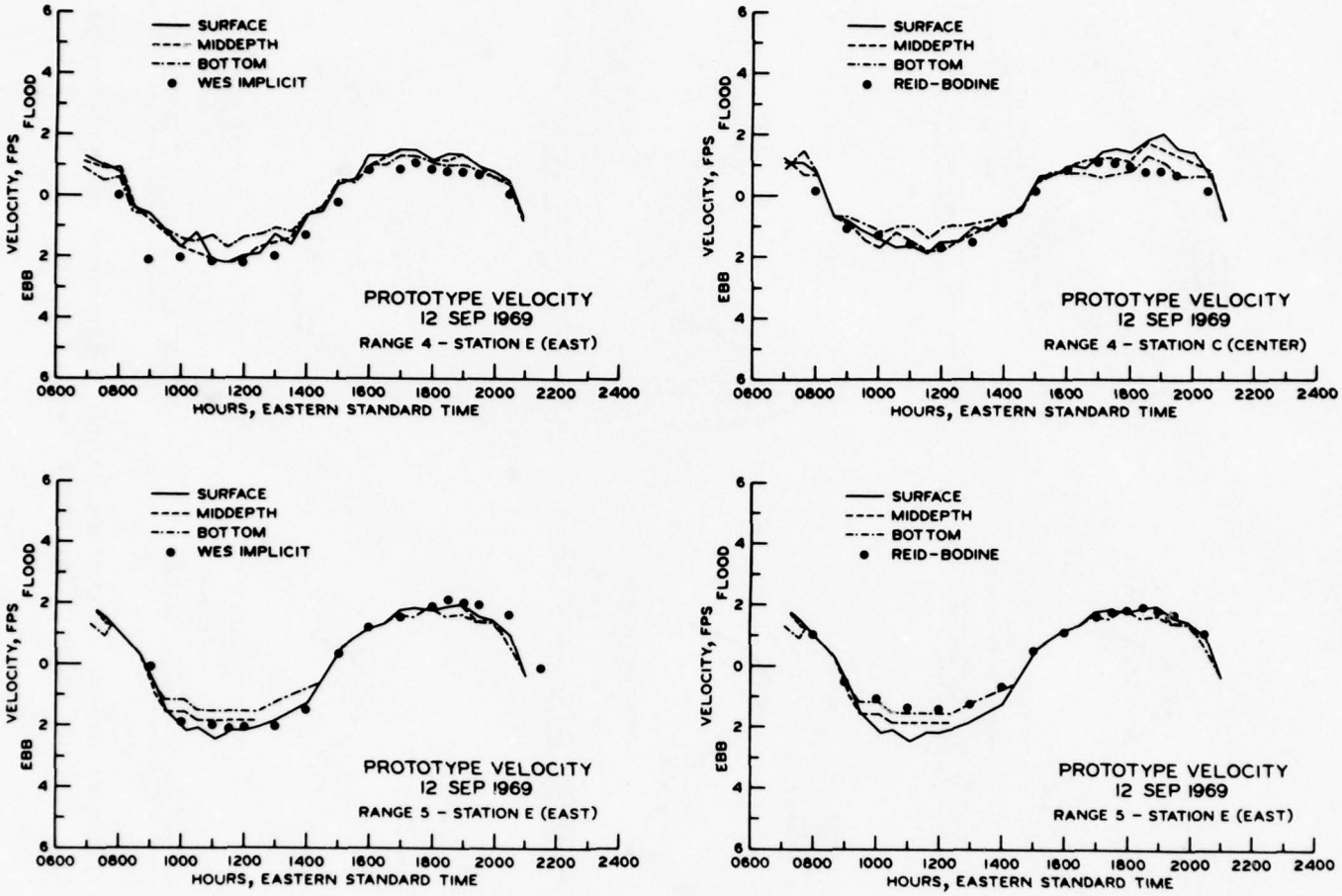

Figure 12. Comparison of current velocity agreement with prototype near ranges 4 and 5 for the WI and RB codes

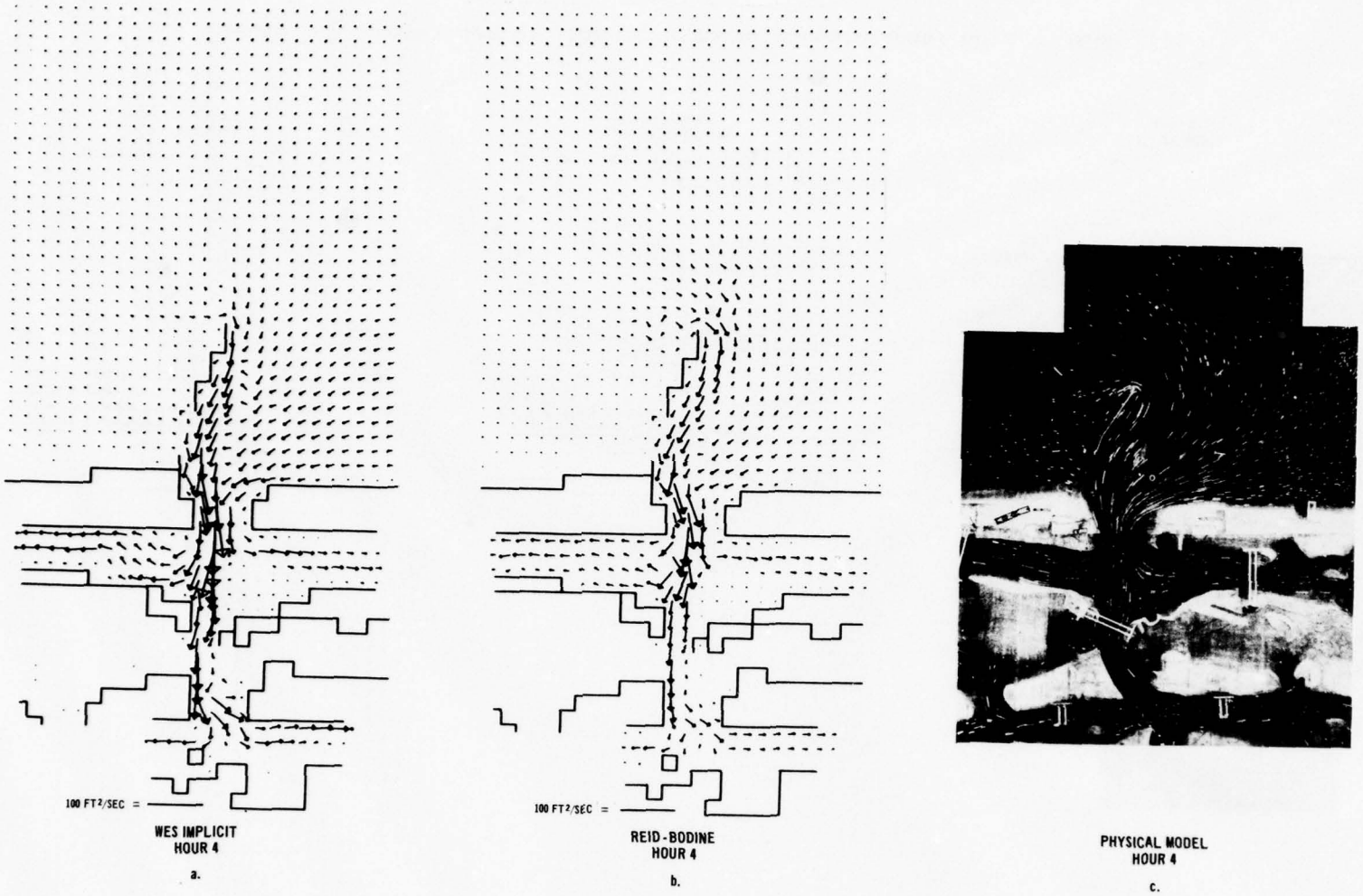

Figure 13. Comparison of flow patterns at computational hour 4 (1750 EST)

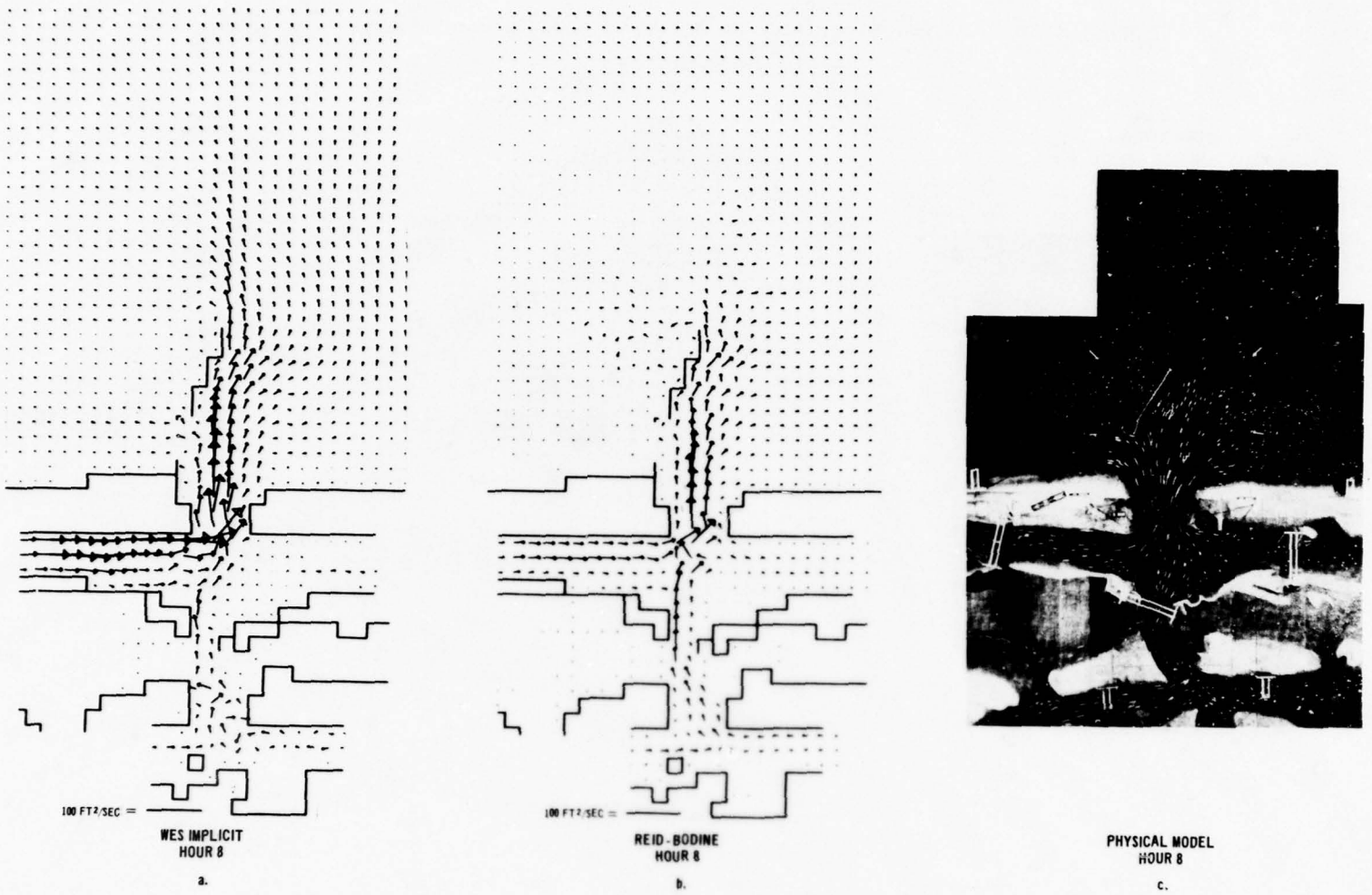

Figure 14. Comparison of flow patterns at computational hour 8 (0900 EST)

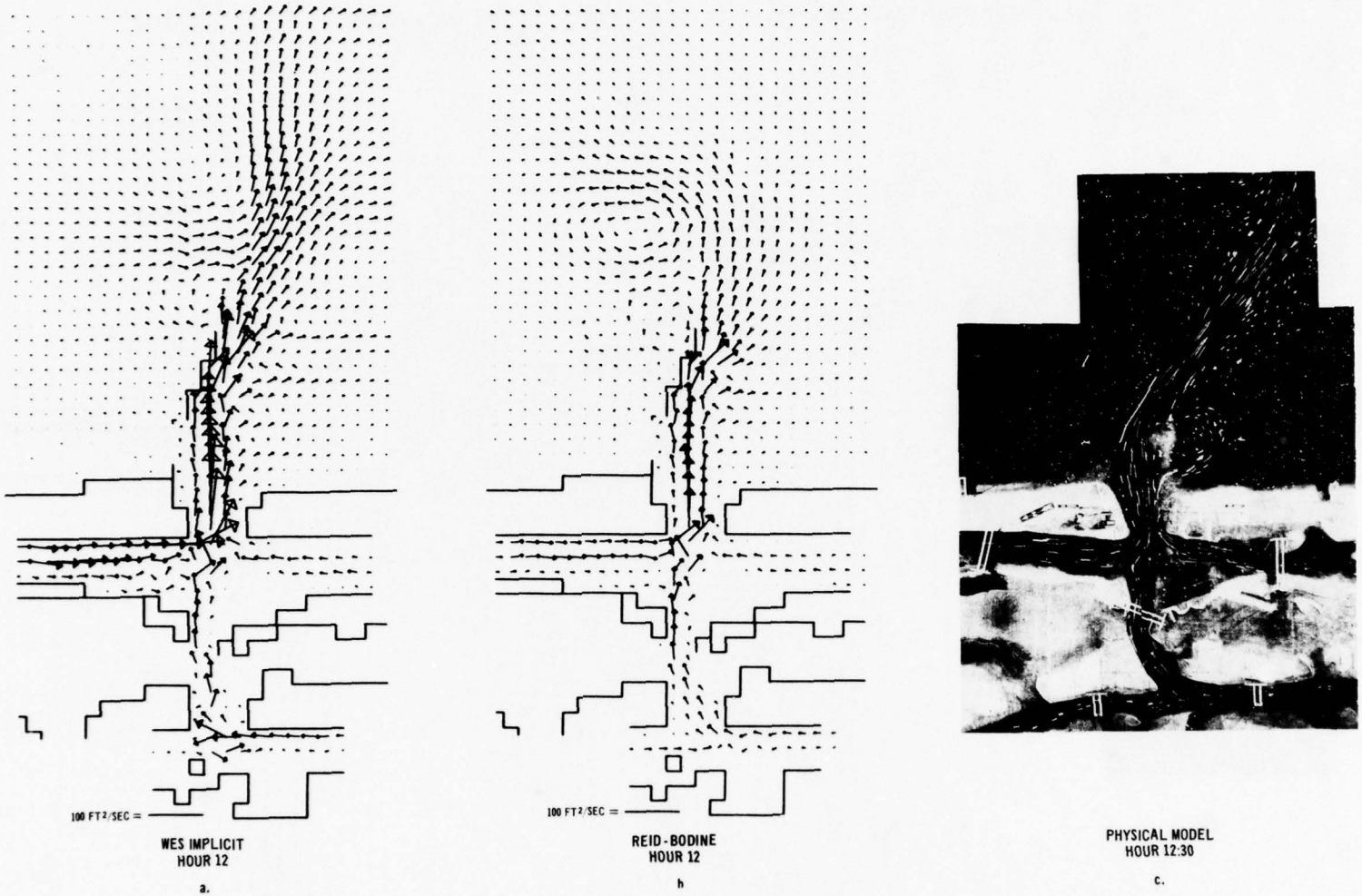

Figure 15. Comparison of flow patterns at computational hour 12 (1300 EST)

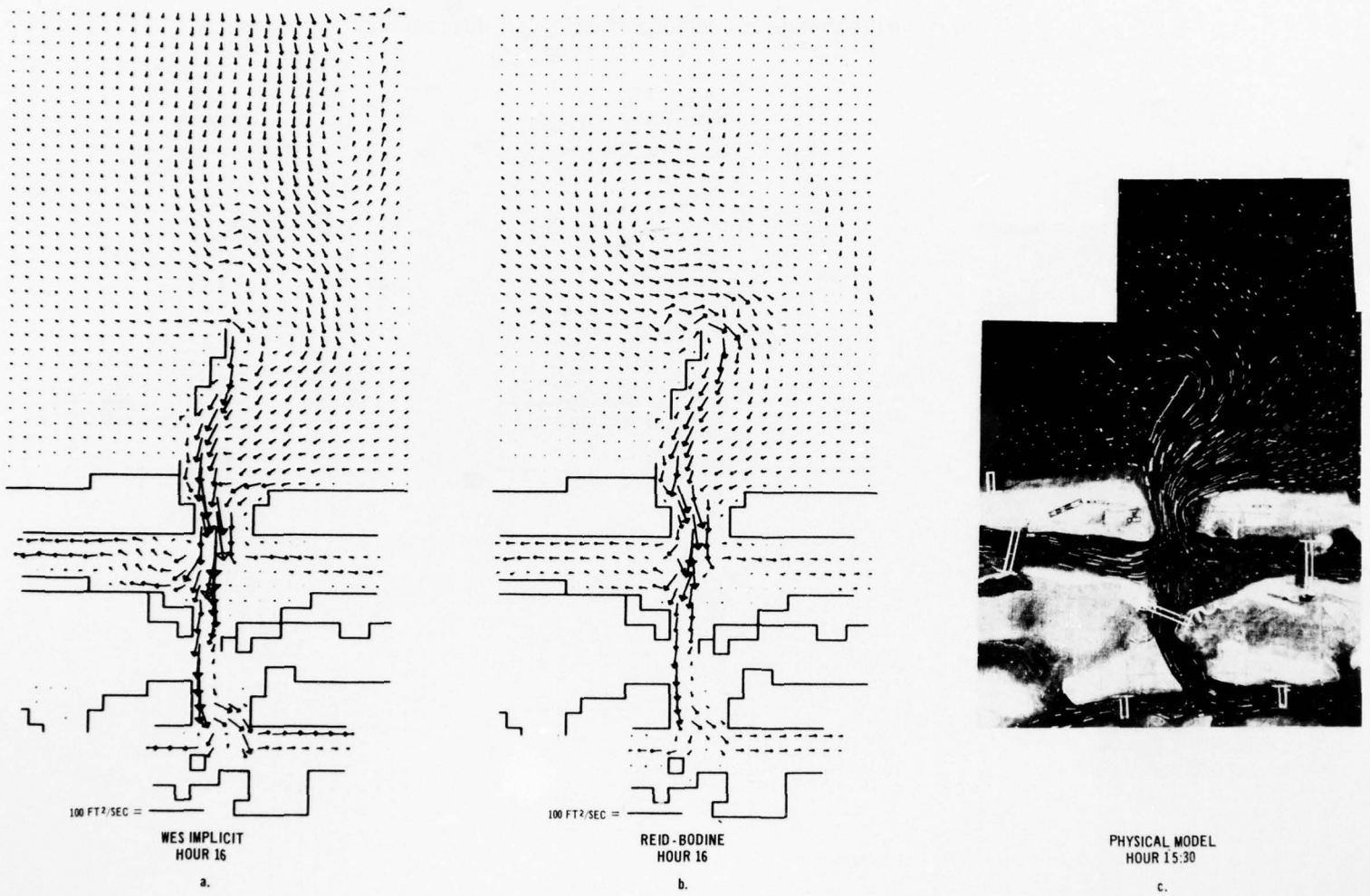

Figure 16. Comparison of flow patterns at computational hour 16 (1700 EST)

numerically generated flow patterns with photographs of the surface velocity patterns obtained in the physical model. The numerical results portray instantaneous values of a vertically averaged flow, whereas the photographs are time exposures of surface currents over a period of about three minutes in the prototype. For Figures 15 and 16 the physical model photograph times differ from the numerical plot times by half an hour. In this light it is observed that the major features of the circulation patterns photographed in the physical model are reproduced in the numerical models. The WI model appears to do a better job in describing the flow, in particular the flow around the jetty and over the weir in Figure 13, channel flows in Figure 14, and the direction of the ebb jet in Figure 15.

36. Table 1 presents the characteristics and run statistics for the Masonboro Inlet simulation. Recall that Δt for the implicit scheme is the time for a complete computational cycle, that is, U and V are computed once and η twice. In the explicit scheme, U, V, and η are computed once in a time step of 3 sec. The relative speed of the implicit scheme can be expressed by the relation

$$S_I \approx 0.5 \frac{\Delta t_i}{\Delta t_e} \tag{20}$$

where Δt_i and Δt_e are the time steps of the implicit and explicit schemes, respectively, and S_I is the execution speed of the implicit model relative to the explicit model. As seen in Table 1, a 15:1 ratio in execution time was obtained for the time steps chosen.

37. In the application of numerical models, various techniques have been used in previous studies to "tune" the model to produce a better agreement with prototype data. The applications presented in this report have been made in a straightforward manner. Schemes such as placing fictitious submerged barriers within channels to control the flow were not used, nor were such barriers used at velocity gage locations to obtain the correct flow rate. Higher values for Manning's n were used to represent flow restrictions in areas where the actual land formations could not be approximated accurately with the selected

grid step. Experience with this study indicated that by correctly applying excitation tidal histories, bathymetry, and standard values for frictional coefficients, both of the numerical models (RB and WI) could simulate prototype conditions with little or no tuning. If tuning is required, it can be accomplished by minor adjustments of frictional coefficients. Results of the comparison study clearly demonstrate the reliability and cost effectiveness of the implicit scheme for modeling tidal hydrodynamics of a complicated inlet-wetlands system.

PART V: CORSON-GREAT EGG COMPLEX

Field Surveys

38. A prototype field survey at GECI was performed during 1974-1975 by the staff at Rutgers University, New Brunswick, N. J.[7] A complete description of the geometric characteristics of GECI, prototype tide data, current data, and hydrographic survey data is given in the Rutgers report. The datum for all data was taken to be 1929 SLD. Tidal elevations and current measurements were taken at each inlet over a period of five days, interspersed between October 1974 and June 1975. Ocean tide data were made available by National Ocean Survey (NOS), an agency within the National Oceanic and Atmospheric Administration. Tides in the study area are semidiurnal with a mean range slightly greater than 4 ft. After studying the available data, it was determined that readings taken on 10 June 1975 at Corson Inlet and on 9 June 1975 at Great Egg Harbor Inlet were of higher quality than those taken on other days and should be used for model verification. In addition, the improvement plans were modeled using the same forcing tidal functions as those used for verification, providing a base for comparison relative to existing conditions. A nonnegligible wind field existed during the June surveys and is given in Table 2 for both Corson and Great Egg Inlets. As applied in the model, the wind field was taken as time-dependent but not spatially dependent.

Computational Grid

39. The same factors considered in the selection of the Masonboro Inlet grid apply to the GECI application. Due to the size of the GECI system, prototype data were not collected concurrently for both inlets and thus it was necessary to model the inlets separately. As a compromise between resolution accuracy and computational effort, a 300-ft mesh size was selected. This resolution allowed a good representation of most of the channels within each system and was also adequate for

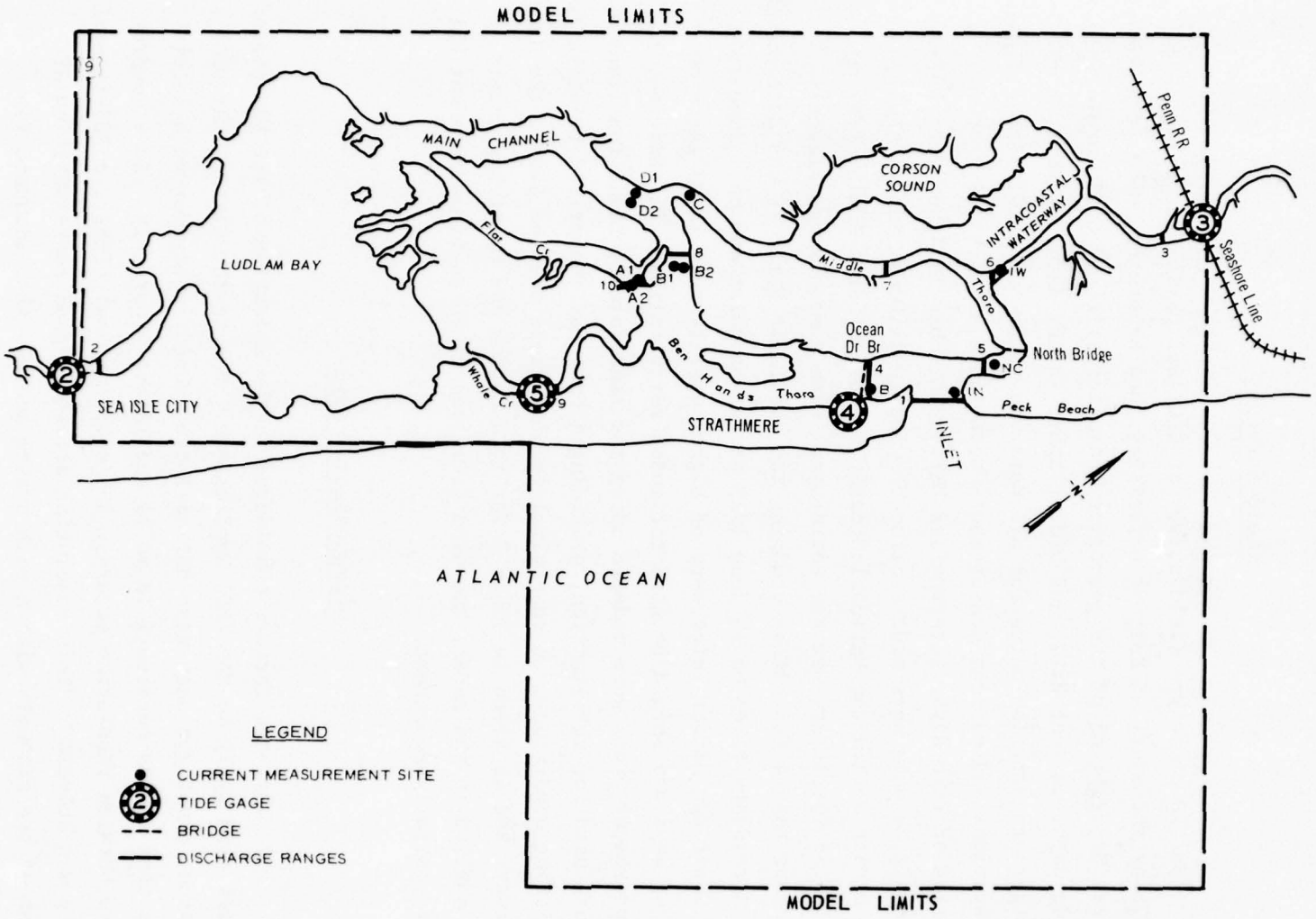

Figure 17. Extent of model area and gage locations for Corson Inlet

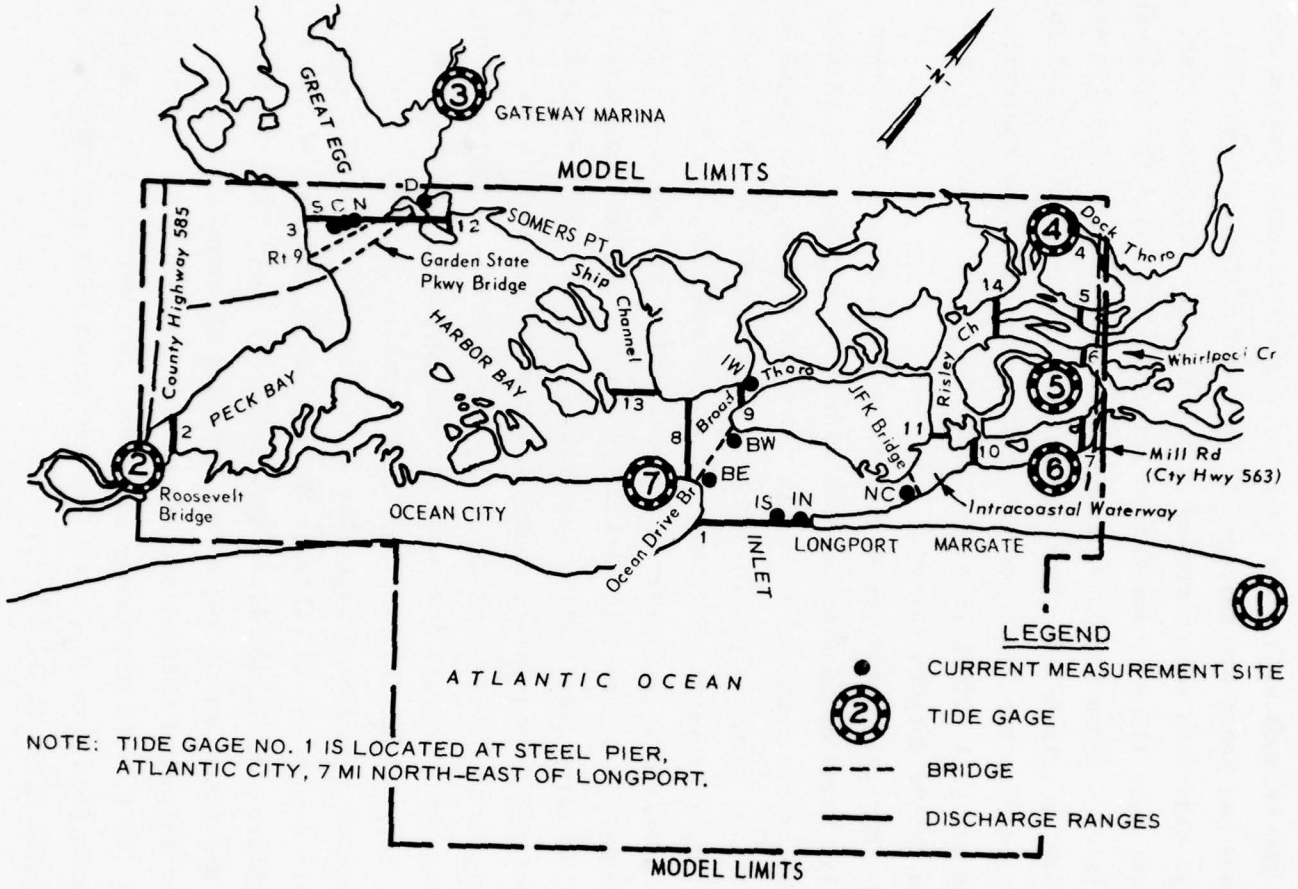

Figure 18. Extent of model area and gage locations for Great Egg Harbor Inlet

describing the proposed modifications. Figures 17 and 18 show the boundaries of the model limits at Corson and Great Egg Harbor Inlets, respectively, as well as grid alignment and pertinent gage locations. Most of the islands within the back bay regions of both systems are marshlands and hence are susceptible to flooding during high tide. The NOS ocean tide data were recorded at the Atlantic City Steel Pier. Grid dimensions were 110 × 91 for Corson Inlet and 152 × 106 for Great Egg Harbor Inlet. Those portions of the computational grid that lie seaward of the barier islands and about two miles north and south of the inlets do not extend to the limits of the grid dimensions, thus conserving the computational effort (Figures 17 and 18). The bathymetry was provided by the Rutgers survey.

40. Natural boundaries were used as computational boundaries. Typically, these boundaries consist of nonflooding barriers through which one or two channels flow. In the field survey, tide gages were placed in the channels passing through these boundaries in order to obtain proper boundary conditions. For Corson Inlet, the Seashore Line Railway provided a convenient northern boundary and the county road from U. S. Highway 9 to Sea Isle City was used as a southern boundary. The western boundary (nonflooding) was taken near the Garden State Parkway. For Great Egg Harbor Inlet, County Highway 585 was taken as a southern boundary, Garden State Parkway to the Somers Point tollgate and high land from there to Mill Road as a western boundary, and Mill Road to Margate City (County Highway 563) as a northern boundary. Tide gages were located at Ludlam Bridge (Cor 2), Seashore Line Bridge (Cor 3), Roosevelt Bridge (GE 2), Gateway Marina (GE 3), Mainland Marina in Dock Thoroughfare (GE 4), and Alton Marina (GE 6). Data from the Mainland Marina and Alton Marina gages were averaged to produce boundary conditions at Whirlpool Channel and the channel between Williams and Kiahs Islands (GE 5). As previously mentioned, the ocean boundary conditions were taken from data collected from the ocean tide gage at Steel Pier in Atlantic City, N. J. (GE 1).

PART VI: MODEL VERIFICATION

Corson Inlet

41. The objective of the verification phase of any model study is to demonstrate the model's ability to produce results that agree with known data for existing conditions. Such a test gives confidence for applying the model as a predictive tool. The model for Corson Inlet was verified by simulating existing conditions for 10 June 1975. Comparisons between prototype and model were made for tidal elevations at two gages and current velocities at 11 gages.

42. Numerous problems were encountered in the verification process. The source of most problems could be traced to the prototype data. A major discrepancy was noted in phasing of the tides at interior boundaries. The ocean gage tidal data supplied by NOS agreed closely with predicted amplitudes and phasing given in the National Ocean Survey Tide Tables, East Coast of North America.[14] To obtain reasonable results it was necessary to shift the survey tide data at the Sea Isle City and Seashore Line Bridge gages in time such that they agreed with the relative phasing given in the NOS tide tables. From the depth data given with the current meter readings in the Rutgers field survey report, it was apparent that the survey crew had great difficulty in maintaining the same gage location throughout the survey for most gages. Comparison of model to prototype should be made with full realization of the problems enumerated above.

43. Figure 19 is a plot of the three tidal hydrographs used as boundary conditions for the 10 June 1975 verification. An initial portion of the Seashore Line Bridge data was missing and had to be constructed by extrapolating the collected data from 0800 EST back to 0400 EST. Figures 20 and 21 show the comparison of tidal elevations between model and prototype for the Strathmere Coast Guard gage and the Whale Creek Marina gage. Figure 17 depicts the study region and locations for tidal gages and velocity stations. The discrepancy in the Strathmere gage results was apparently due to an error in relating

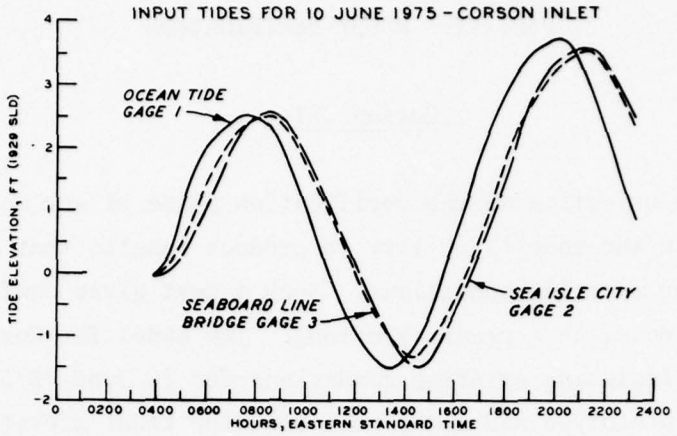

Figure 19. Forcing tides for Corson Inlet model

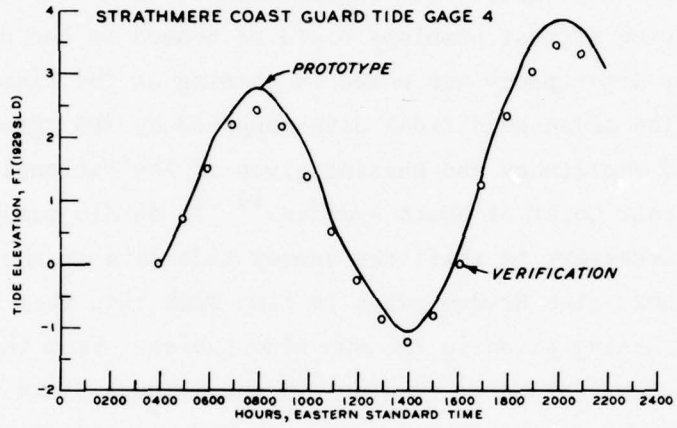

Figure 20. Comparison of surface elevation agreement with prototype for the Strathmere tide gage

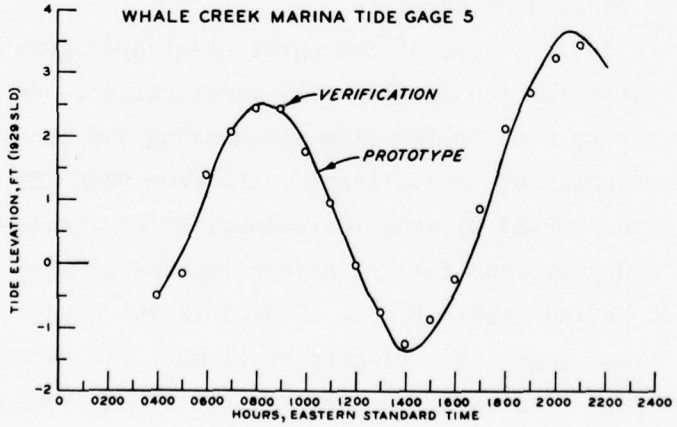

Figure 21. Comparison of surface elevation agreement with prototype for the Whale Creek Marina tide gage

the prototype tide data to the proper benchmark. This gage should have an amplitude response similar to the ocean gage but somewhat lower as indicated in the tide tables. The numerical results show such a behavior for the Strathmere gage.

44. Reproducing current velocities is a much more difficult problem than reproducing surface elevations. This difficulty arises from several sources: (a) the numerical model calculates a depth-averaged flow, an entity which cannot be measured directly in the prototype; (b) prototype velocities cannot be measured as accurately as surface elevations due to instrument limitations; and (c) the numerical model calculates velocities from flow data computed at discrete points in the grid system which may not coincide exactly with the locations of prototype velocity gages. Figures 22 and 23 depict the comparison between prototype and calculated velocities. For ease of inspection, the velocities have been plotted as being either flood or ebb according to the direction of movement across the velocity range. Due to the sparseness of the prototype data and the variation in peak current between surface and bottom readings, no attempt was made to construct smooth curves through the data. The calculated depth-averaged velocities are represented by the solid dots at one-hour intervals. The comparisons show satisfactory agreement in both phase and magnitude. Discrepancies, such as those noted for the inlet throat gage in Figure 23, may be explained in part by the shifting of the gage location in the field survey. Gage C in Ben Hands Thoroughfare was the only gage for which poor agreement between prototype and model was obtained. The poor agreement was apparently due to a lack of sufficient data on the bathymetry in the back bay area, in particular, the data relative to defining the proper flow communication between Corson Sound and the Intracoastal Waterway.

45. The study region was too large for plotting circulation patterns on a single cathode ray tube (CRT) film frame. As a compromise, an area consisting of 3250 grid points around the inlet throat was plotted. Figures 24-27 show the vector flow patterns for four times in the tidal cycle. There were no prototype data available for direct comparison with these plots. Two types of circulation patterns are

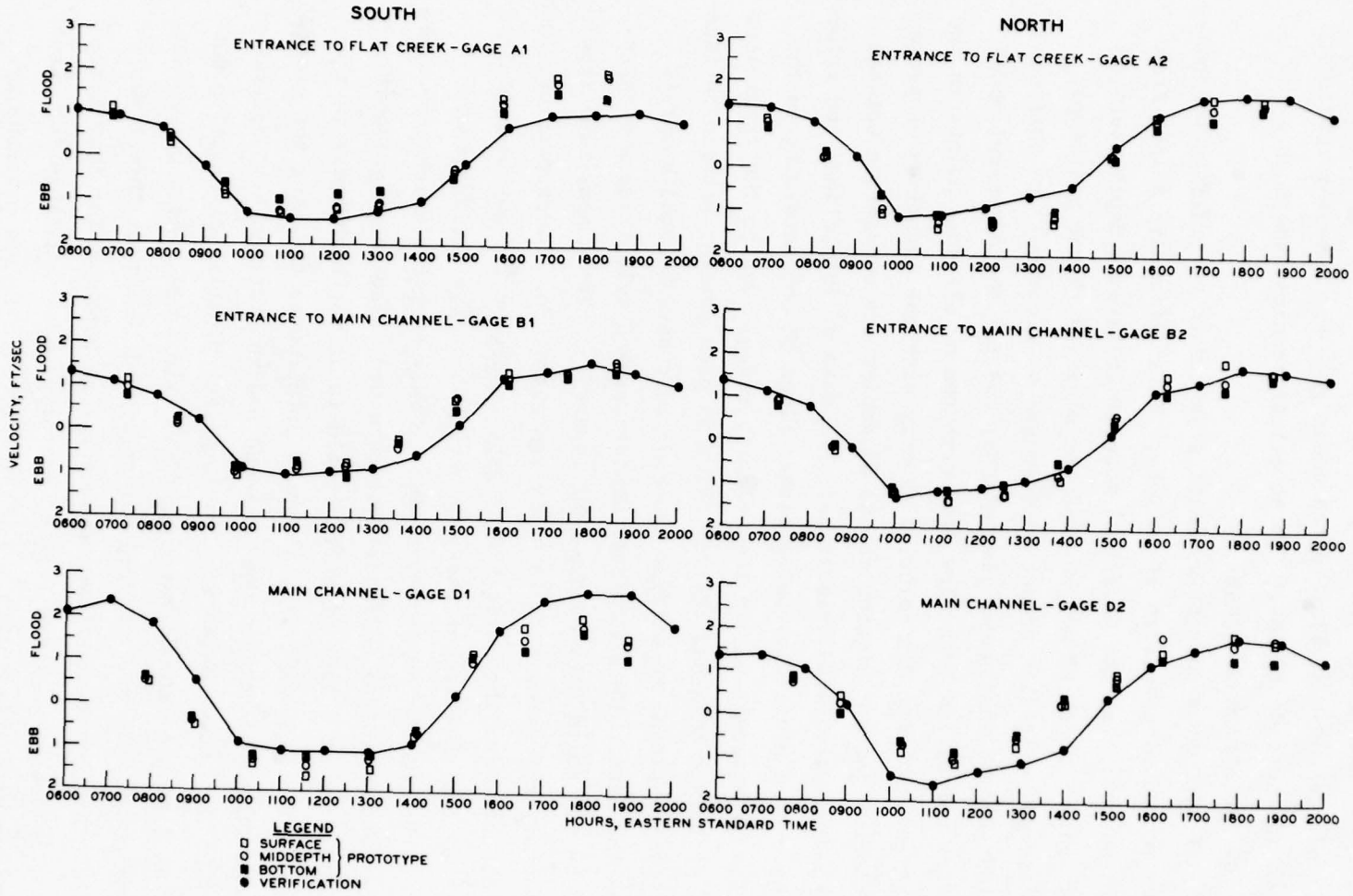

Figure 22. Comparison of current velocity agreement with prototype for Corson Inlet base gages A1, A2, B1, B2, D1, and D2

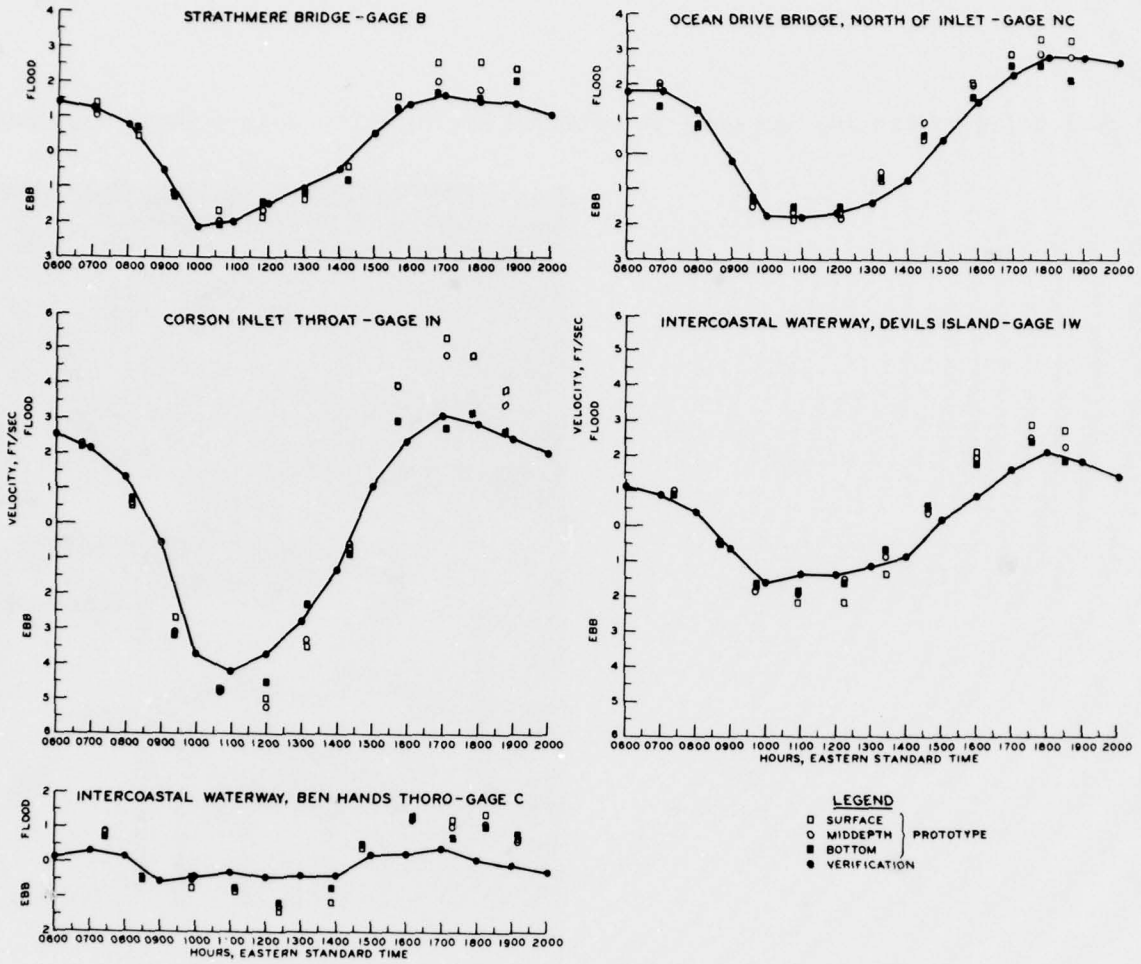

Figure 23. Comparison of current velocity agreement with prototype for Corson Inlet base gages B, NC, 1N, 1W, and C

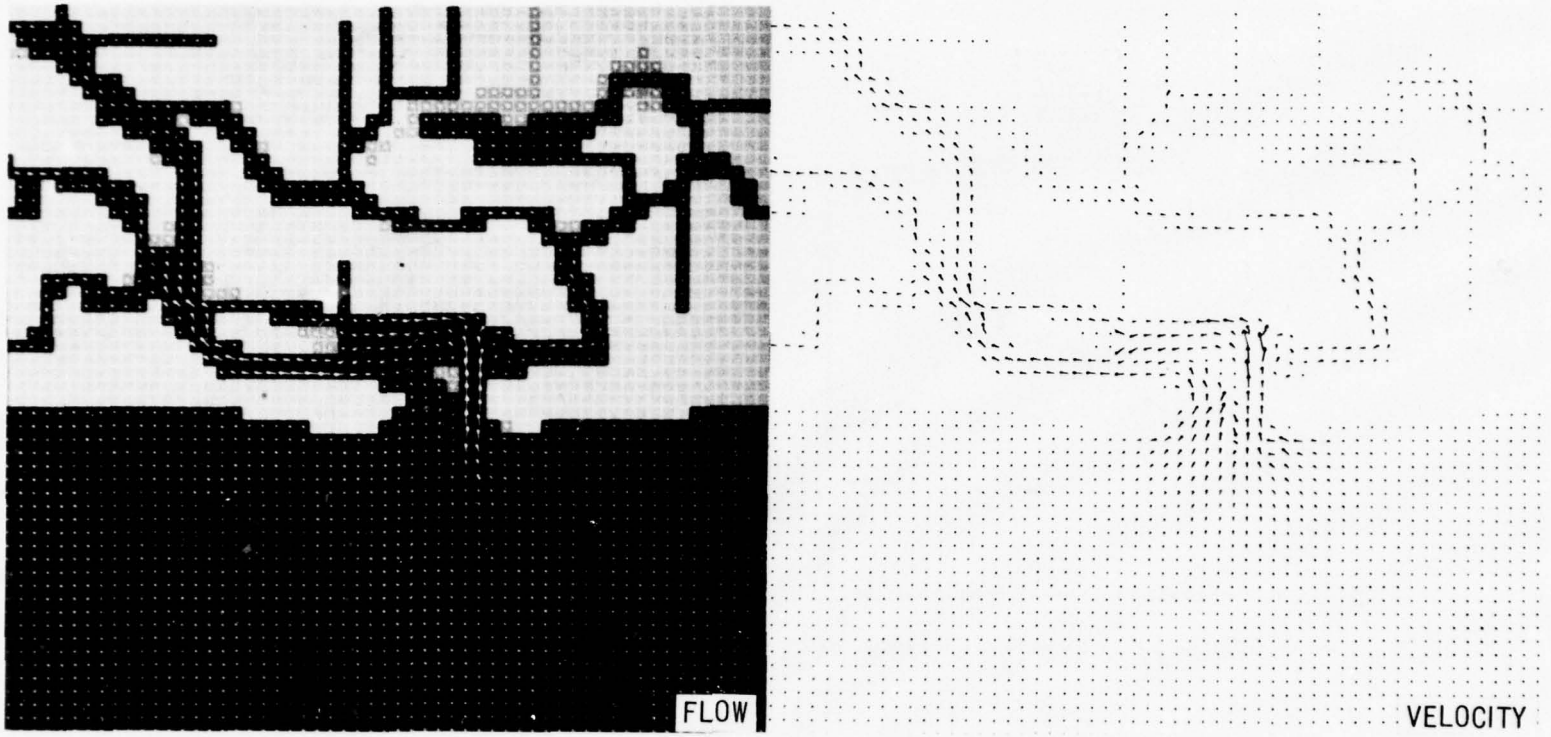

Figure 24. Comparison of unit flow and velocity patterns at 0600 EST for verification runs of Corson Inlet

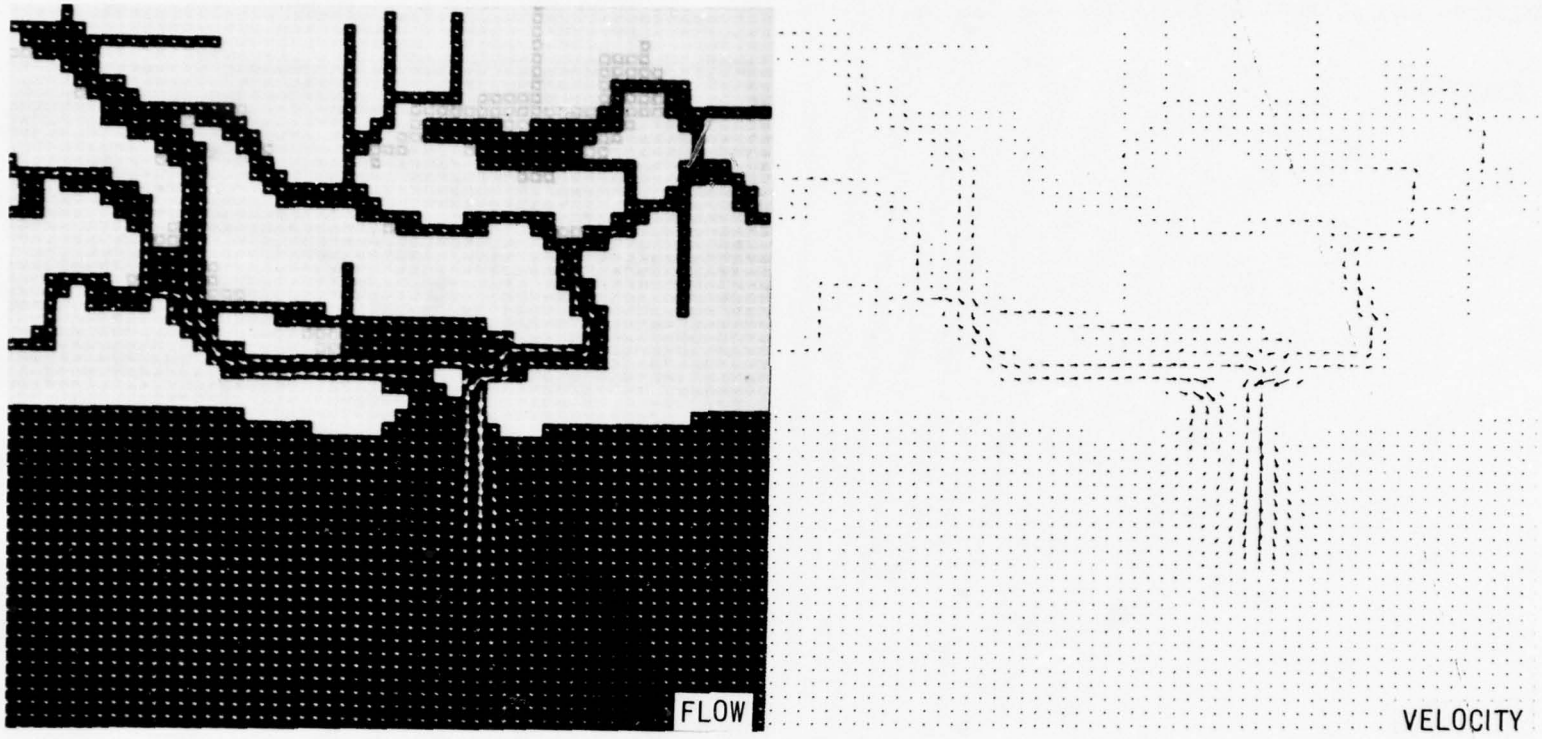

Figure 25. Comparison of unit flow and velocity patterns at 1000 EST for verification runs of Corson Inlet

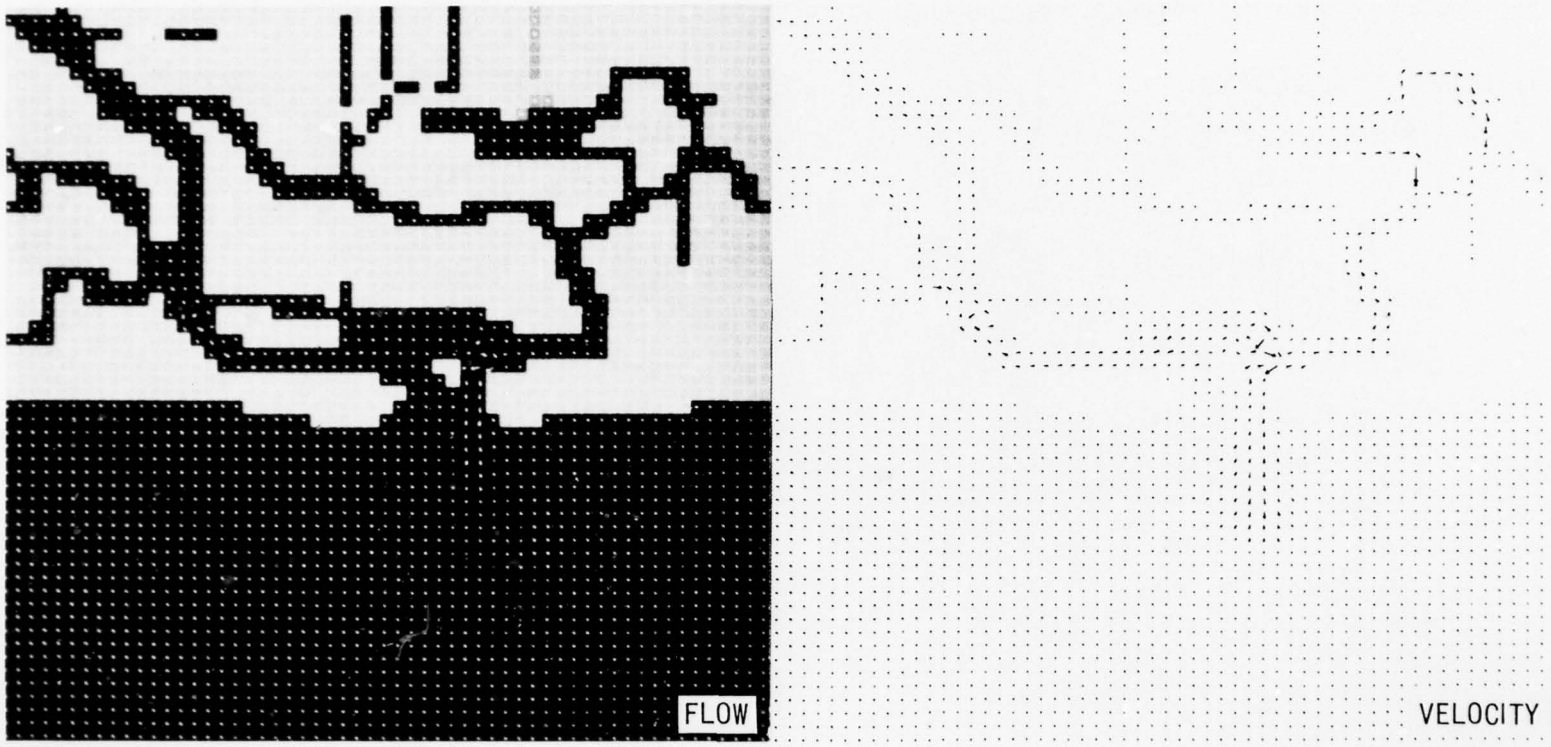

Figure 26. Comparison of unit flow and velocity patterns at 1400 EST for verification runs of Corson Inlet

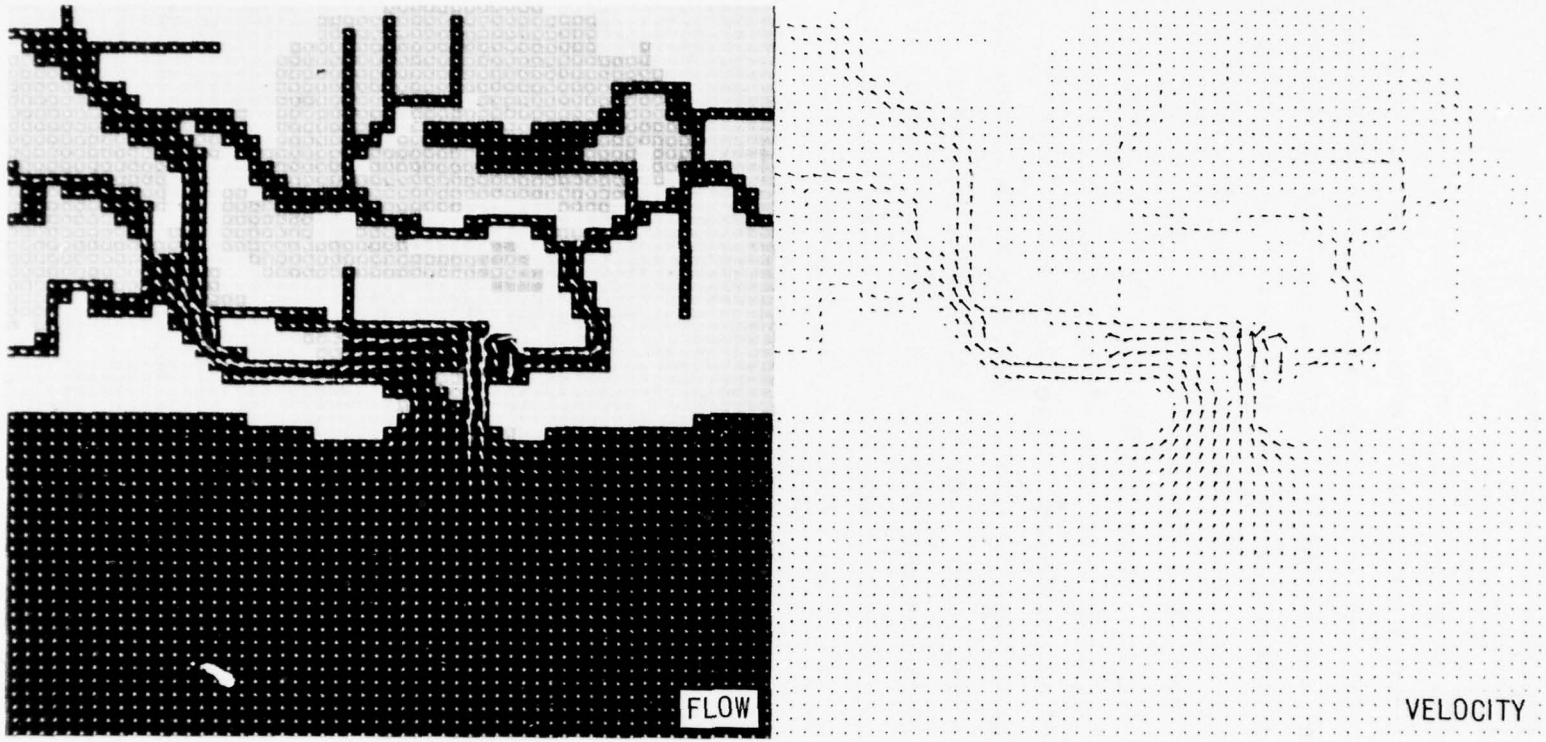

Figure 27. Comparison of unit flow and velocity patterns at 1900 EST for verification runs of Corson Inlet

given: (a) instantaneous depth-averaged unit flows at each point in the plot area, and (b) instantaneous depth-averaged velocities. The flow patterns given in part (a) of these figures were made from colored slides. The lightest background indicates land and the dark background water. The shaded area indicates terrain which was exposed at low-water level but was flooded at the time appropriate to the plot. Such flow plots indicate the amount and direction of water flowing through a given cross section at a given time. A vector with length equal to a cell width represents a flow of 50 ft^2/sec. The velocity patterns shown in each figure correspond closely to surface current patterns, giving a more accurate description of the circulation and flushing characteristics of the system. These plots were obtained from black/white microfilm and exposed land is indicated by the absence of a vector. A vector with length equal to a cell width represents a velocity of 4 ft/sec. Both flow and velocity plots for verification at every 1/2 hour of the computation are available in microfiche form and are attached to the back cover of this report (Appendix E, Card F1). The examples displayed show the tendency of the flow to remain confined to the main channels in both flood and ebb stage. A major characteristic of the flow patterns is the well-formed eddy behind Peck Beach in the vicinity of gage NC.

46. Mean tide levels and volumetric discharges across various velocity ranges (Figure 17) were calculated by the model for a 12-1/2-hour tidal cycle extending from 0730 to 2000 hours EST. A tabulation of these results for 10 ranges is given in Table 3. Since the tidal cycle is asymmetric (Figure 19) the discharges during flood and ebb in the above table do not agree. Ranges 1, 2, and 3 are at the entrances of the back bay system. The net discharge of water into the back bay system was approximately 3.0×10^8 ft^3 during the particular cycle under investigation. Ranges 4 and 5 indicate that the total inflow through the inlet throat during the cycle under investigation is split between the two branches as follows: 70 percent through the Strathmere reach and 30 percent through the Peck Beach reach. No prototype data were available to verify discharges through velocity ranges.

Great Egg Harbor Inlet

47. The problems encountered with the Corson Inlet prototype data were prevalent in the field survey data for Great Egg Harbor Inlet (GEI). The model for GEI was verified by simulating existing conditions for 9 June 1975. Comparisons were made between prototype and model for a single tide gage and 10 velocity gages. The study region for GEI, showing gage locations, is depicted in Figure 18.

48. Again, major discrepancies were noted in the phasing of the tides used at the interior boundaries. The ocean gage tidal data supplied by NOS agreed closely with the predicted amplitudes and phases. A phase lead existed for all interior prototype gage data relative to the tide tables. Thus, it was necessary to shift the tide data forward in time at the following gages:

Great Egg Tide Gage No.	Name	Phase Lead min
2	Roosevelt Bridge	20
3	Gateway Marina	20
4	Mainland Marina	25
6	Alton Marina	10

Figure 28 is a plot of the six tidal hydrographs used as boundary conditions for the 9 June 1975 verification. For an approximation of the tide at Whirlpool Channel (gage 5), an average between gages 4 and 6 was used in the absence of prototype data. Figure 29 shows the comparison of tidal elevation between model and prototype for the Ocean City Coast Guard gage (gage 7). Again, there is a discrepancy in the gage results which is apparently due to an error in the benchmark used. The amplitude response indicated in the tide tables agrees with the numerical results. Gage 7 provided the only prototype tide data for use in verifying the model.

49. Comparisons between prototype and calculated velocities are drawn in Figures 30 and 31. The comparisons show good agreement at most gages. More recent bathymetric data for the back bay area would

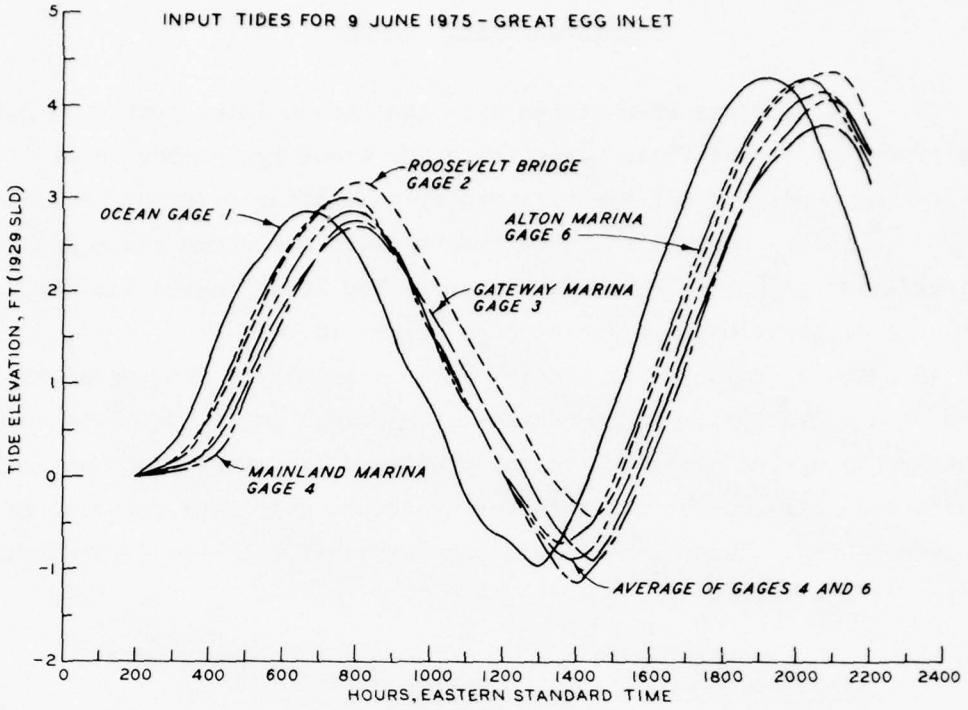

Figure 28. Forcing tides for Great Egg Harbor Inlet model

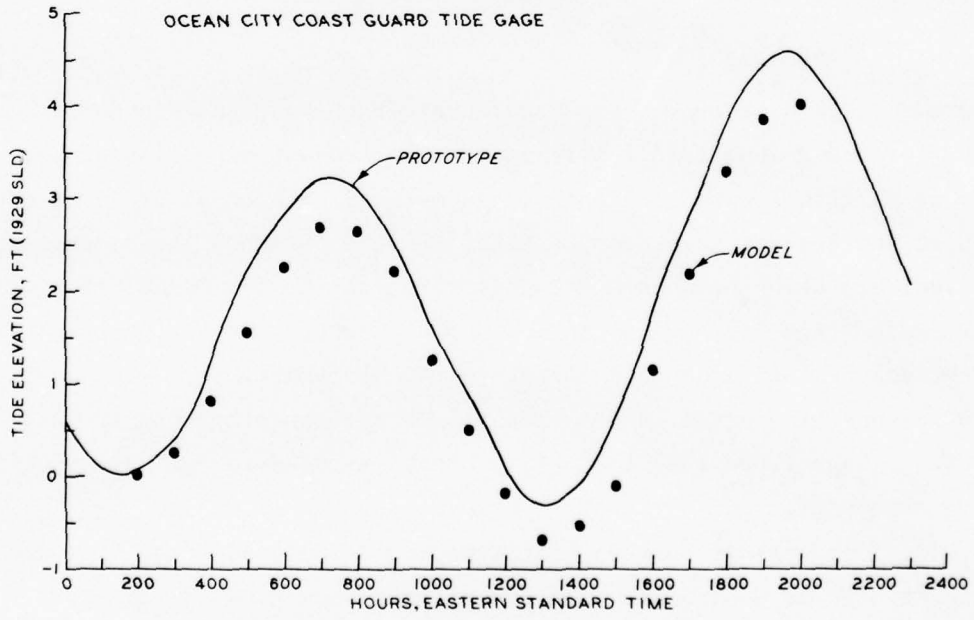

Figure 29. Comparison of surface elevation agreement with prototype for the Ocean City tide gage

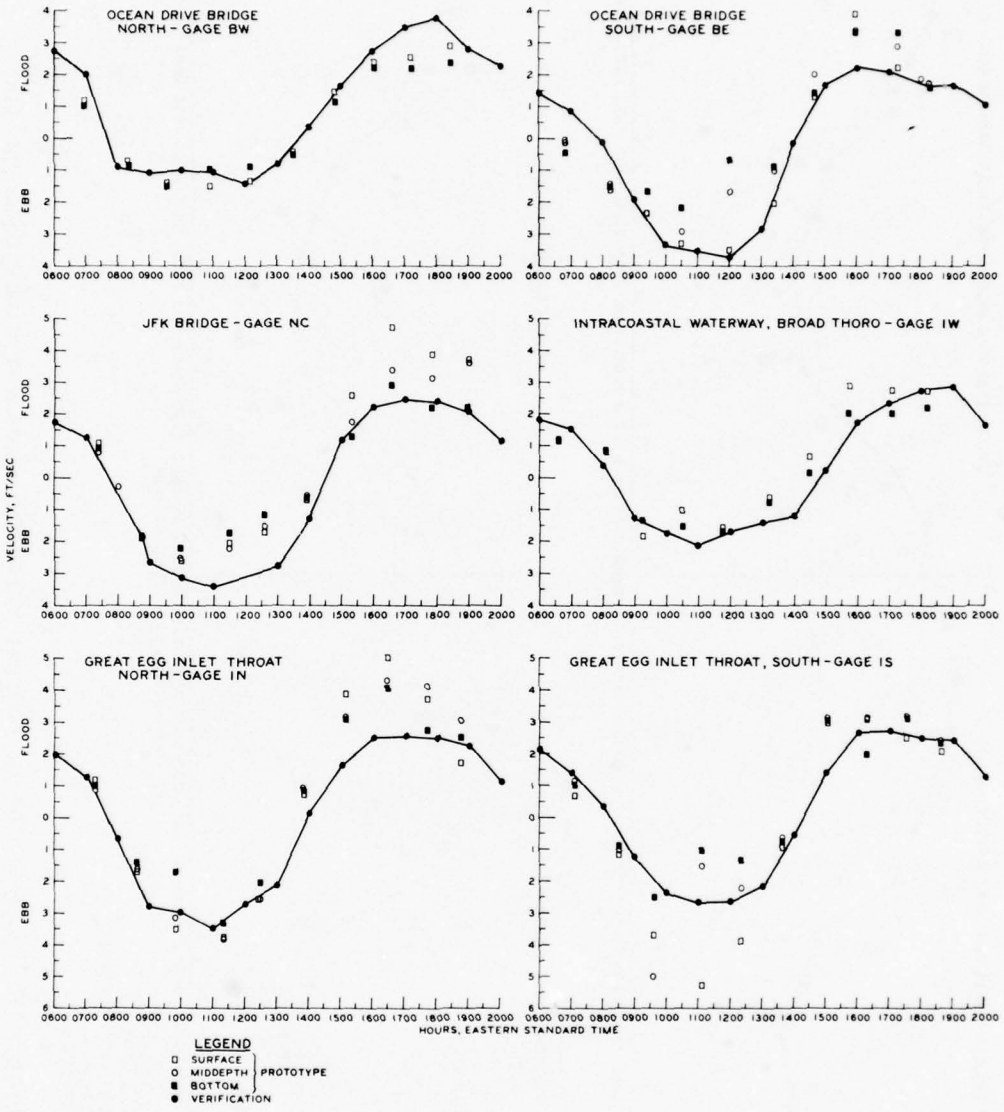

Figure 30. Comparison of current velocity agreement with prototype for Great Egg Harbor Inlet base gages BW, BE, NC, 1W, 1N, and 1S

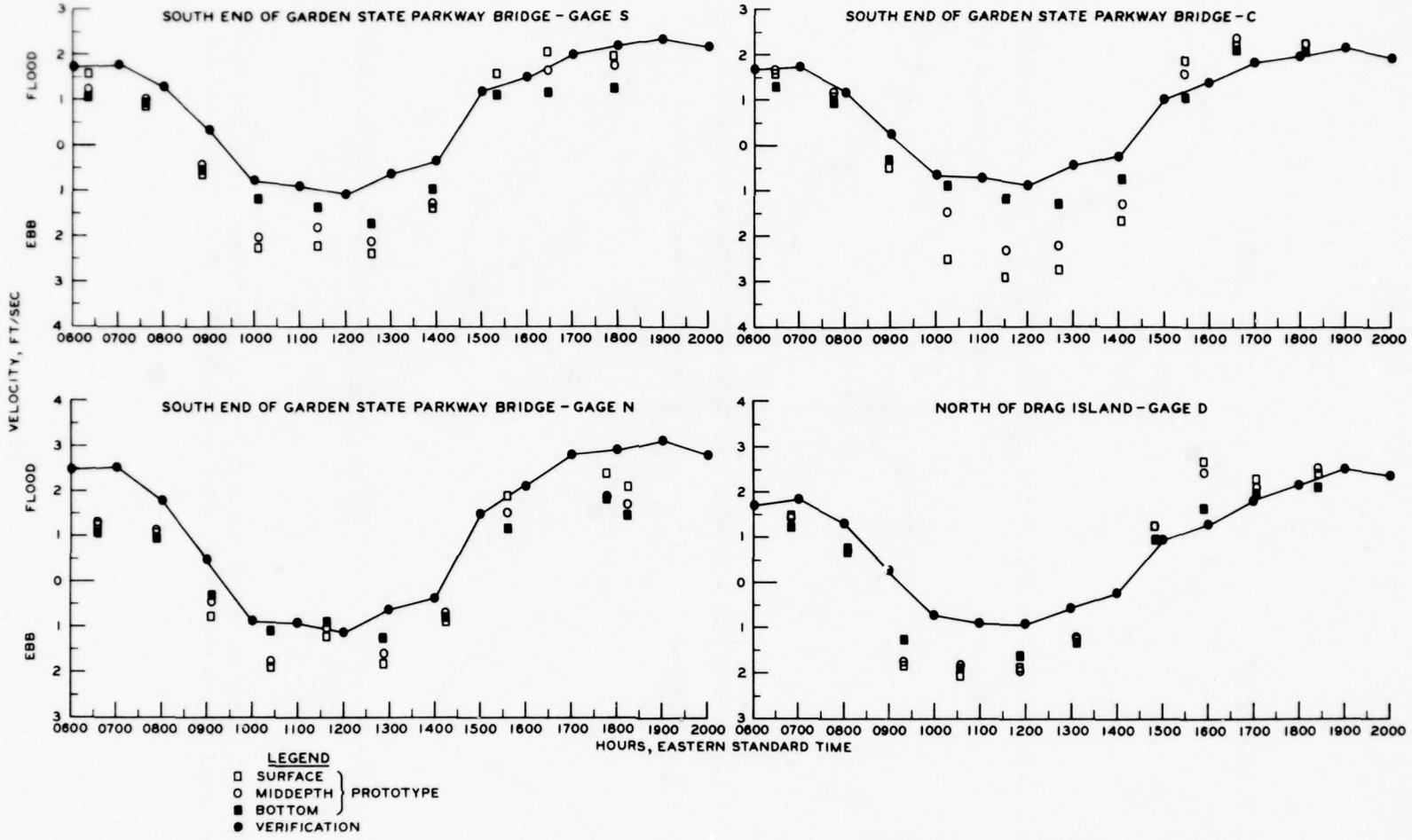

Figure 31. Comparison of current velocity agreement with prototype for Great Egg Harbor Inlet base gages S, C, N, and D

be required to obtain better agreement. This is particularly true for gages S, C, N, and D in the Garden State Parkway Bridge areas. The accuracy of the field survey data did not warrant additional effort to obtain a better agreement.

50. Circulation patterns for the GEI throat area (3760 points) are presented in Figures 32-35 for four times in the tidal cycle. Both unit flow and velocity vector patterns are given. The flow diagrams were made from colored slides and the velocity diagrams from microfilm. Flow and velocity plots for verification at every 1/2 hour of the computation are available in microfiche form and are attached to the back cover of this report (Appendix E, Card F2). The examples chosen show the tendency of the flow to remain confined to the deep entrance channel at flood stage and a tendency to move over the large shoal area off Ocean City during ebb stage. There is some erratic behavior in the velocity field (Figure 35) in the channel area immediately to the north of Ocean City. Time and funds were not sufficient to completely resolve the reason for this behavior, and it is not recommended that direct quantitative comparisons be made in this area for existing conditions and the various improvement plans. However, it was ascertained that this behavior, whether real or not, had a negligible effect on computed data in the inlet throat and estuary. No prototype data were available for comparison of the velocity fields.

51. Mean tide levels and volumetric discharges across various velocity ranges (Figure 18) were calculated for a 12-1/2-hour tidal cycle extending from 077 EST to 1930 EST. A tabulation of results for 14 ranges is given in Table 4 (listed as base condition). As for Corson Inlet, a check was made on the net discharge of water into the system over the chosen tidal range. Ranges 1-7 are at the entrances of the back bay system. The net discharge of water into the system was approximately 2.7×10 ft^3 during the particular cycle under investigation. Ranges 8-11 indicate that the inflow through the inlet throat during this cycle was primarily directed toward the southern portion of the system.

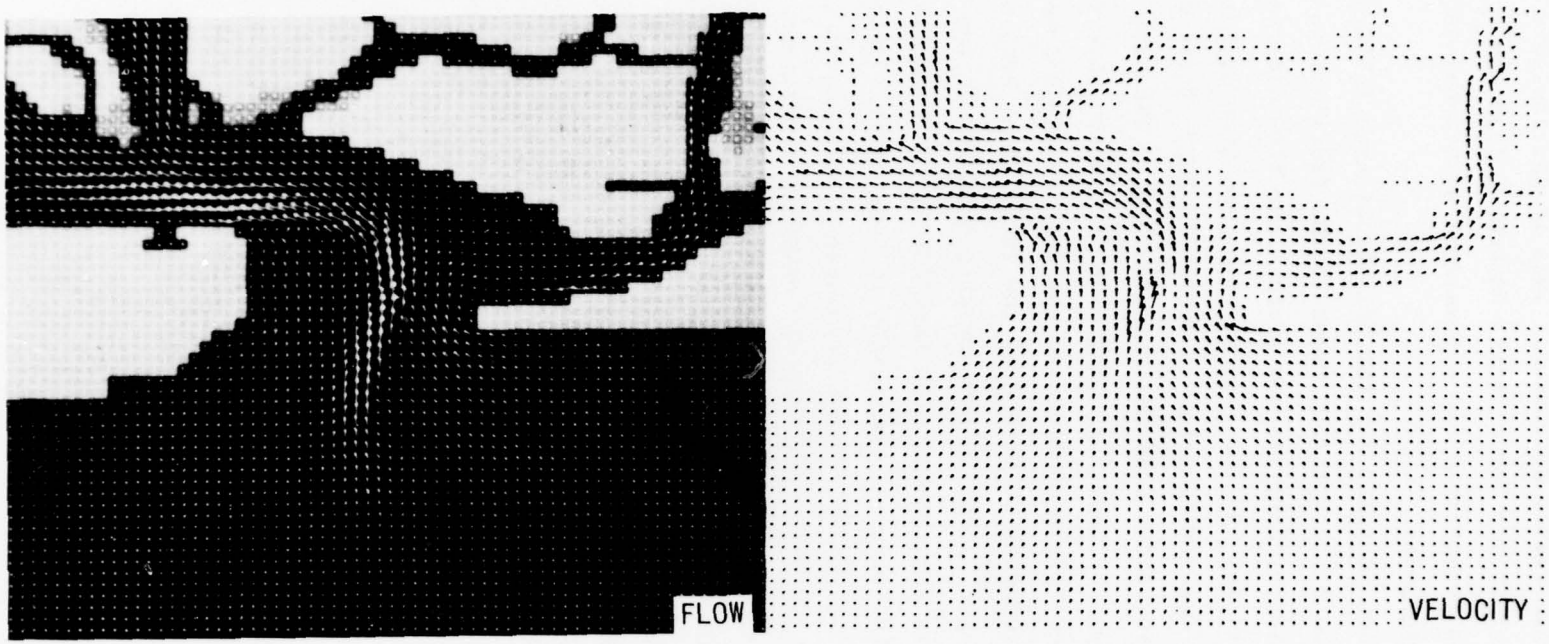

Figure 32. Comparison of unit flow and velocity patterns at 0500 EST for verification run of Great Egg Harbor Inlet

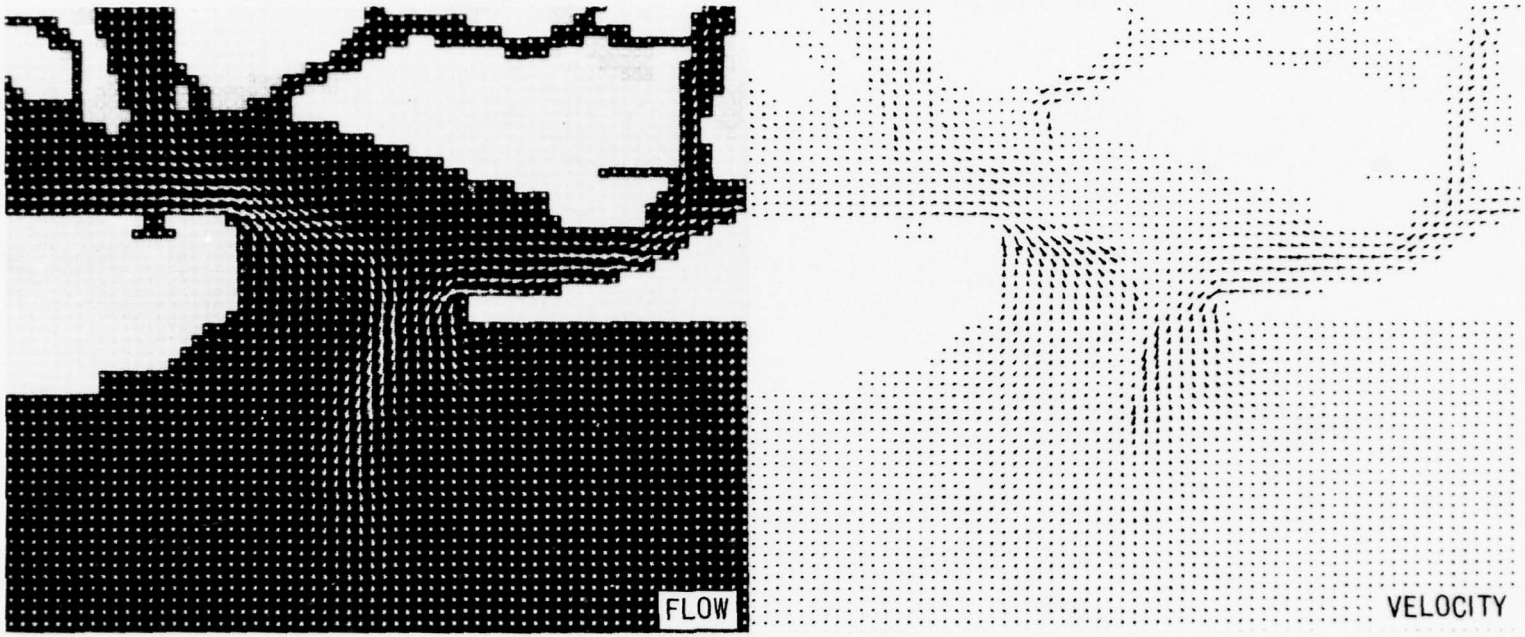

Figure 33. Comparison of unit flow and velocity patterns at 0900 EST for verification run of Great Egg Harbor Inlet

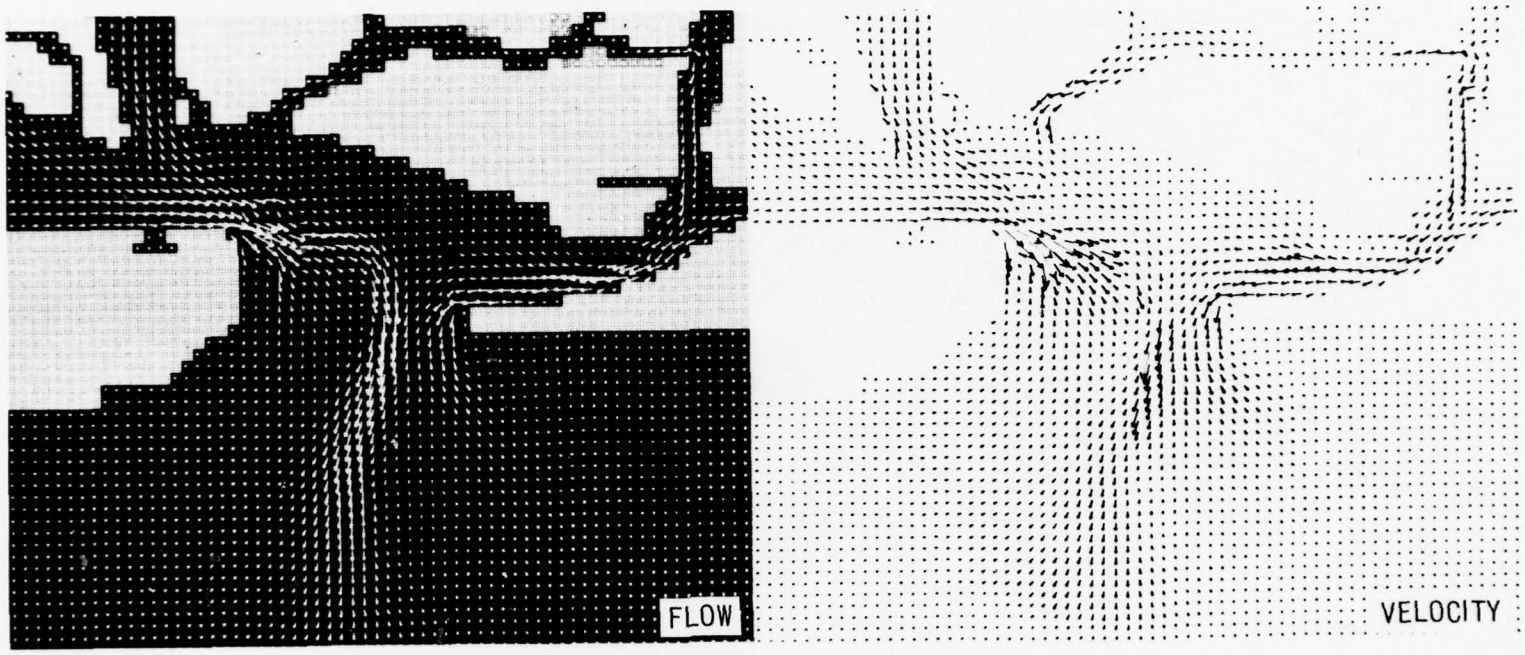

Figure 34. Comparison of unit flow and velocity patterns at 1100 EST for verification run of Great Egg Harbor Inlet

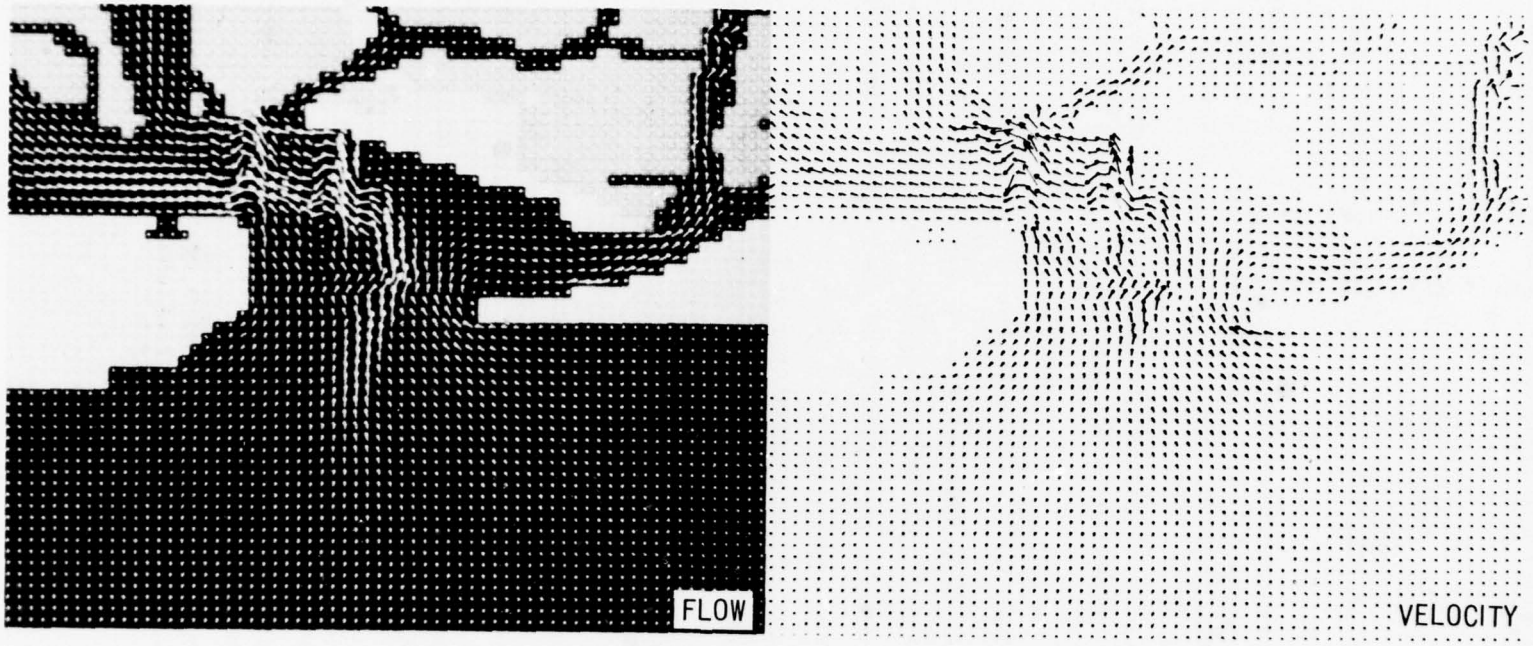

Figure 35. Comparison of unit flow and velocity patterns at 1900 EST for verification run of Great Egg Harbor Inlet

PART VII: ALTERNATE IMPROVEMENT PLAN CONFIGURATIONS

Inlet Modifications

52. The major problem conditions affecting the GECI area are purported to be:

a. The presence of a shifting sandbar on the updrift side of Corson Inlet, which has almost closed the inlet, making passage through the inlet difficult, hazardous, and at times impossible.

b. The existing channel in Great Egg Harbor Inlet is unsafe for navigation except under ideal conditions of tide and wind.

In general, the outer shoal areas adjacent to both inlet channels are reported to produce sharp ground swells at all stages of tide. Waves break across both inlet openings during low stages of tide which, combined with ground swells, make passage of small craft almost impossible. Many local boat owners have relocated elsewhere. In order to eliminate these problems, plans of improvement for each inlet have been considered. Two plans for Corson Inlet and three plans for Great Egg Harbor Inlet were recommended for testing by NAPEN.

53. The basic improvement plans authorized for each inlet are similar. In general, they provide for:

a. A jetty for navigation protection and beach erosion control located on the updrift side (northern side) of each inlet. The jetty includes a low-water weir section and is designed to intercept southerly littoral drift and prevent movement into the inlet channel by causing the drift to be trapped in a deposition basin for later transferral across the inlet to the southern beaches.

b. The construction and maintenance of specified navigation channels.

c. A bulkhead and jetty system located on the downdrift side of each inlet.

d. An optional development of a landfill area adjacent to the bulkhead for public recreational use.

Improvement Plans for Corson Inlet

54. Tests of two proposed plans of improvement were conducted with the 1974-1975 hydrographic conditions and the 10 June 1975 tidal conditions of the Corson Inlet system. Figure 36 depicts both plans which are identified as Plan AA and Plan CC. These plans included:

a. A 3225-ft-long weir-jetty system extending seaward from Peck Beach with a 2000-ft-long low-weir section having a top elevation of 0.0 SLD.

b. A 33-acre deposition basin (bottom elevation -29 ft SLD) located immediately west of the low-weir section.

c. A 300-ft-wide entrance channel extending to the -14 ft bottom contour and maintained at -14 ft SLD.

d. A 100-ft-wide bay channel (to be maintained at -8 ft SLD) linking Strathmere reach and the entrance channel.

For the downdrift side of the inlet the improvement plans included:

a. For Plan AA, a 3900-ft-long bulkhead-jetty system extending from the northern end of Strathmere along the inlet frontage for 1200 ft (bulkhead) and then seaward for 2700 ft (1100-ft bulkhead and 1600-ft jetty).

b. For Plan AA, the fillet between the jetty and the bulkhead was backfilled with sand to an elevation of +6 ft SLD.

c. For Plan CC, the bulkhead-jetty-fill area system was replaced by a 2800-ft-long dogleg jetty.

Plan AA results

55. Figures 37 and 38 show the comparison of tidal elevations with Plan AA installed using the verification results as a base condition. With this plan installed it was noted that tidal elevations were not significantly changed with the exception of the period between 1100 and 1600 hours EST (low water). During this period the flow through Middle Thoro was very sensitive to any change in input data such as a change in the tidal boundary conditions or the introduction of an improvement plan. In order to alleviate the problem, more accurate hydrographic survey data for the back bay area would be necessary. In particular,

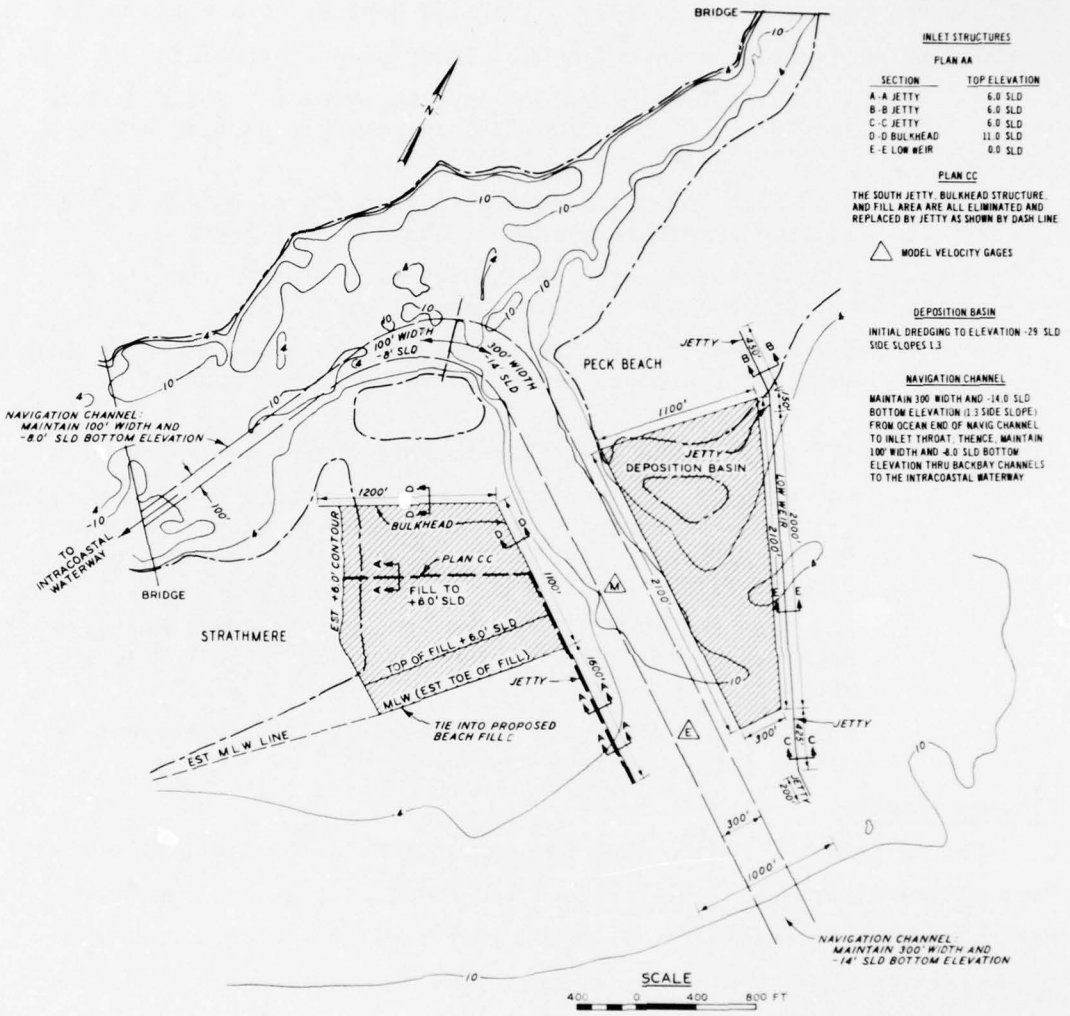

Figure 36. Proposed improvement plans for Corson Inlet

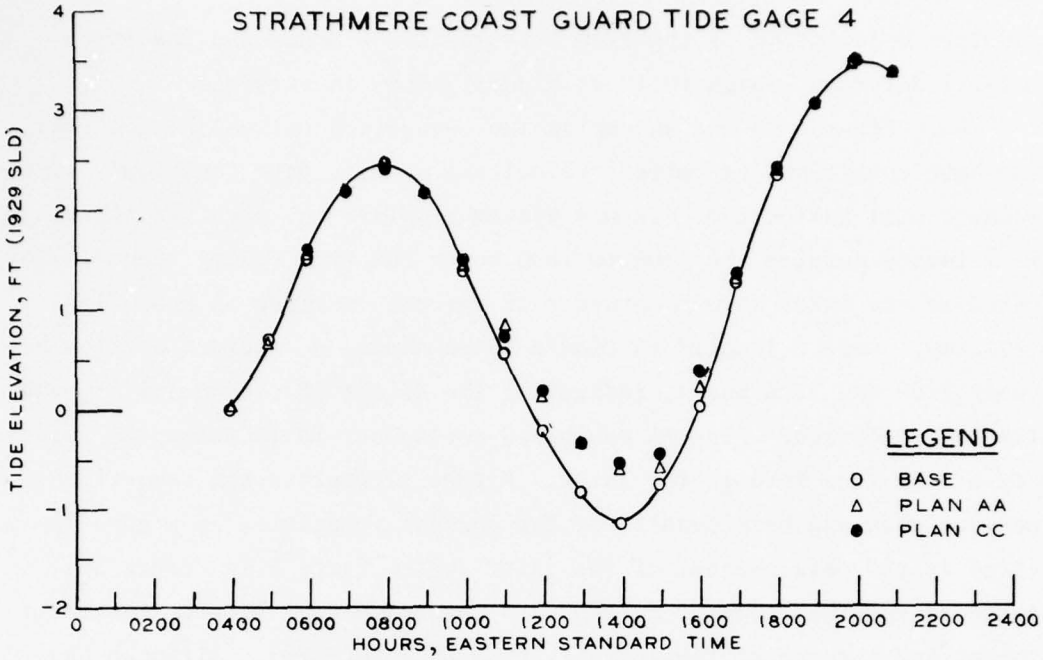

Figure 37. Comparison of surface elevations (plan to base) for the Strathmere tide gage

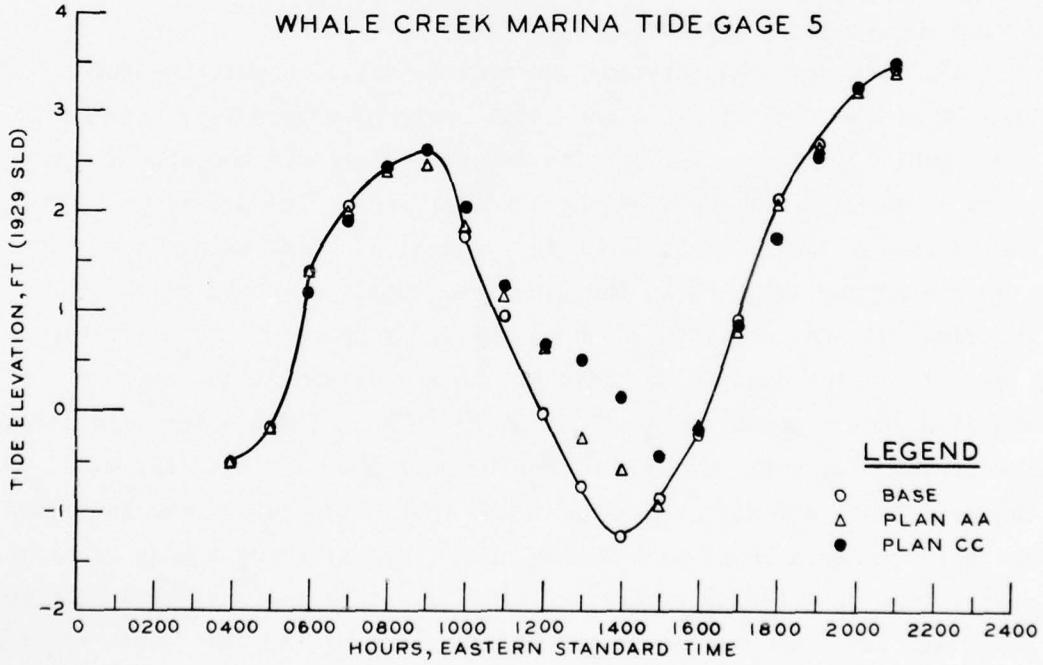

Figure 38. Comparison of surface elevations (plan to base) for Whale Creek Marina tide gage

a better description of the flow between Corson Sound and the Intracoastal Waterway (which includes Middle Thoro) is required.

56. Figures 39 and 40 depict the comparison between Plan AA and the base condition for current velocities at base gage locations. Gages located well inside the back bay system displayed no significant change in velocity outside the 1100 to 1600 hours EST time frame. Gage IN located in the inlet throat showed a 15 percent increase in peak flood velocity. Gage C located in Middle Thoro showed a reversal of flow between 1200 and 1300 hours, indicating the effect of the numerical problem that occurred. Plan AA exhibited a tendency to increase the velocity of the flow through the inlet. Figure 41 depicts the comparison between plan and base conditions for current velocities at a gage located in the main channel of the jetty system (gage E in Figure 36). A second gage was located in the main channel midway between the inlet throat and the end of the jetty (gage M in Figure 36). Although the increased flow rates cannot be quantified due to the numerical problem occurring between 1100 and 1600 hours, the tendency to increase the flow during ebb stage is apparent.

57. Figures 42-45 display the vector unit flow patterns for Plan AA at the same times in the tidal cycle used for displaying the base results (Figures 24-27). The downcoast jetty in the velocity patterns is shown extending from the landfill area. The prevalent eddy behind Peck Beach noted in the base results was still maintained. The plan did appear to keep the the flow well confined to the main channel. The flow pattern in Figure 44 shows the development of a small circulation cell in the deposition basin at the end of ebb stage. Figures 42 and 45 depict a confusion in the flow pattern at flood stage, indicating the mixing of a substantial flow coming over the weir with the main channel flow. A finer mesh size in the throat area would aid in alleviating the computational problems in this area, allowing a more accurate description of the flow pattern. The weir action appears sufficient to alleviate sand impoundment on the updrift side of the weir-jetty system. Both flow and velocity plots for Plan AA conditions at every 1/2 hour of the computation are available in microfiche form in Appendix E.

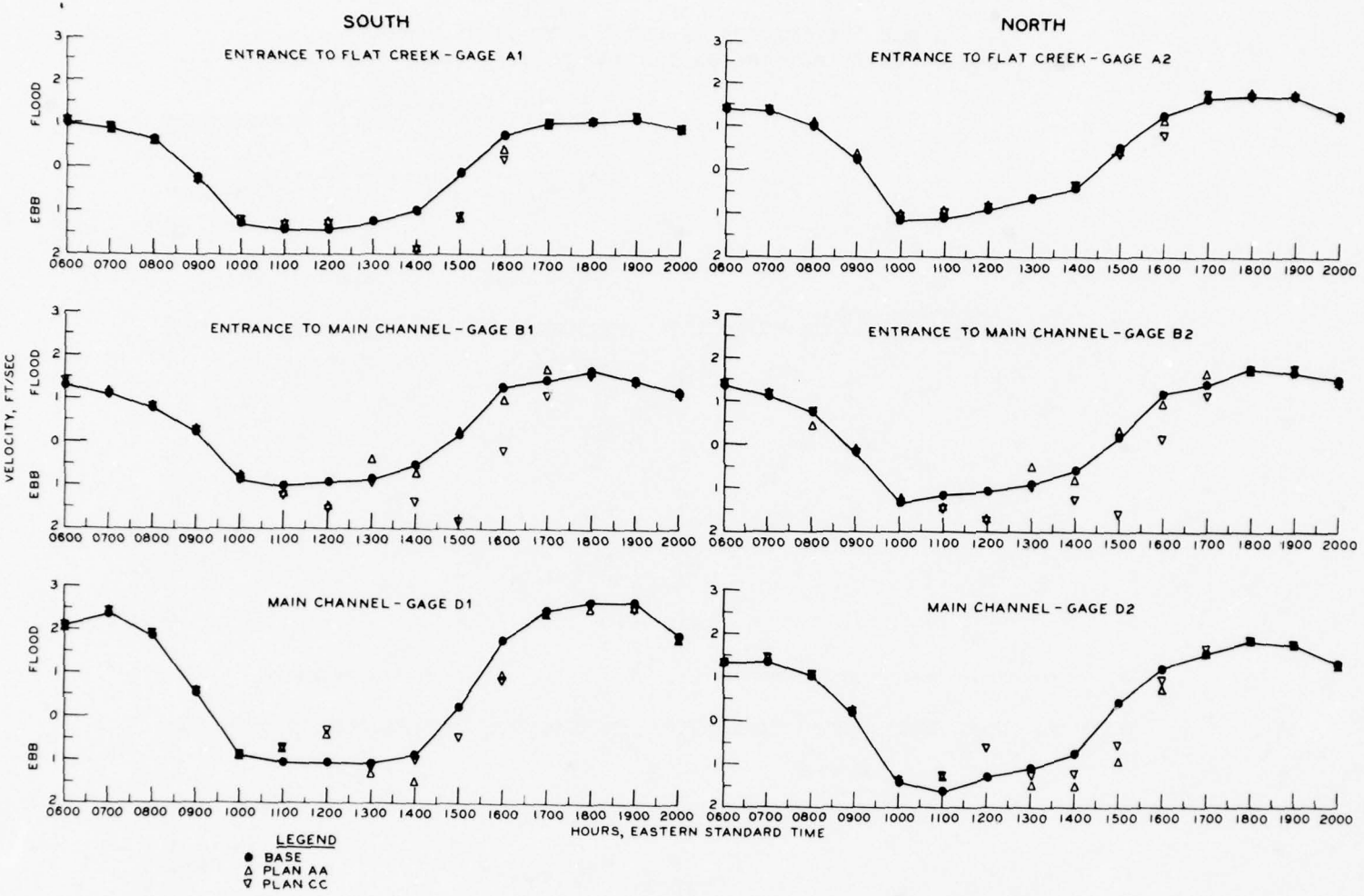

Figure 39. Comparison of current velocities (plan to base) for Corson Inlet base gages A1, A2, B1, B2, D1, and D2

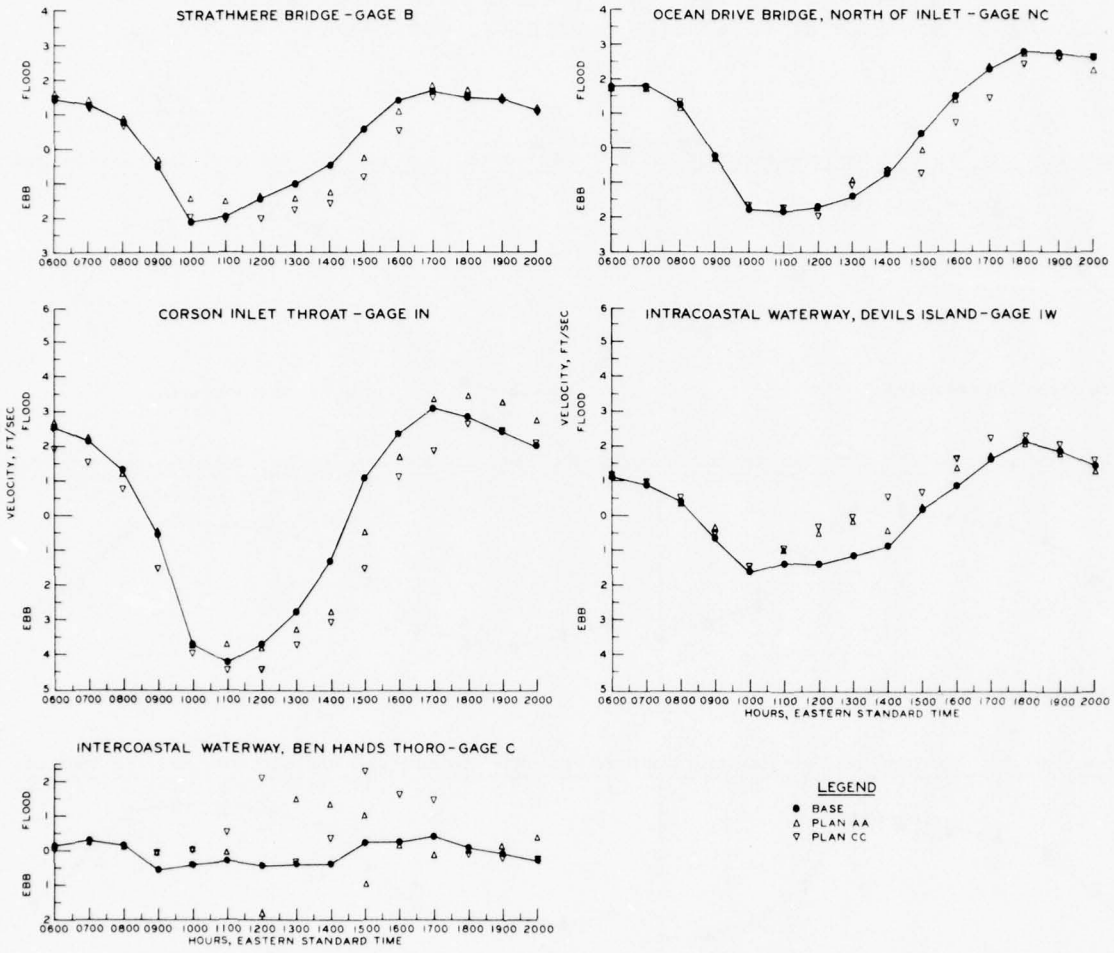

Figure 40. Comparison of current velocities (plan to base) for Corson Inlet base gages B, NC, IN, IW, and C

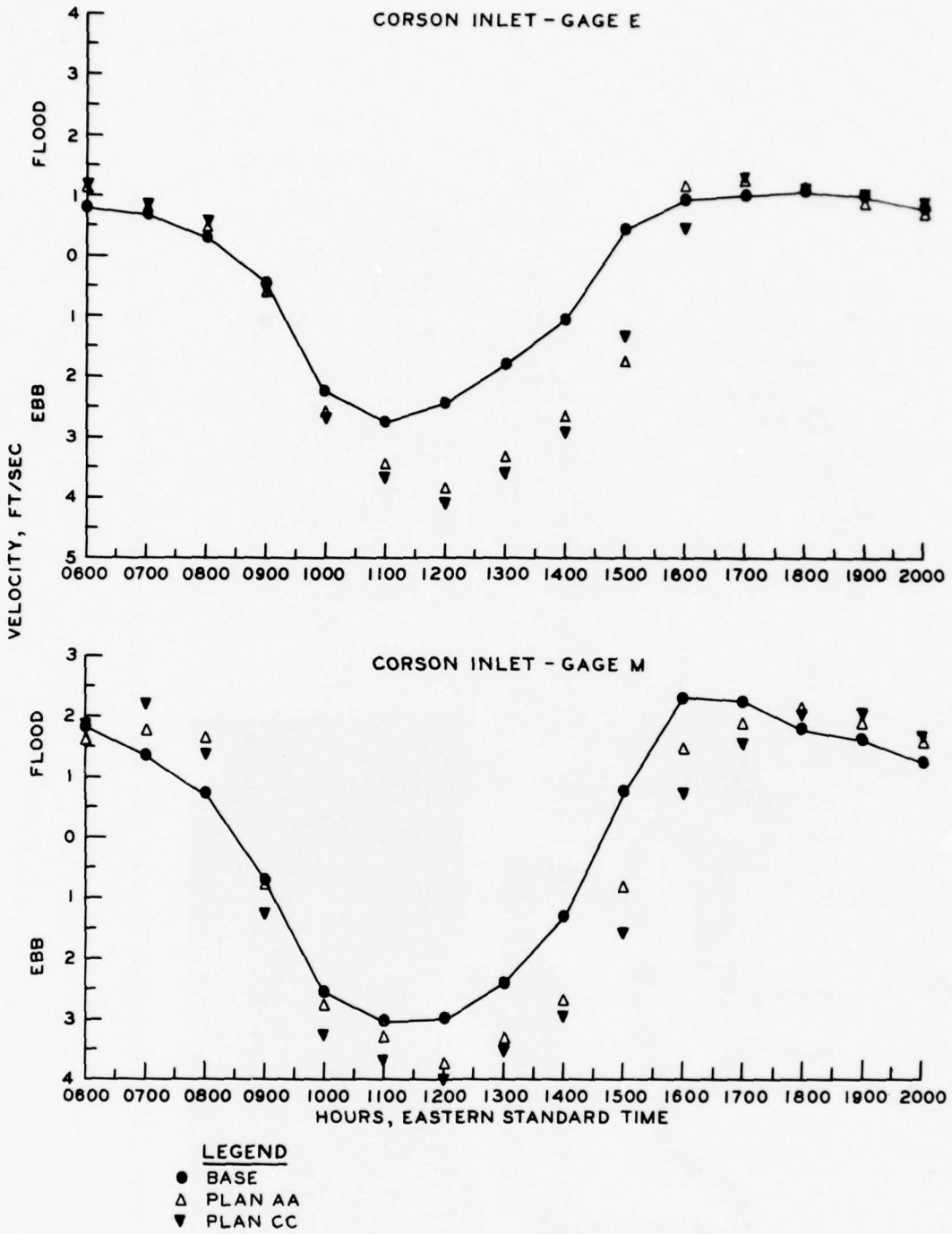

Figure 41. Comparison of current velocities in main channel (plan to base)

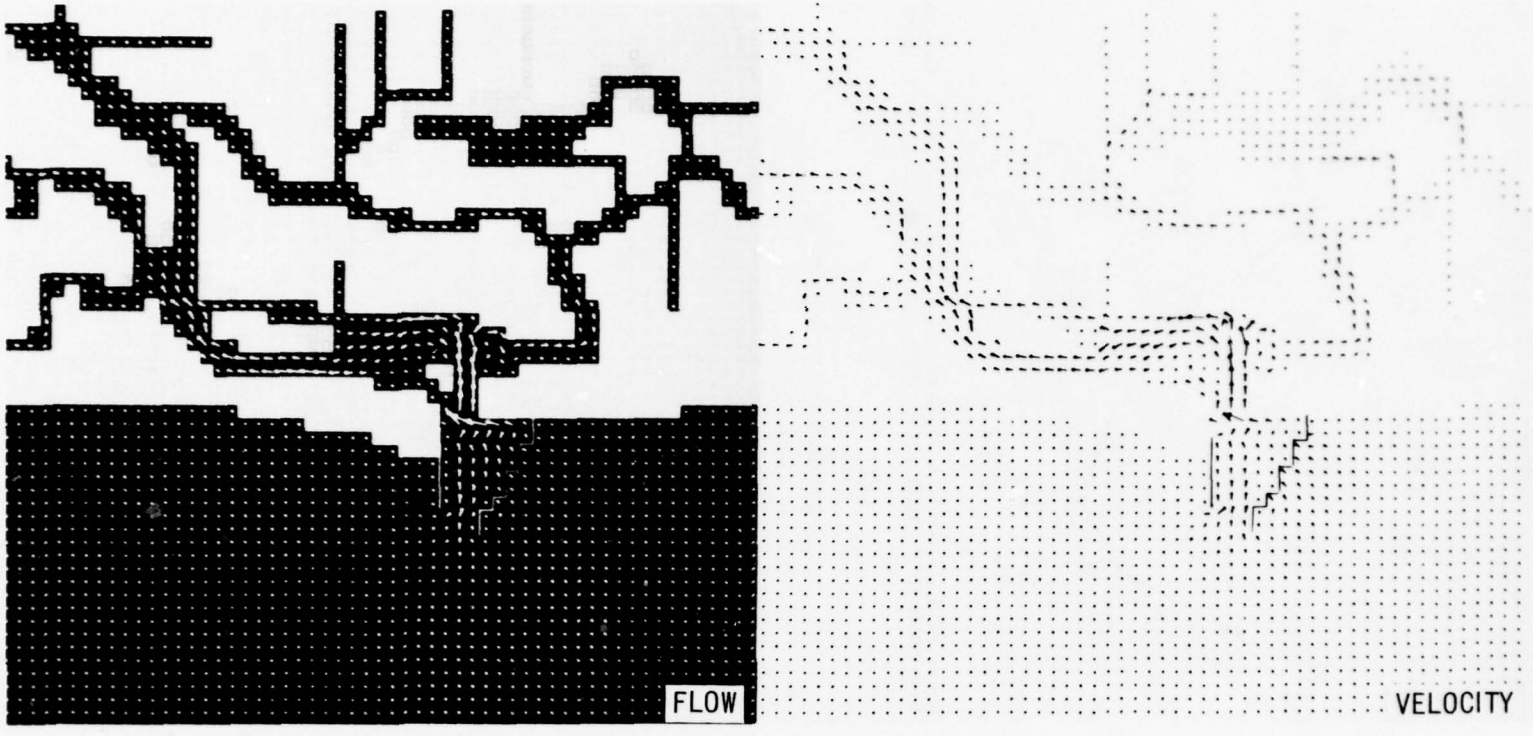

Figure 42. Comparison of unit flow and velocity patterns at 0600 EST for Plan AA

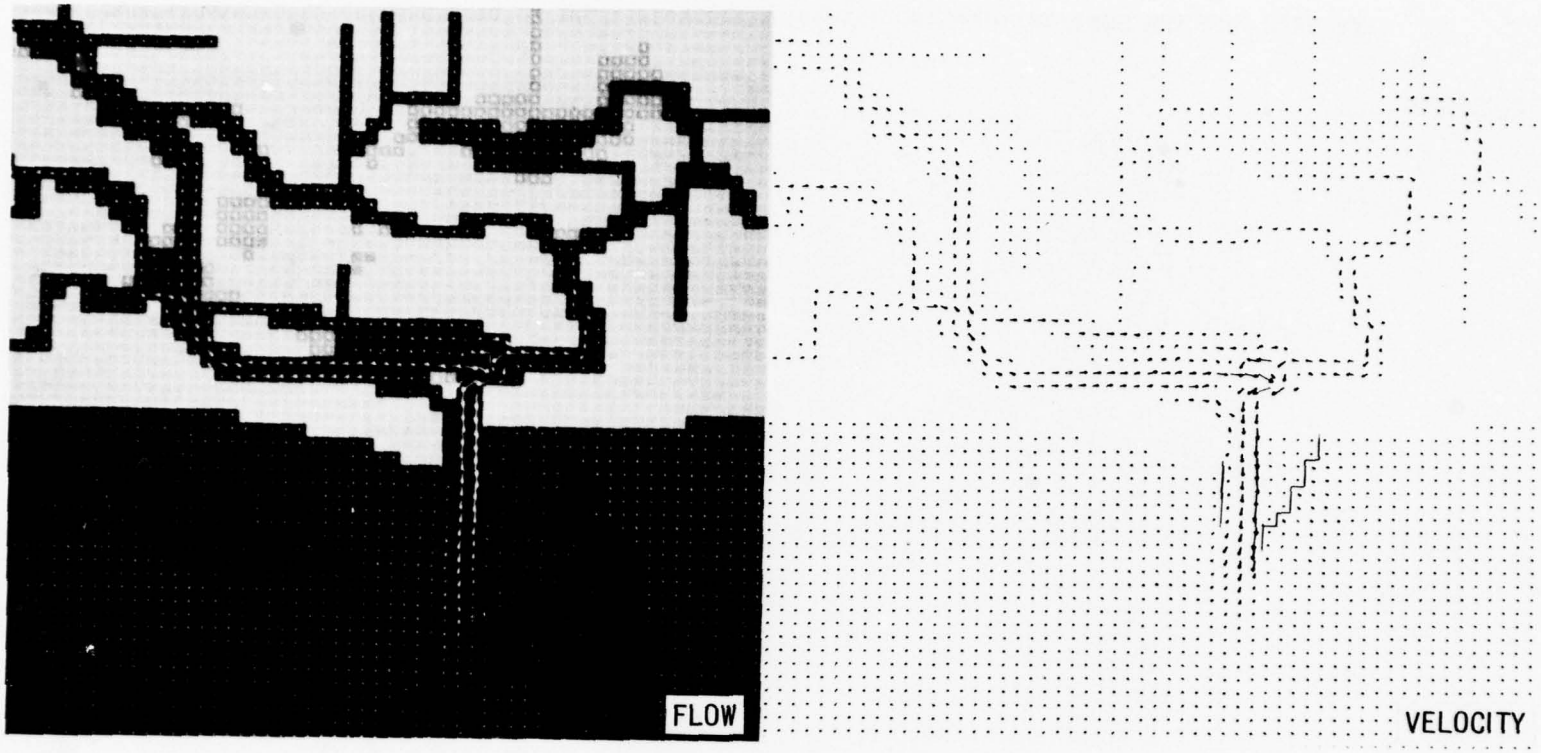

Figure 43. Comparison of unit flow and velocity patterns at 1000 EST for Plan AA

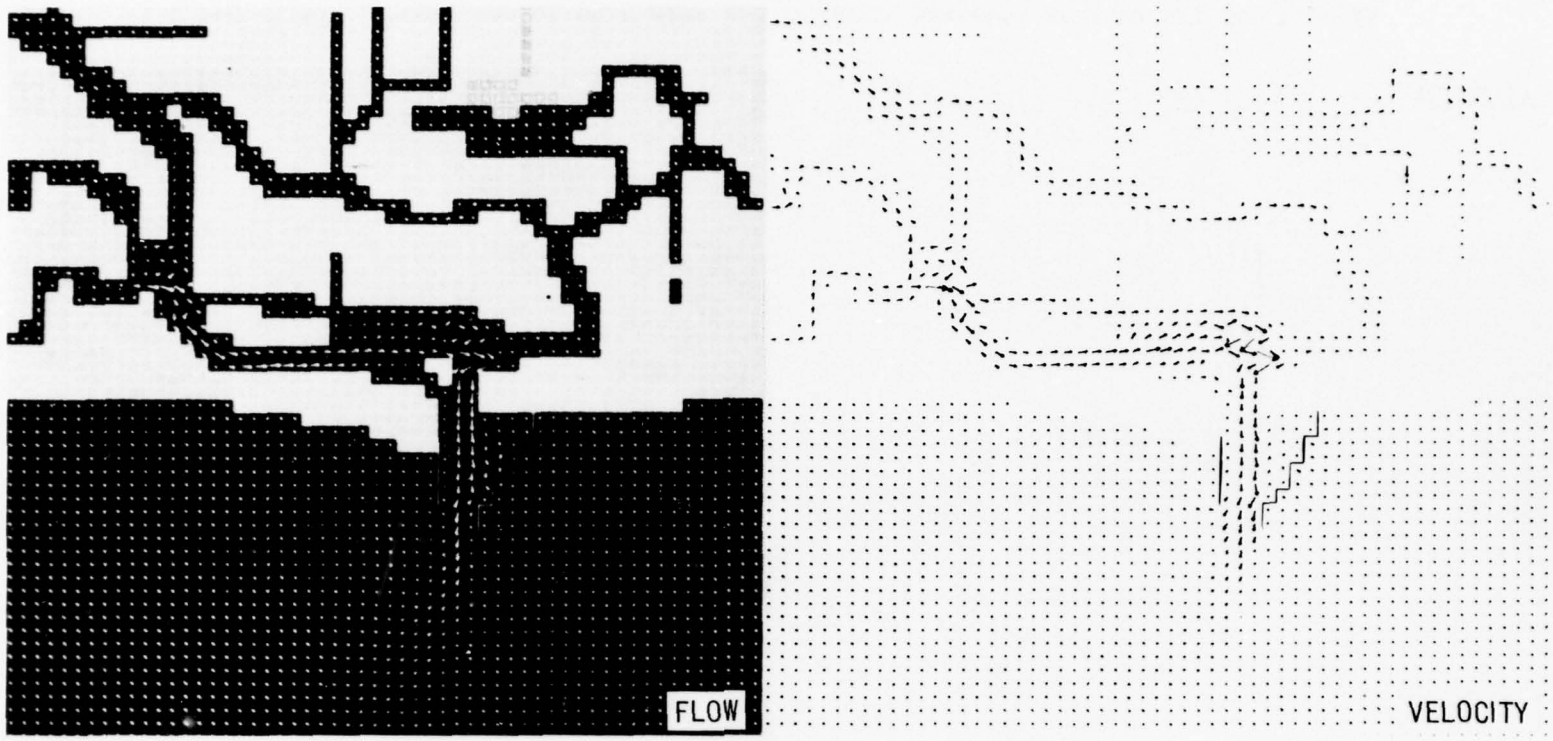

Figure 44. Comparison of unit flow and velocity patterns at 1400 EST for Plan AA

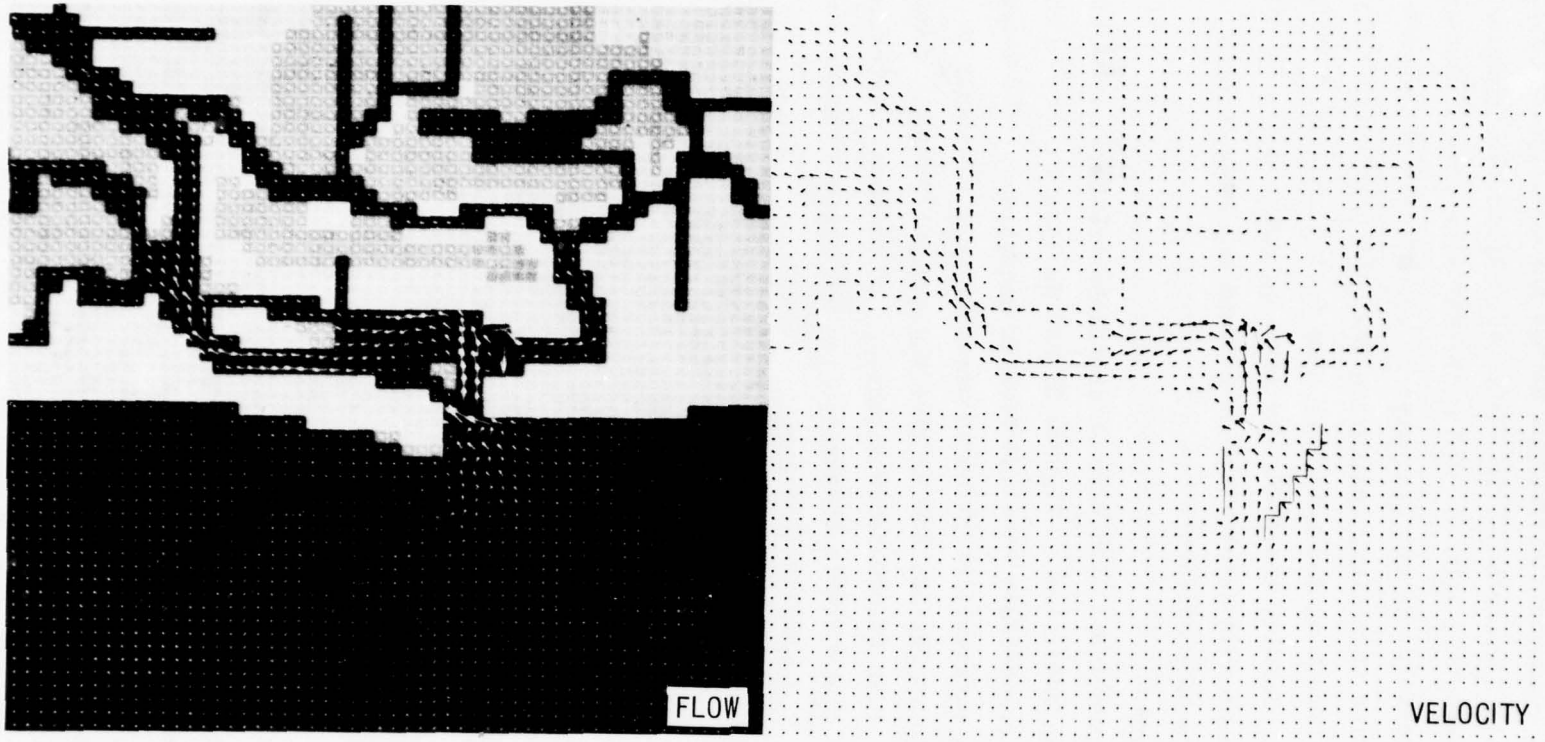

Figure 45. Comparison of unit flow and velocity patterns at 1900 EST for Plan AA

58. The volumetric discharges across three of the ten ranges listed in Table 3 are plotted in Figure 46. Again the numerical problem is evident during the 1100 to 1600 hours EST time frame. Outside of this time interval, the net discharge is essentially the same with and without the plan installed, indicating that the plan would tend to have a negligible effect on the net flow. Due to the numerical difficulties experienced in running the plan, the time integration of the discharges would give suspicious results and no attempt was made to draw information from such calculations.

Plan CC results

59. Corson Inlet with Plan CC installed exhibited behavior similar to the Plan AA conditions. Figures 37 and 38 show the comparison of tidal elevations between base and Plan CC conditions. The comments on the numerical difficulties given in previous sections apply to this plan as well. Figures 39, 40, and 41 give the current velocity comparisons for Plan CC. Plan CC does show a tendency to produce greater current velocities in the entrance channel during ebb stage as noted in Figure 41.

60. Figures 47-50 display the vector flow patterns for Plan CC at four times. Without the landfill of Strathmere Beach (Plan AA), more flow was directed during flood stage over the shoal area between the downcoast jetty leg and the tidal delta located just inside the inlet (as seen in Figures 47 and 50). Both flow and velocity plots for Plan CC conditions at every 1/2 hour of the computation are available in microfiche form in Appendix E. Volumetric discharges are plotted in Figure 46. Little difference is noted between results for both improvement plans.

61. Difference plots of unit flow vectors for both proposed plans are given in Figures 51-54. The vector differences were formed by subtracting plan results from base calculations. The direction of the resulting vector will be reversed relative to the proper flow direction if the flow magnitude for the plan is greater than that for the base condition. The effects of both plans are noted to be confined to a localized area near the improvement structures. During peak ebb stage

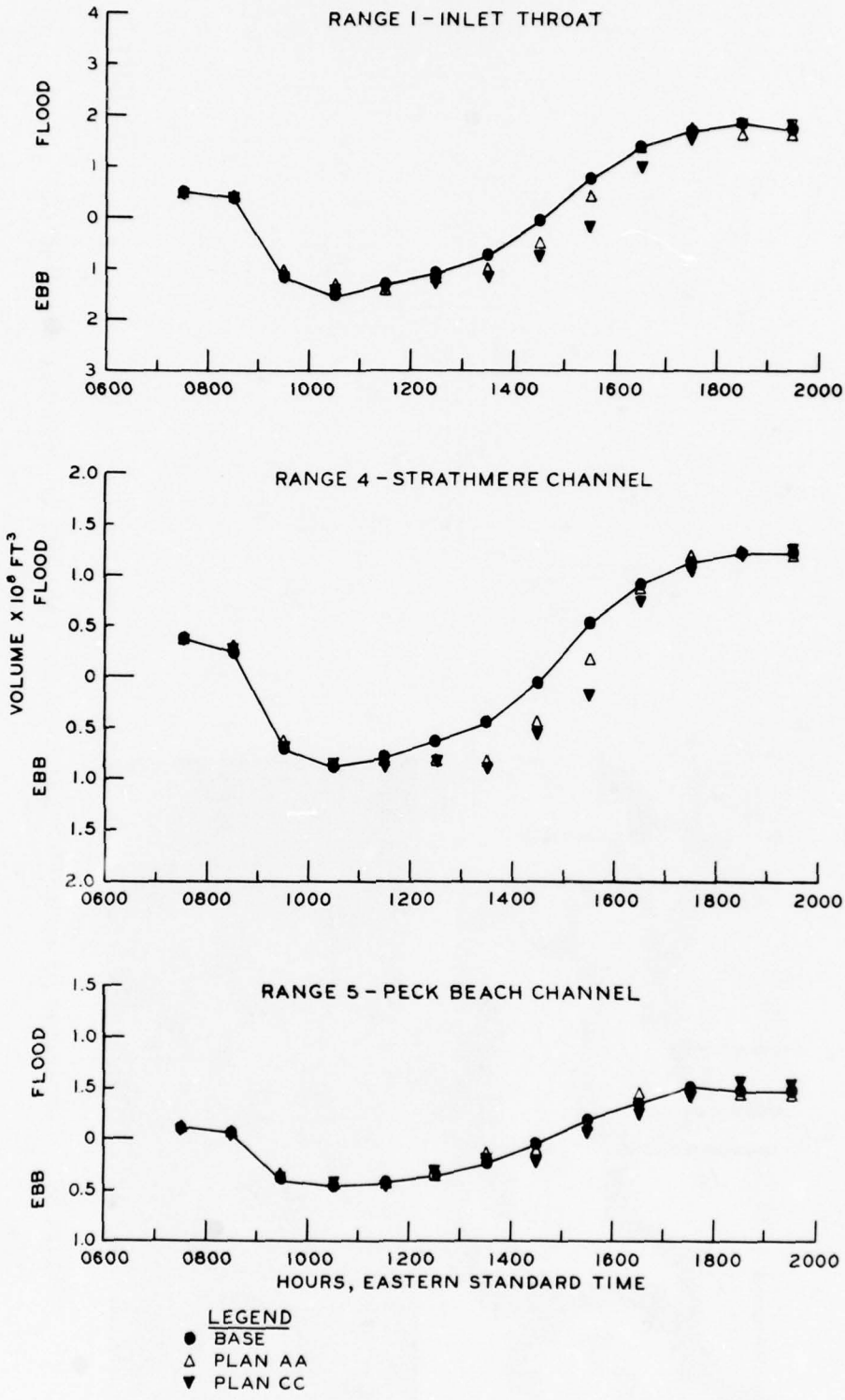

Figure 46. Comparison of volumetric discharges (plan to base) for Corson Inlet

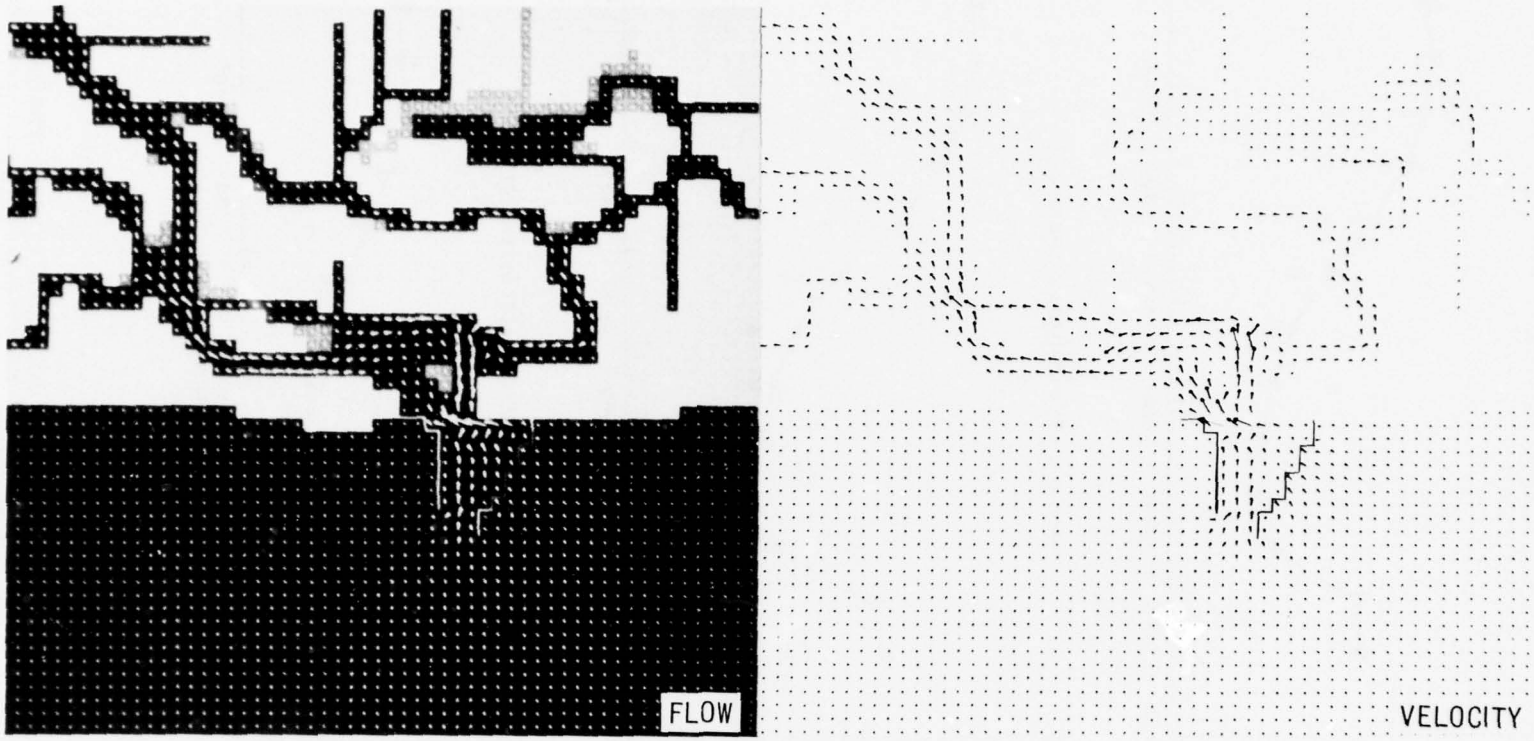

Figure 47. Comparison of unit flow and velocity patterns at 0600 EST for Plan CC

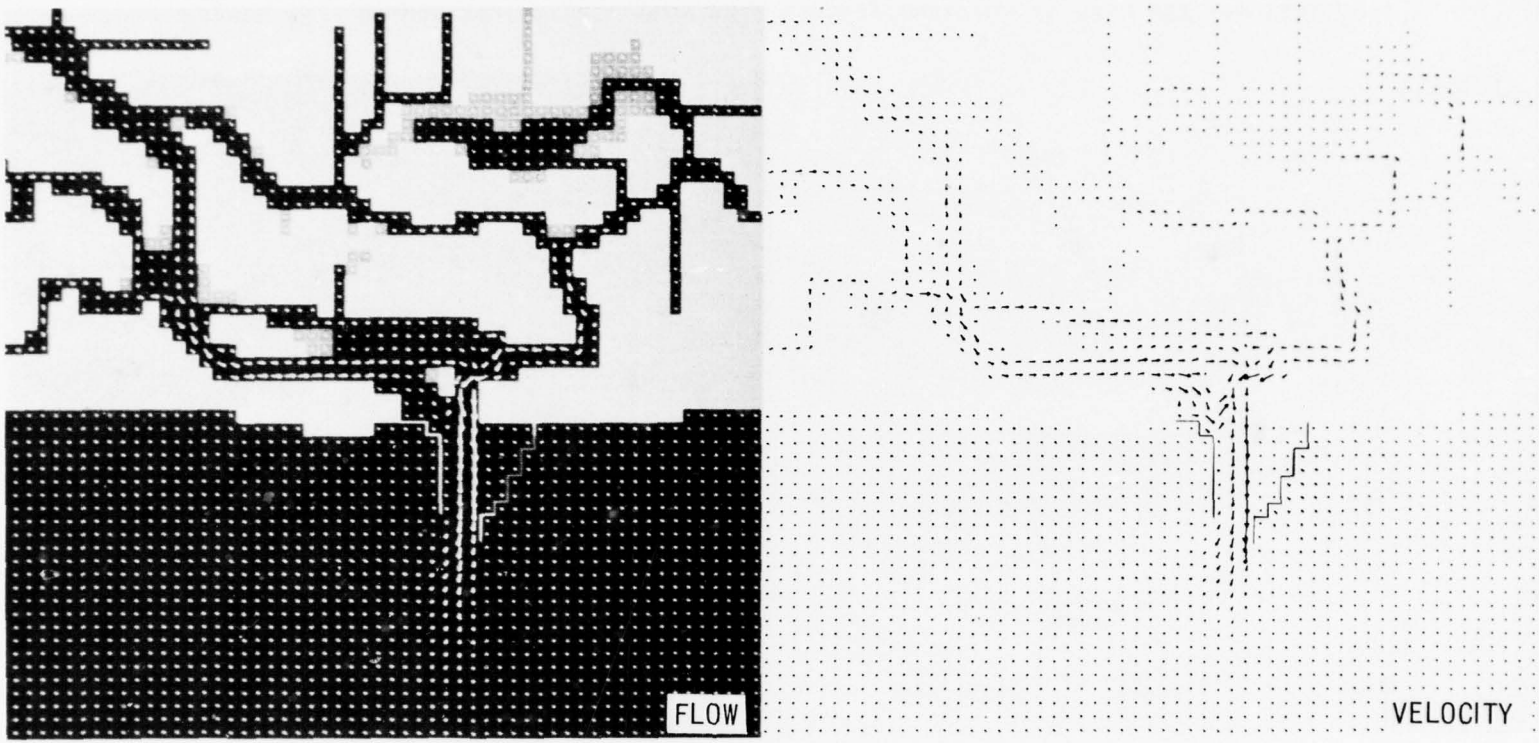

Figure 48. Comparison of unit flow and velocity patterns at 1000 EST for Plan CC

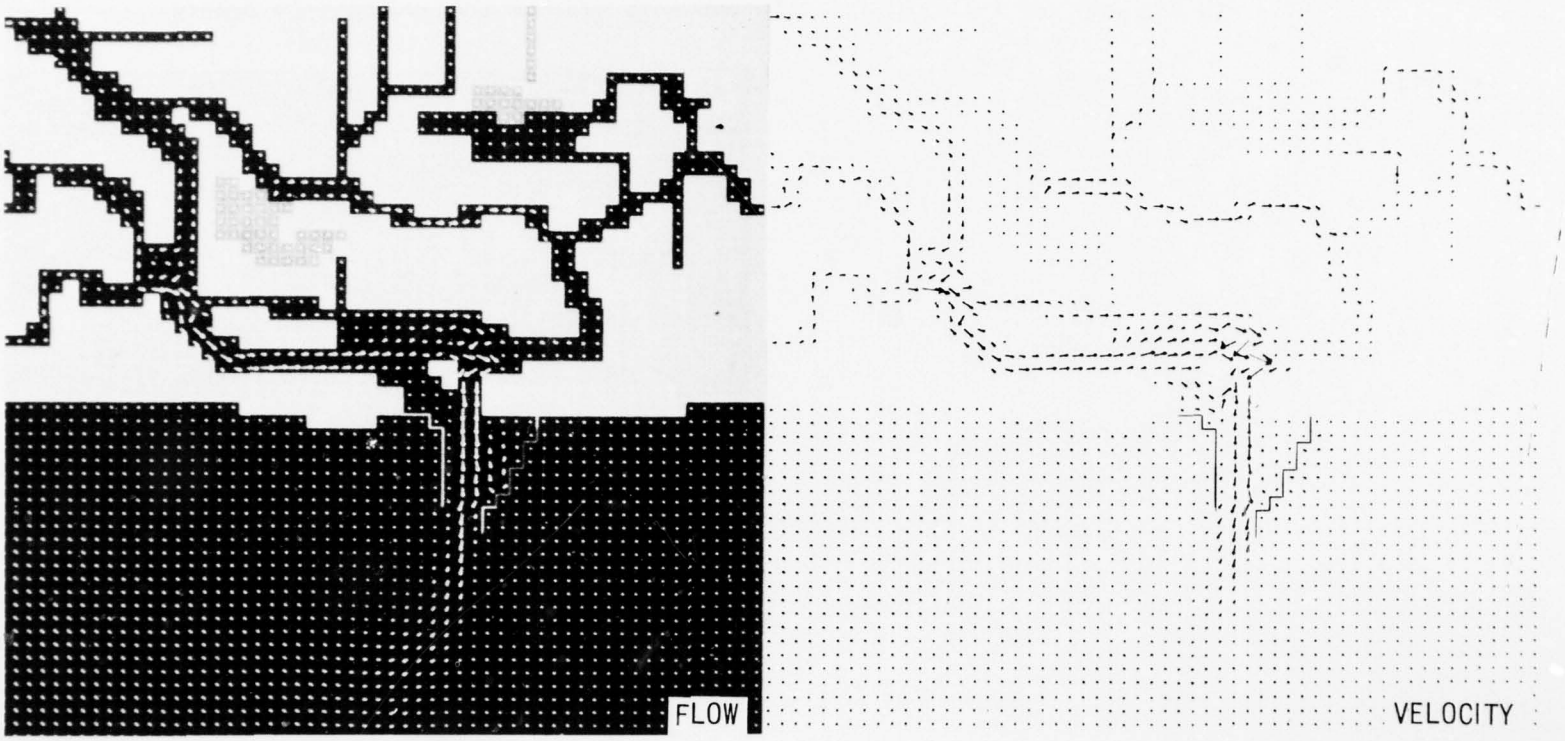

Figure 49. Comparison of unit flow and velocity patterns at 1400 EST for Plan CC

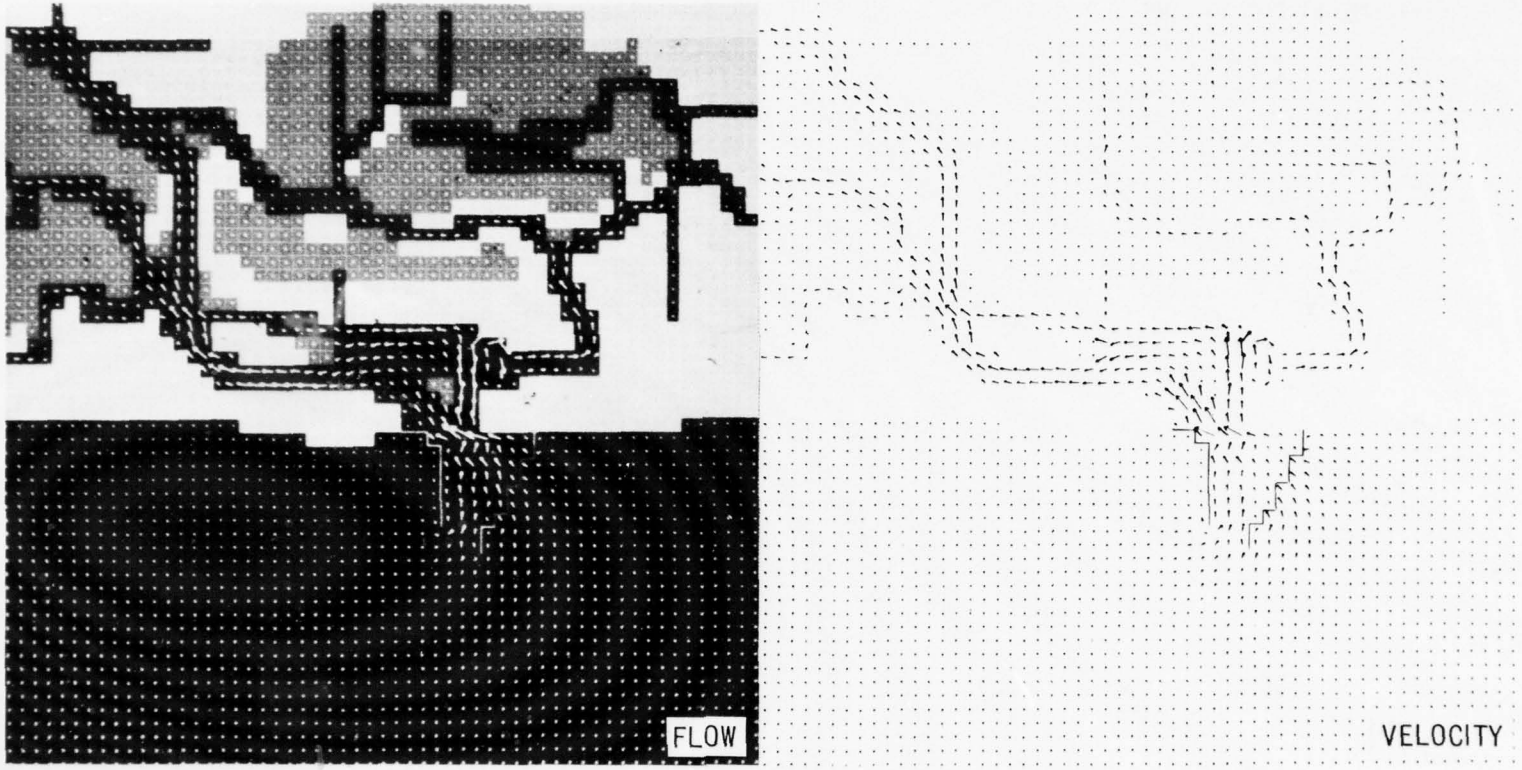

Figure 50. Comparison of unit flow and velocity patterns at 1900 EST for Plan CC

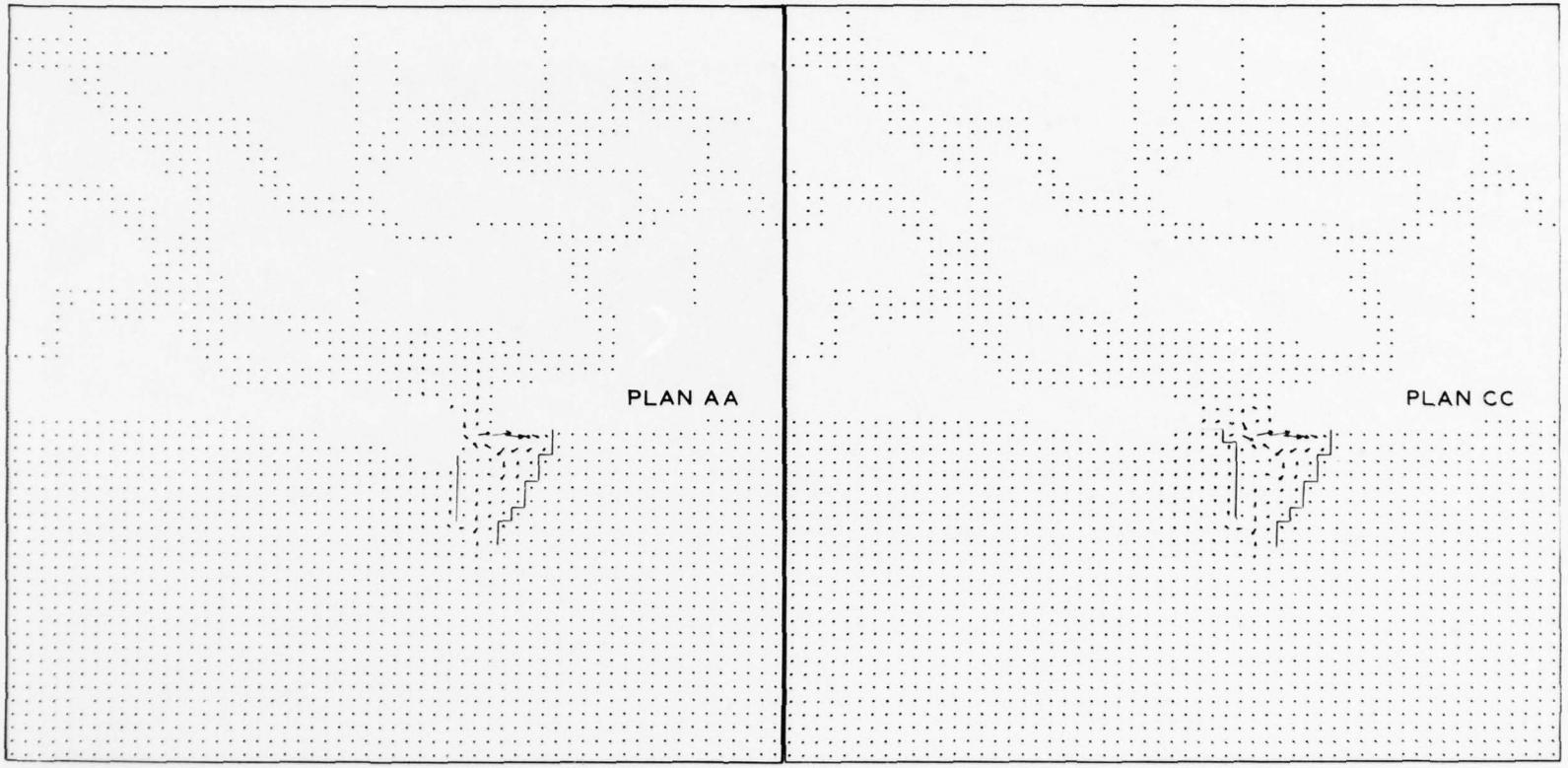

Figure 51. Comparison of unit flow difference patterns for Corson Inlet Plans AA and CC at 0600 EST

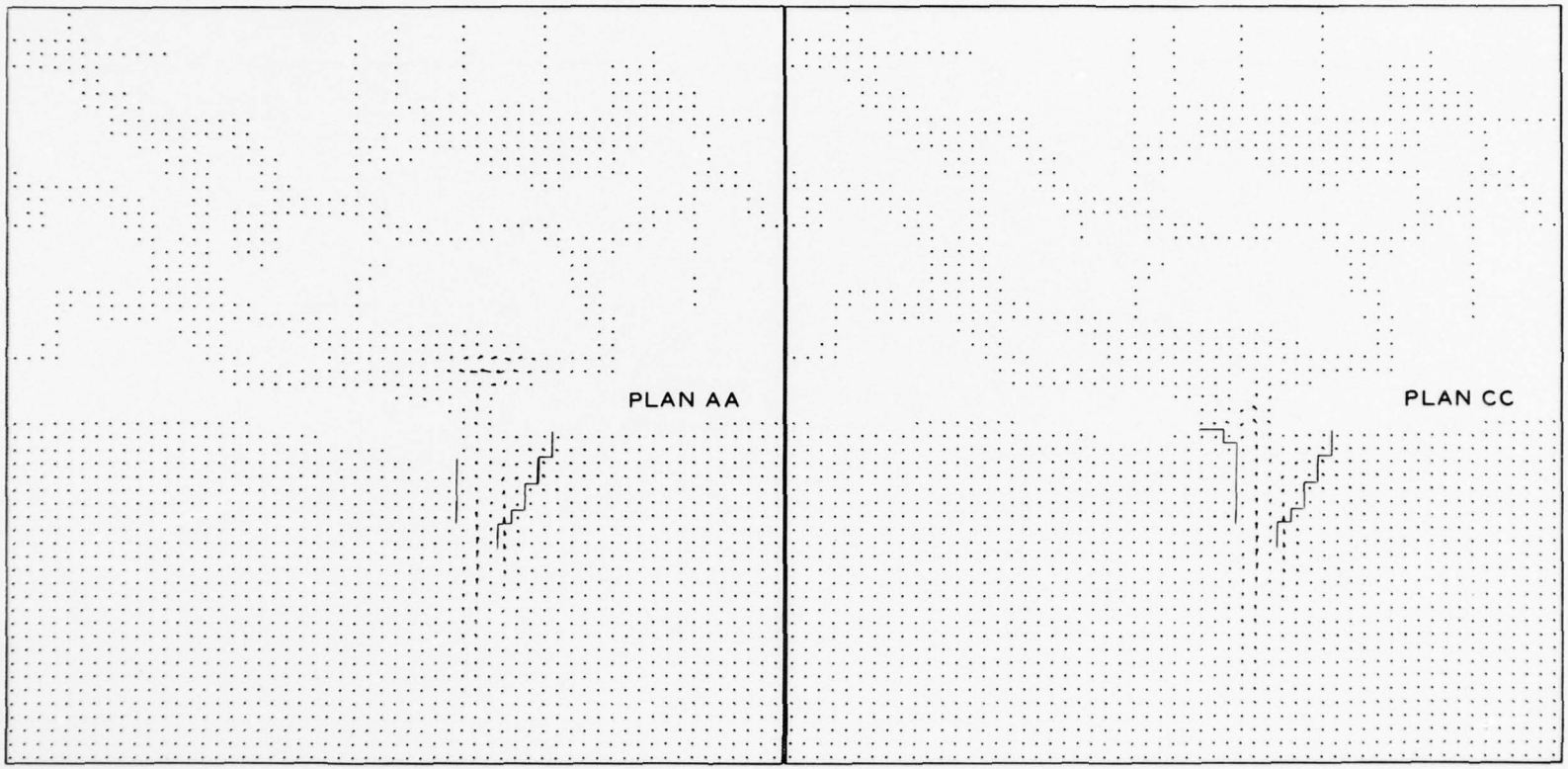

Figure 52. Comparison of unit flow difference patterns for Corson Inlet Plans AA and CC at 1000 EST

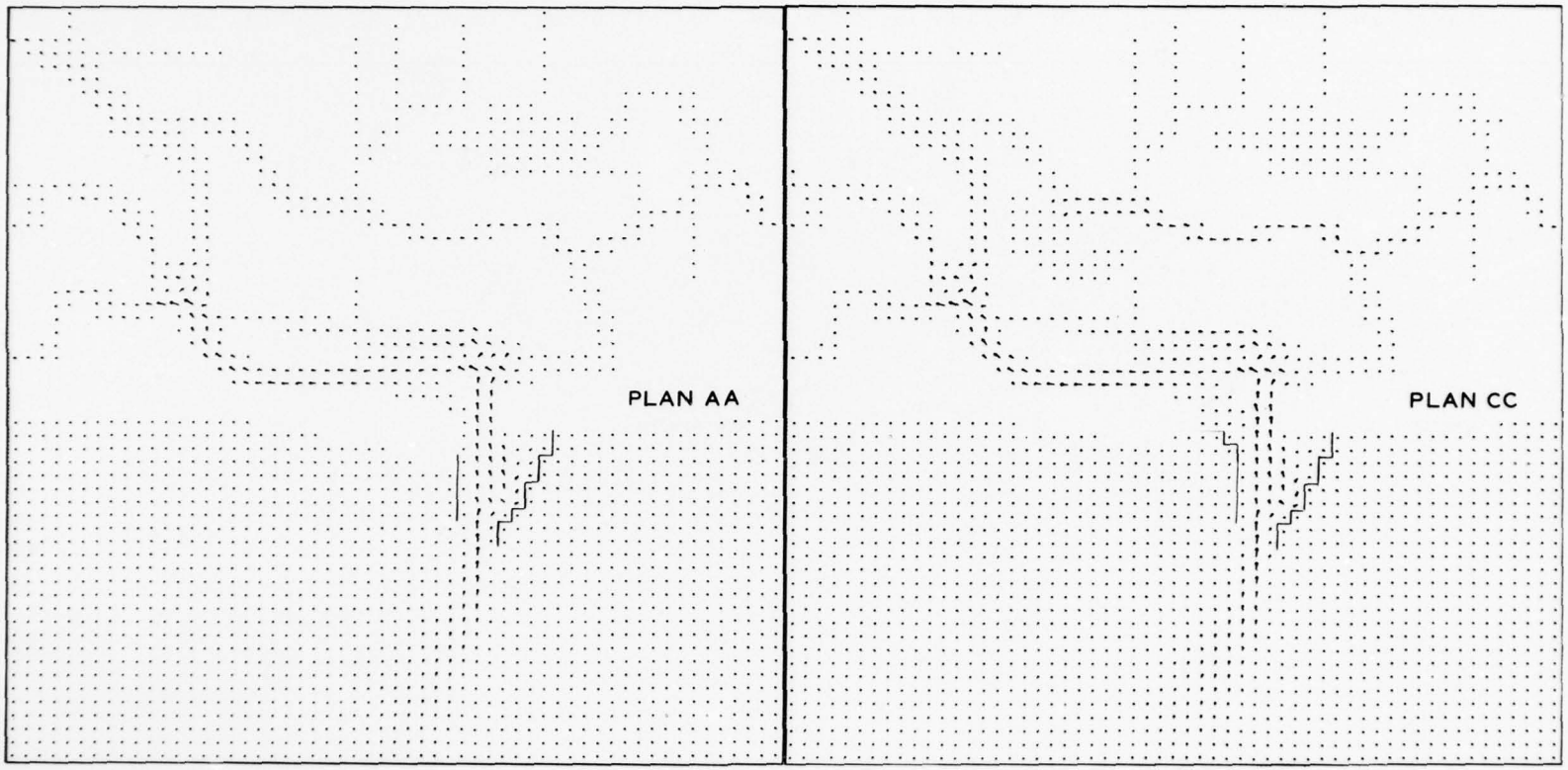

Figure 53. Comparison of unit flow difference patterns for Corson Inlet Plans AA and CC at 1400 EST

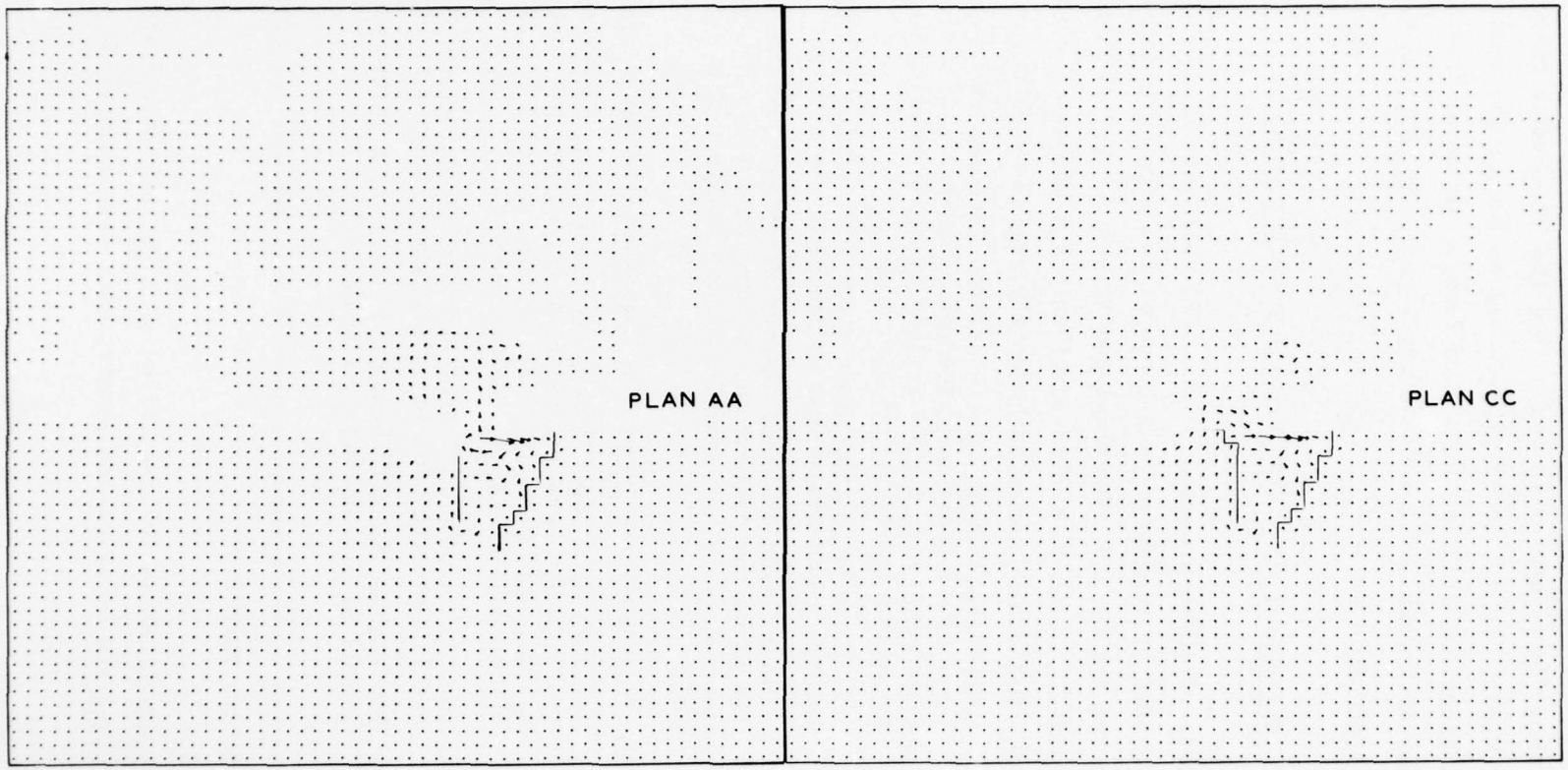

Figure 54. Comparison of unit flow difference patterns for Corson Inlet Plans AA and CC at 1900 EST

(Figure 53) the effects appear to reach into the Strathmere channel as well as into Middle Thoro. These effects may be due to the numerical difficulties experienced during this time frame. The unit flow difference plots for both plans at 1-hour intervals are available in microfiche form in Appendix E.

Improvement Plans for Great Egg Harbor Inlet

62. Tests of three proposed inlet modifications were conducted with the 1974-1975 hydrographic conditions of the Great Egg Harbor Inlet system and the 9 June 1975 tidal conditions. Figure 55 depicts Plans A, B, and B1. Plan B1 consisted of only the upcoast portion of Plans A and B. All plans tested included the following features:

a. A 3000-ft-long weir-jetty system, attached to an existing jetty at Longport and extending seaward in a southerly direction, with a 2200-ft-long low-weir section having a top elevation of 0.0 ft SLD.

b. A 54-acre deposition basin (bottom elevation -27 ft SLD) located immediately west of the low-weir section.

c. A 300-ft-wide entrance channel extending seaward to the -14 ft bottom contour and bayward to Bascule Bridge at Ocean City. The channel is to be maintained at -14 ft SLD.

For the downdrift side of the inlet, the improvement plans included:

a. For Plan A, a 5550-ft-long bulkhead-jetty system extending from the northern end of Ocean City along the inlet frontage for 3450 ft (bulkhead) and then seaward for 2100 ft (1100-ft bulkhead and 1000-ft jetty).

b. For Plan A, the fillet between the jetty and bulkhead was backfilled with sand to an elevation of +6.0 ft SLD.

c. For Plan B, the bulkhead-jetty-fill area system was replaced by a 4200-ft-long dogleg jetty.

Plan B1 consisted of the upcoast structures only and was tested solely for investigatory purposes.

Plan A results

63. Figure 56 shows the comparison of tidal elevations with Plan A installed, using the verification results as a base condition. With

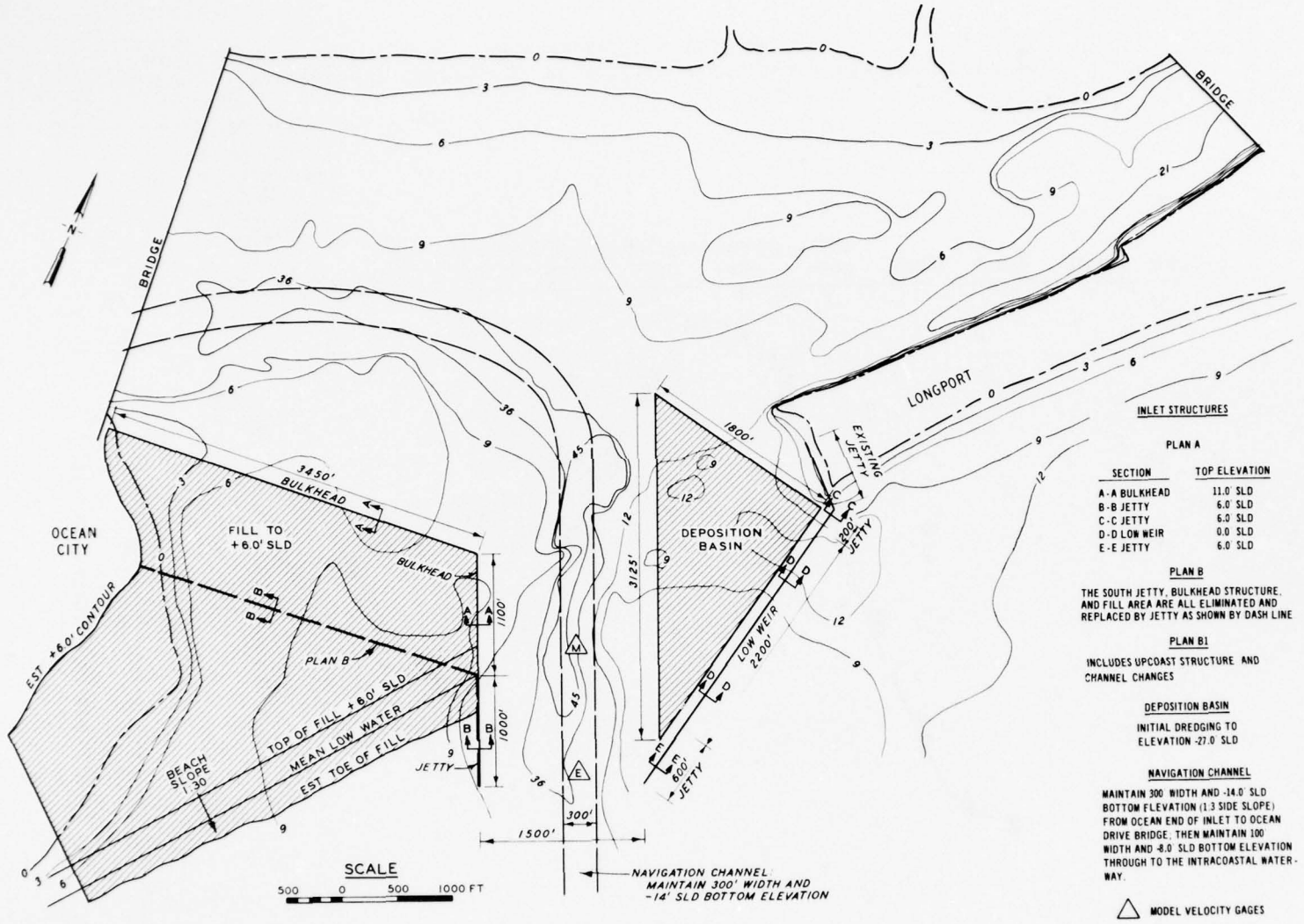

Figure 55. Proposed improvement plans for Great Egg Harbor Inlet

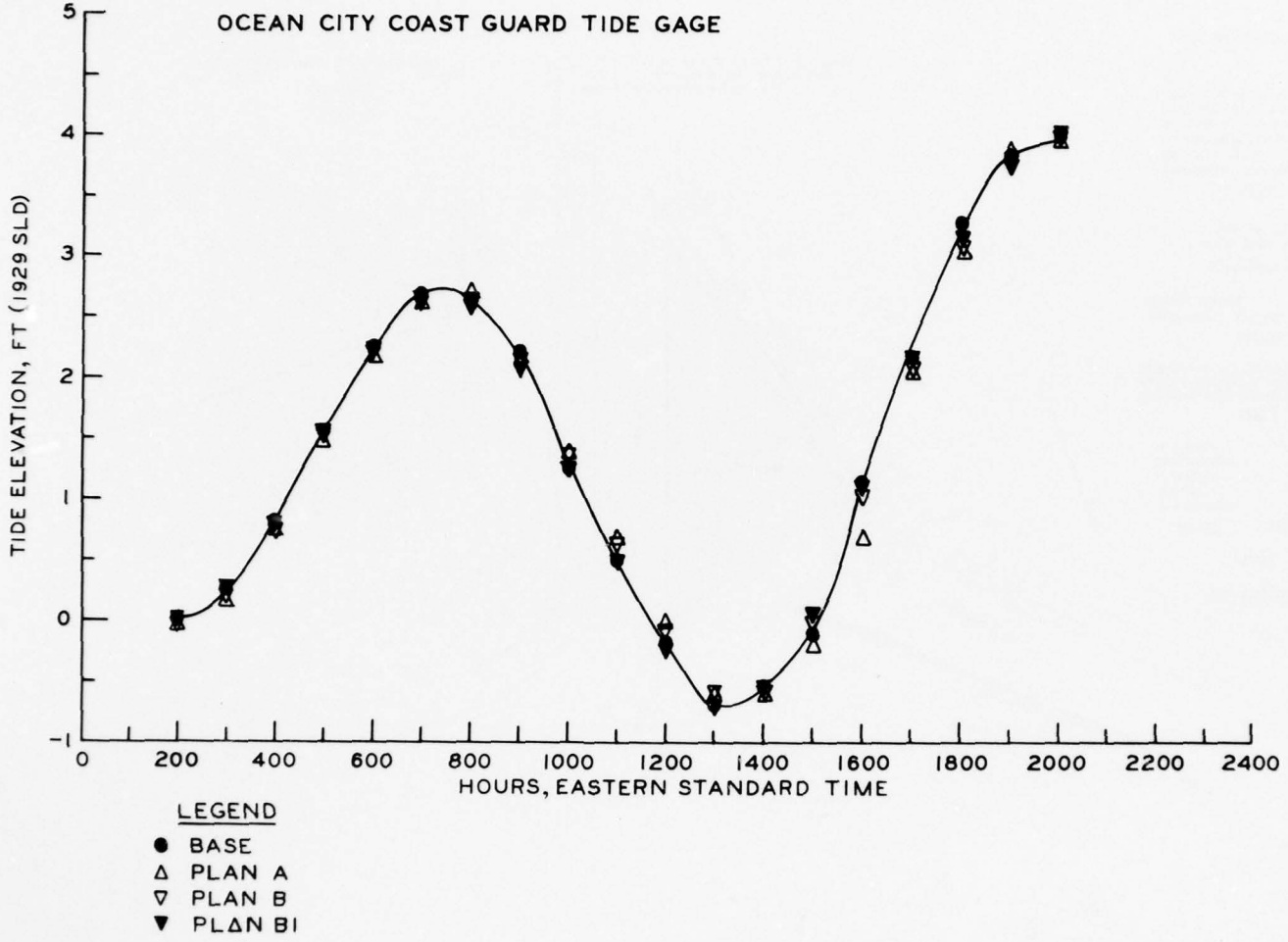

Figure 56. Comparison of surface elevations (plan to base) for the Ocean City tide gage

this plan installed it was noted that tidal elevations were not significantly changed. The plan had a tendency to reduce the tidal elevation during flood stage and to increase it during ebb stage in the vicinity of the inlet throat but the tidal amplitude was unchanged. Mean tide levels for various locations throughout the inlet system are given in Table 4, and it can be seen that the plan caused no significant mean tide level changes.

64. The comparisons between Plan A and the base conditions for current velocities at base gage conditions are given in Figures 57 and 58. The velocities at these locations were changed only slightly. There was a general tendency for maximum ebb and maximum flood velocities to be slightly reduced. The base gages in the throat area are not located in the main channel and thus give little information on the plan effects in this area. Figure 59 depicts the comparison between plan and base conditions for current velocities at a gage located in the entrance channel at the end of the jetty system (gage E in Figure 55). A second gage was located in main channel midway between the inlet throat and the end of the jetty (gage M in Figure 55). Increases in maximum velocity (30 to 70 percent) are noted for both gages during flood and ebb stages with the plan installed.

65. Unit flow patterns for Plan A at the same time in the tidal cycle used for displaying the base results (Figures 32-35) are given in Figures 60-63. The downcoast jetty in the velocity patterns is shown extending from the landfill area. Plan A tended to keep the flow confined to the main channels during most of the tidal cycle. During ebb stage the flow appeared to move toward the deposition basin. Plots such as Figure 62 indicate that the ebb flow might well erode the berm between the channel and the deposition basin. The flood flow over the low-weir section during higher stages of the tide appears substantial and should eliminate any impoundment of sand on the updrift side of the structure by allowing the sand to move into the deposition basin. The downdrift bulkhead and landfill appeared to substantially reduce ebb flow over the shoal area north of the bulkhead. Another feature of the plan was the formation of small eddies at the seaward end of the

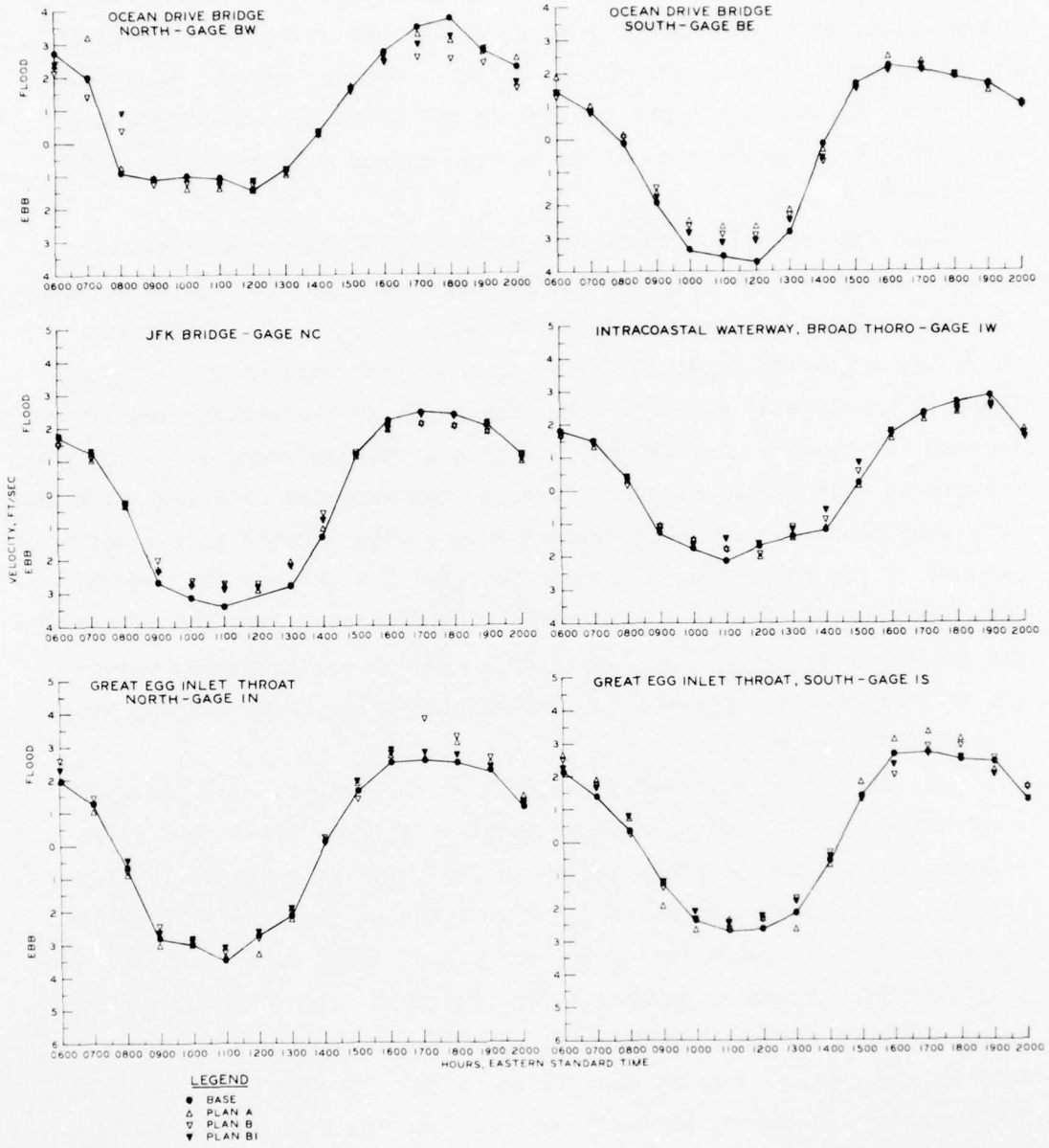

Figure 57. Comparison of current velocities (plan to base) for Great Egg Harbor Inlet base gages

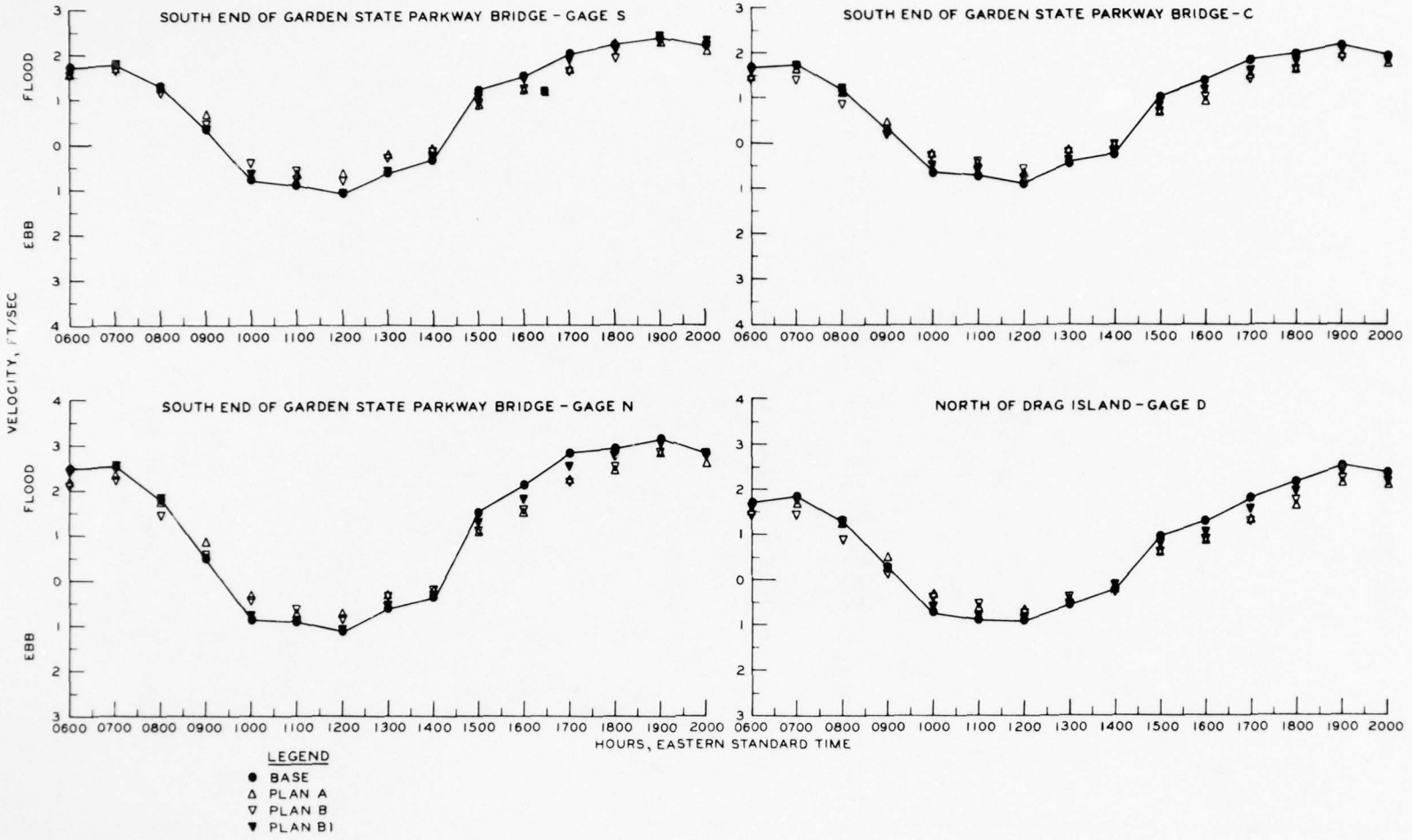

Figure 58. Comparison of current velocities (plan to base) for Great Egg Harbor Inlet base gages

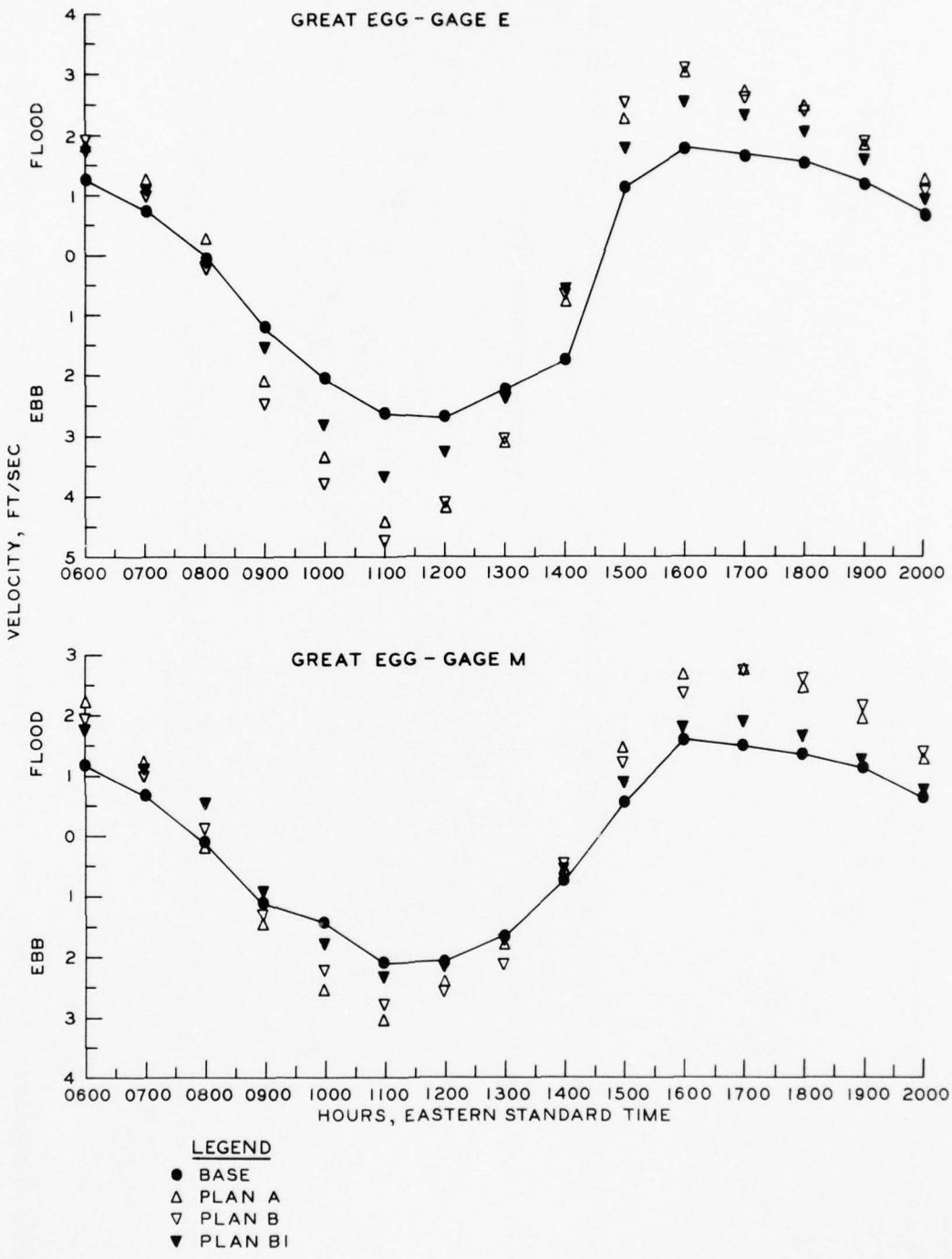

Figure 59. Comparison of current velocities in main channel (plan to base)

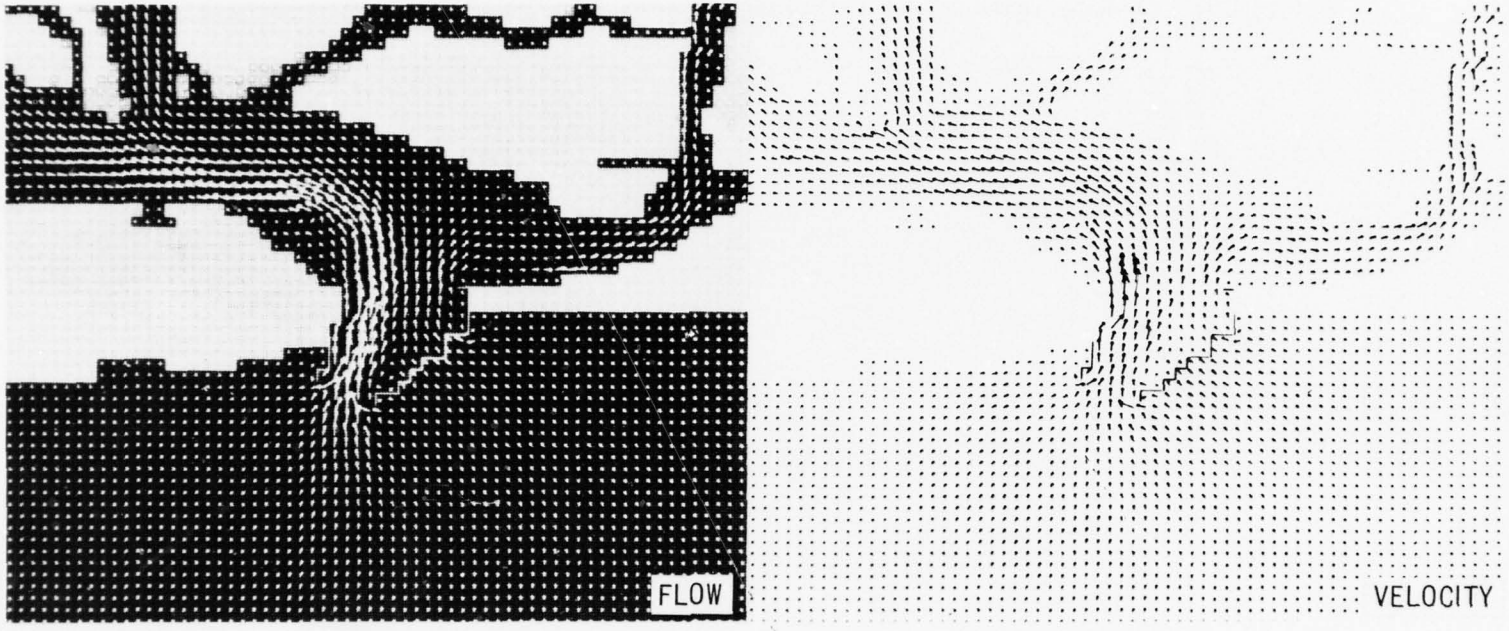

Figure 60. Comparison of unit flow and velocity patterns at 0500 EST for Plan A

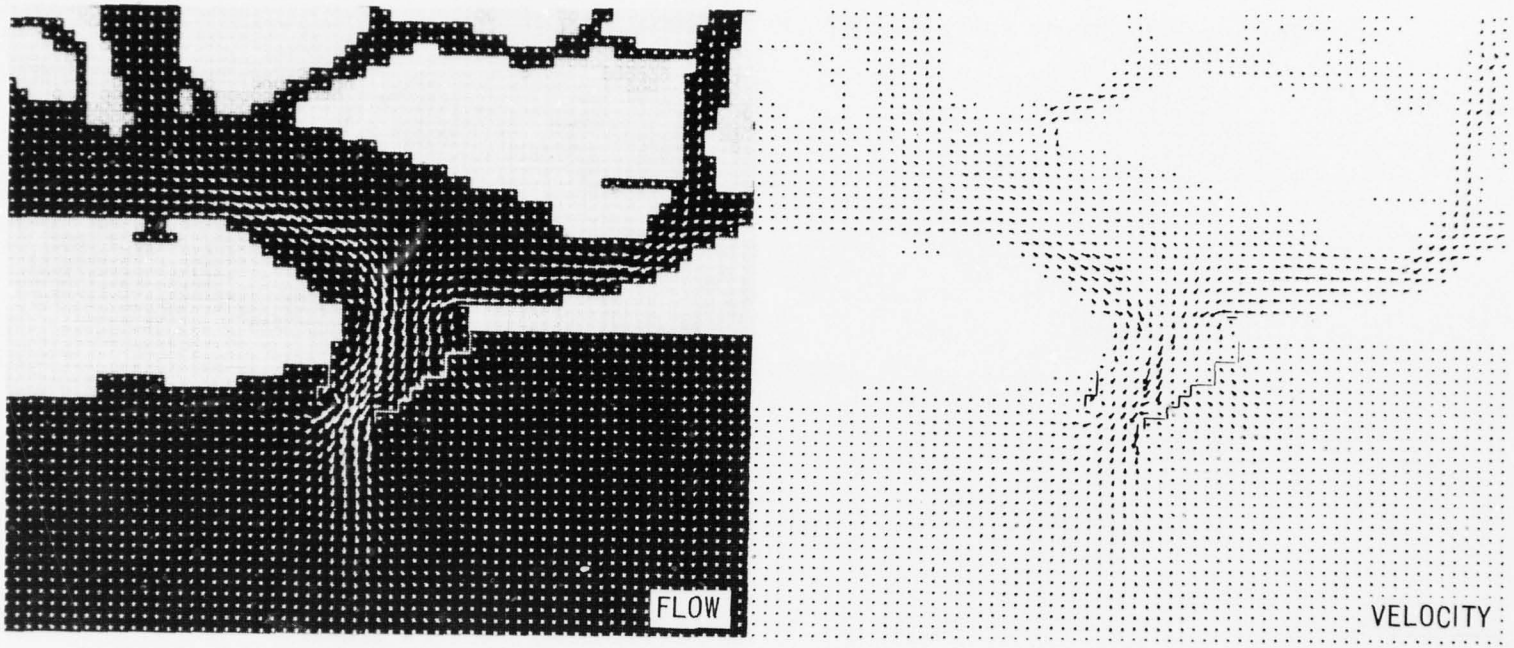

Figure 61. Comparison of unit flow and velocity patterns at 0900 EST for Plan A

AD-A063 080 ARMY ENGINEER WATERWAYS EXPERIMENT STATION VICKSBURG MISS F/G 20/4
NUMERICAL SIMULATION OF TIDAL HYDRODYNAMICS, GREAT EGG HARBOR A--ETC(U)
JUN 78 H L BUTLER

UNCLASSIFIED WES-TR-H-78-11 NL

2 OF 2
AD
A063080

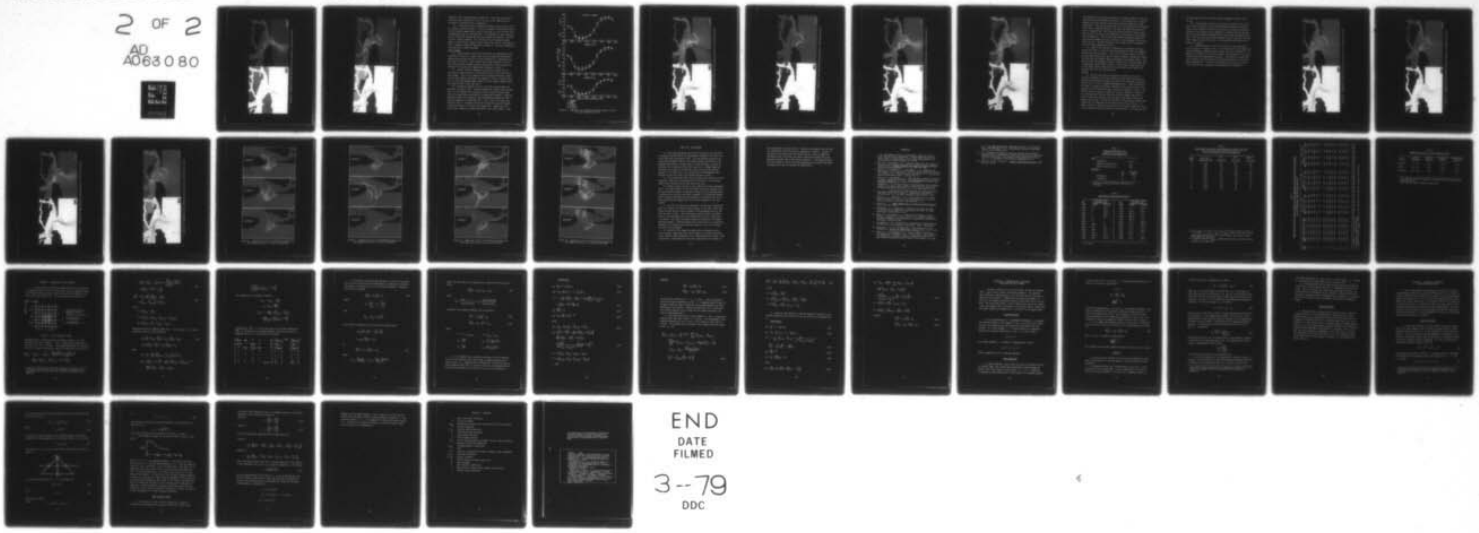

END
DATE
FILMED
3--79
DDC

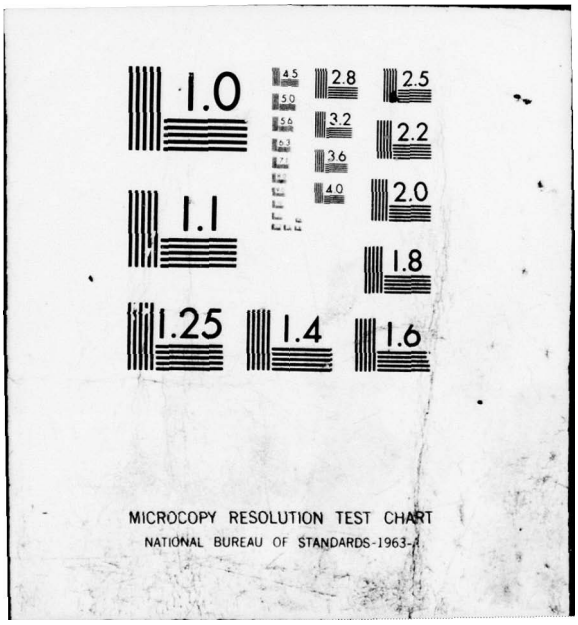
1.0
1.1
1.25
1.4
1.6
1.8
2.0
2.2
2.5
2.8
3.2
3.6
4.0
4.5
5.0
5.6
MICROCOPY RESOLUTION TEST CHART
NATIONAL BUREAU OF STANDARDS-1963-A

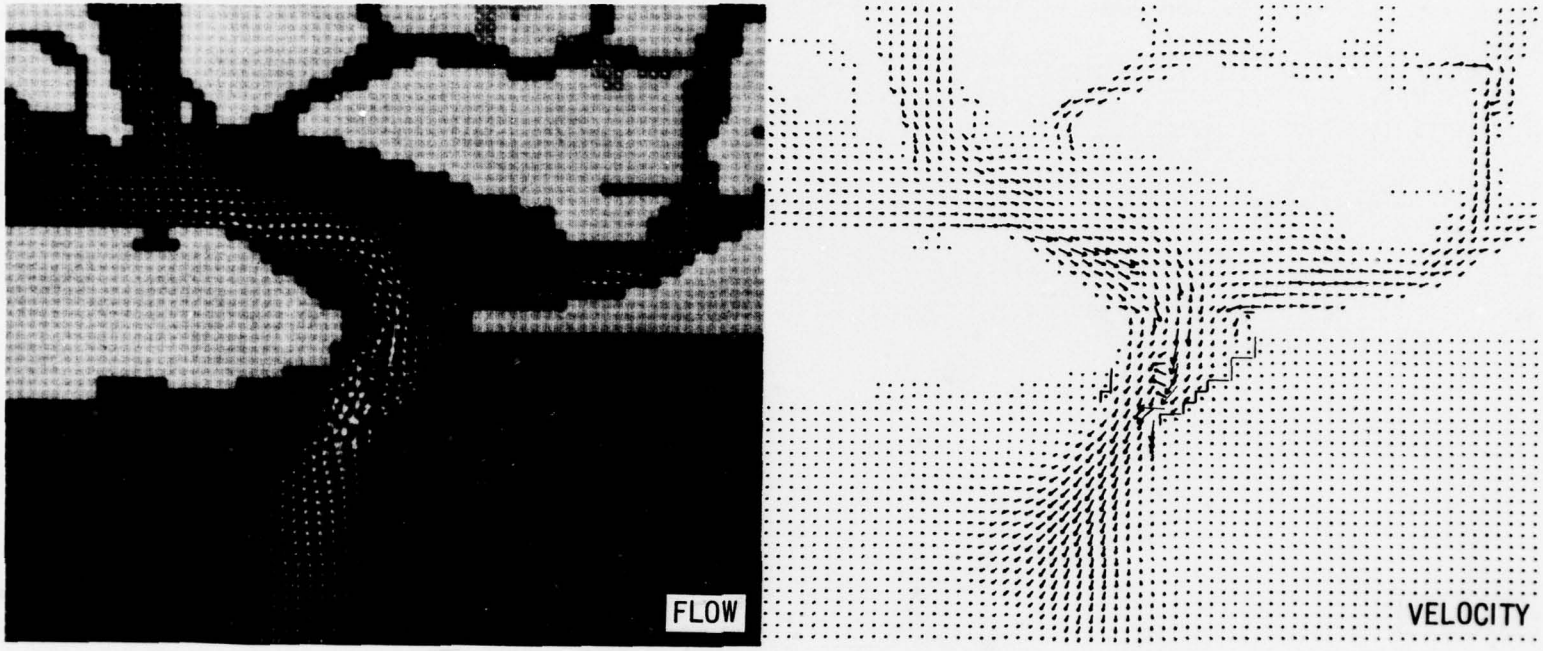

Figure 62. Comparison of unit flow and velocity patterns at 1100 EST for Plan A

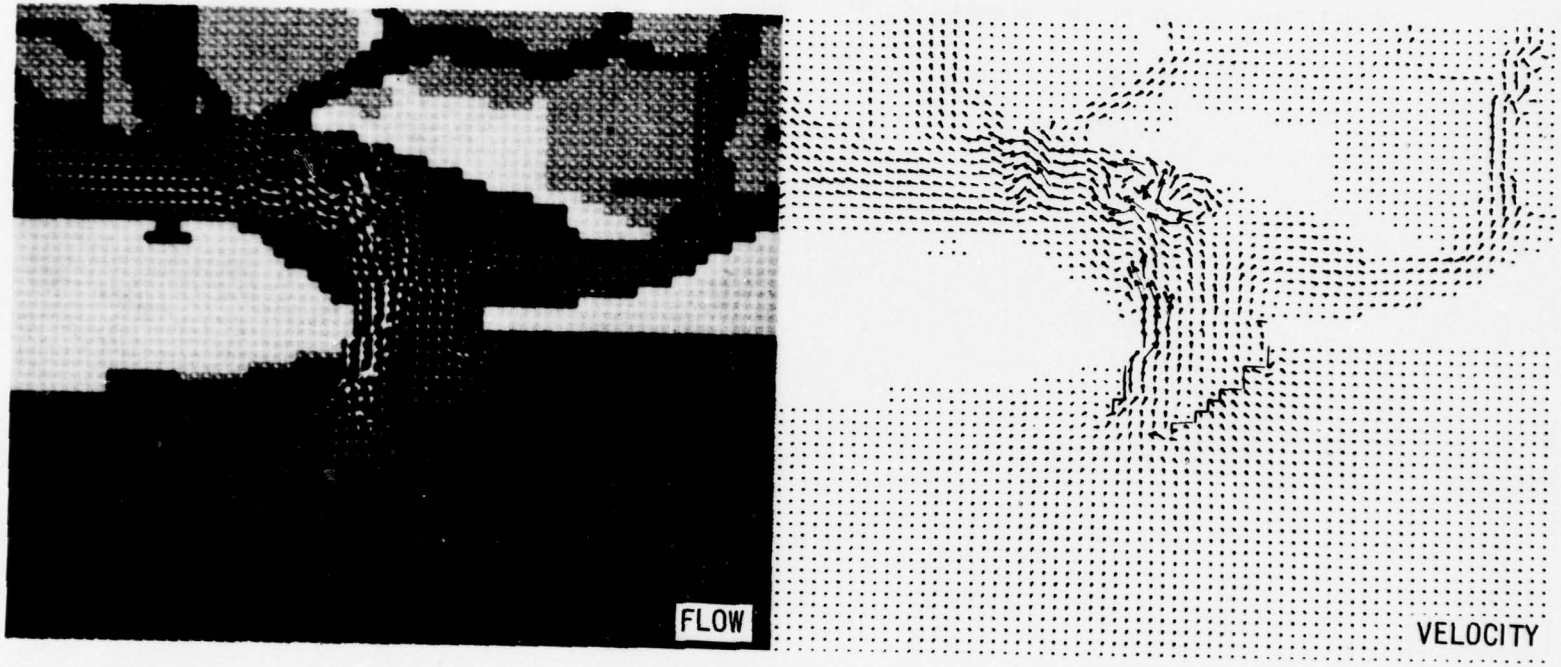

Figure 63. Comparison of unit flow and velocity patterns at 1900 EST for Plan A

downcoast jetty during ebb stage (Figure 61). Both flow and velocity plots for Plan A conditions at ever 1/2 hour of the computation are available in microfiche form in Appendix E.

66. A tabulation of net volumetric discharge across various velocity ranges is given in Table 4. As for the similar verification results, the calculations summarized in Table 4 were made for a 12-1/2-hour cycle extending from 0700 to 1930 hours EST. By narrowing the inlet entrance, the net flood flow through the inlet was reduced by 9 percent. The ebb flow was likewise reduced. Time histories of the discharge through range 1 (inlet throat), ranges 8 and 9 (Ocean City reach), and ranges 10 and 11 (Longport reach) are depicted in Figure 64. The plots demonstrate the reduction in volume discharge.

Plan B results

67. Tidal elevations with Plan B installed are compared with base conditions in Figure 56. Again there were no significant differences between plan and base results with the exception of a slight phase lag with Plan B installed. Plan B showed less change than Plan A at the Ocean City gage but somewhat greater differences at other locations as reflected in the mean tide computations tabulated in Table 4.

68. Current velocity comparisons are given in Figures 57-59. Plan B gives similar results to those noted for Plan A for the verification gages. This can be expected since the major differences should occur in the landfill area which was removed in Plan B. Current velocities at the main channel gages (Figure 59) were slightly higher during ebb stage for Plan B than for Plan A.

69. Circulation patterns for Plan B at four selected times are displayed in Figures 65-68. The major difference between this plan and Plan A is the tendency for substantial flow to seek the shorter path across the large shoal area north of the downcoast bulkhead. Figure 65 indicates weaker flow streamline than corresponding figures for Plan A and base conditions at 0900 hours EST. This is due to the phase lag noted for Plan B. The marsh area north of Ocean City was not flooded at 1900 EST because of the phase lag (Figure 68). During the first flood stage a numerical problem developed in this shoal region. Since

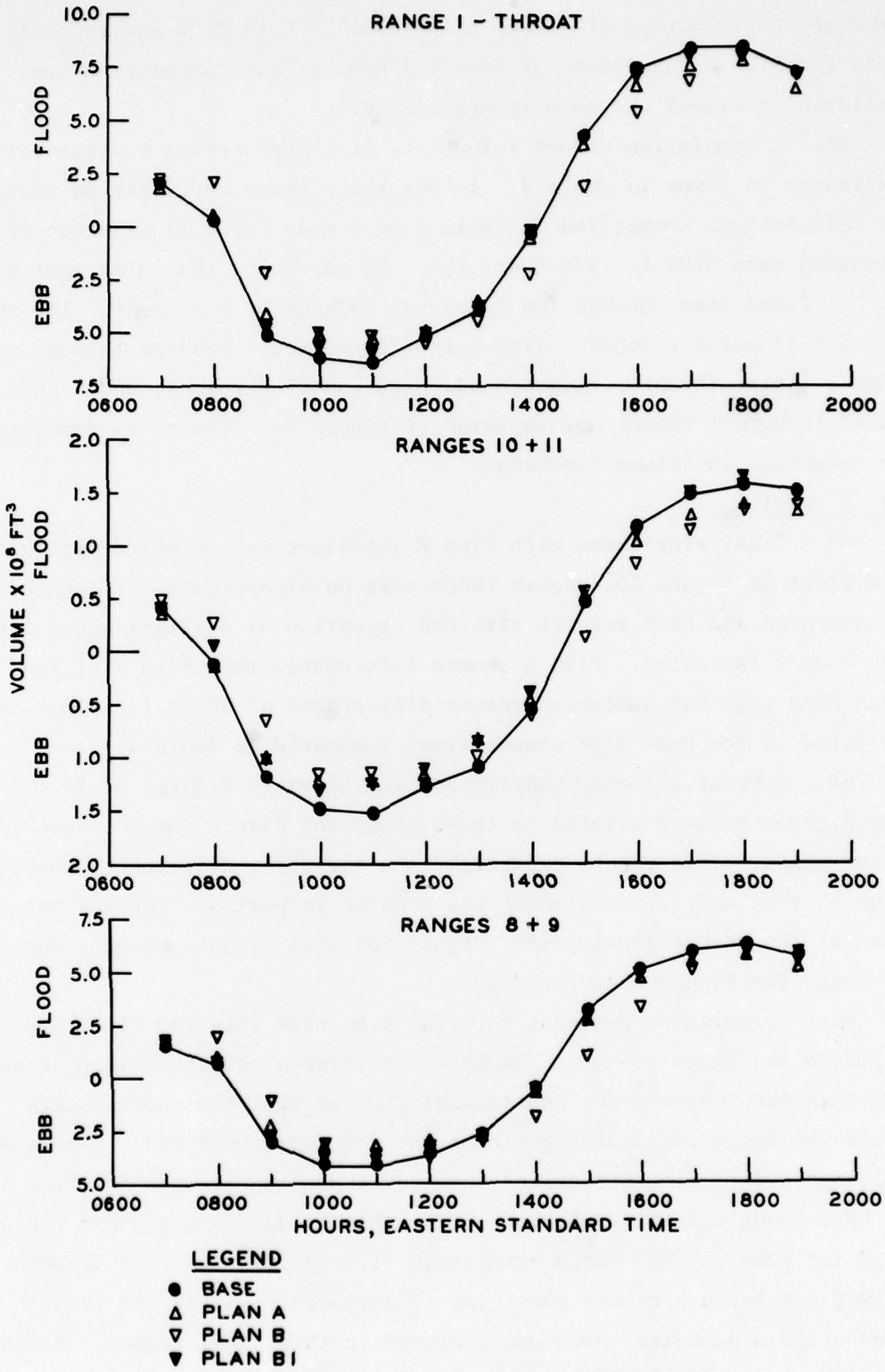

Figure 64. Comparison of volumetric discharges (plan to base) for Great Egg Harbor Inlet

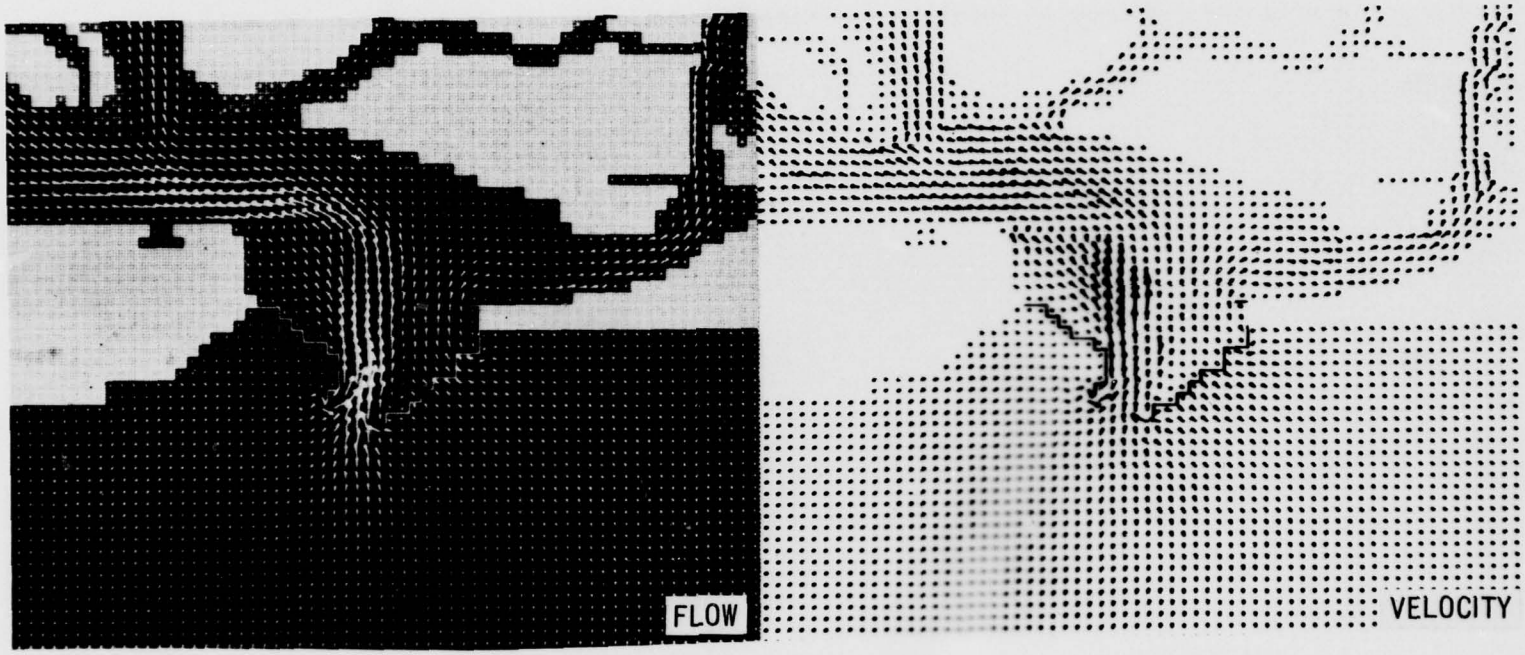

Figure 65. Comparison of unit flow and velocity patterns at 0500 EST for Plan B

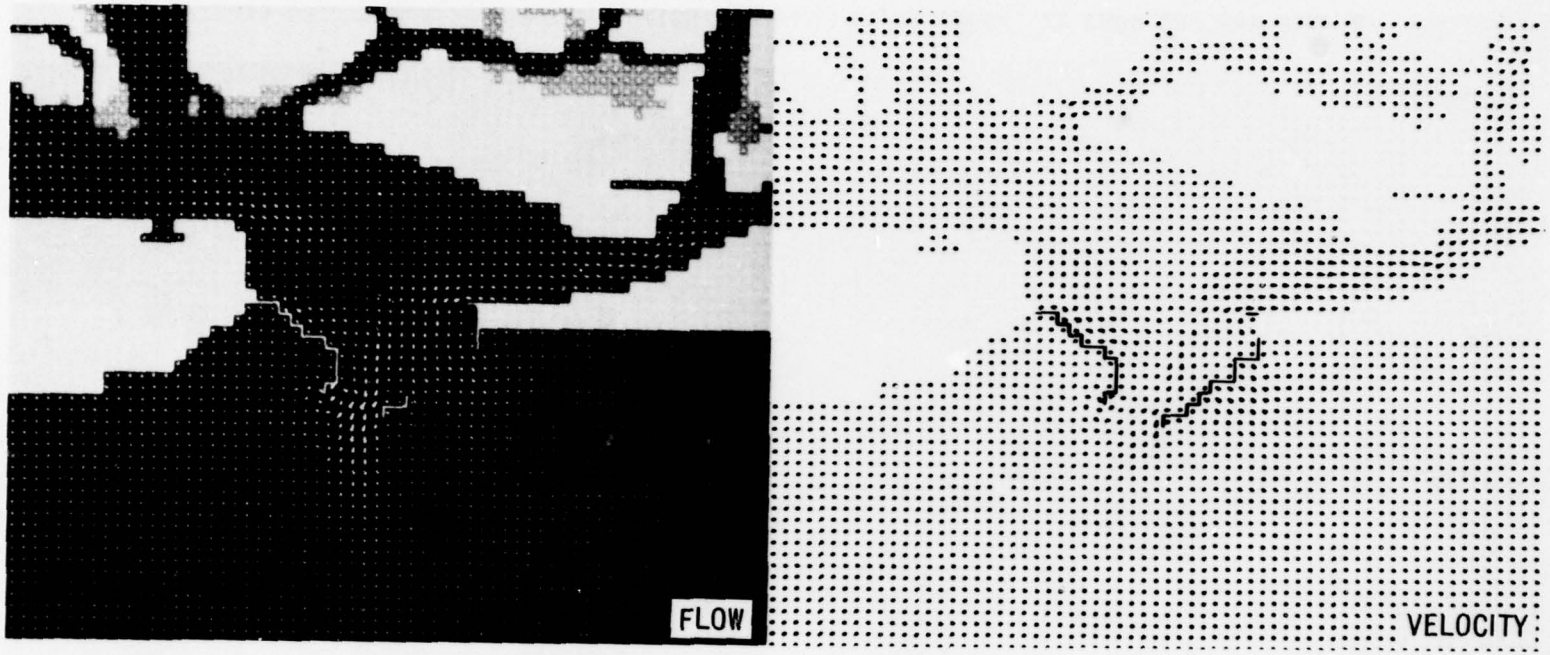

Figure 66. Comparison of unit flow and velocity patterns at 0900 EST for Plan B

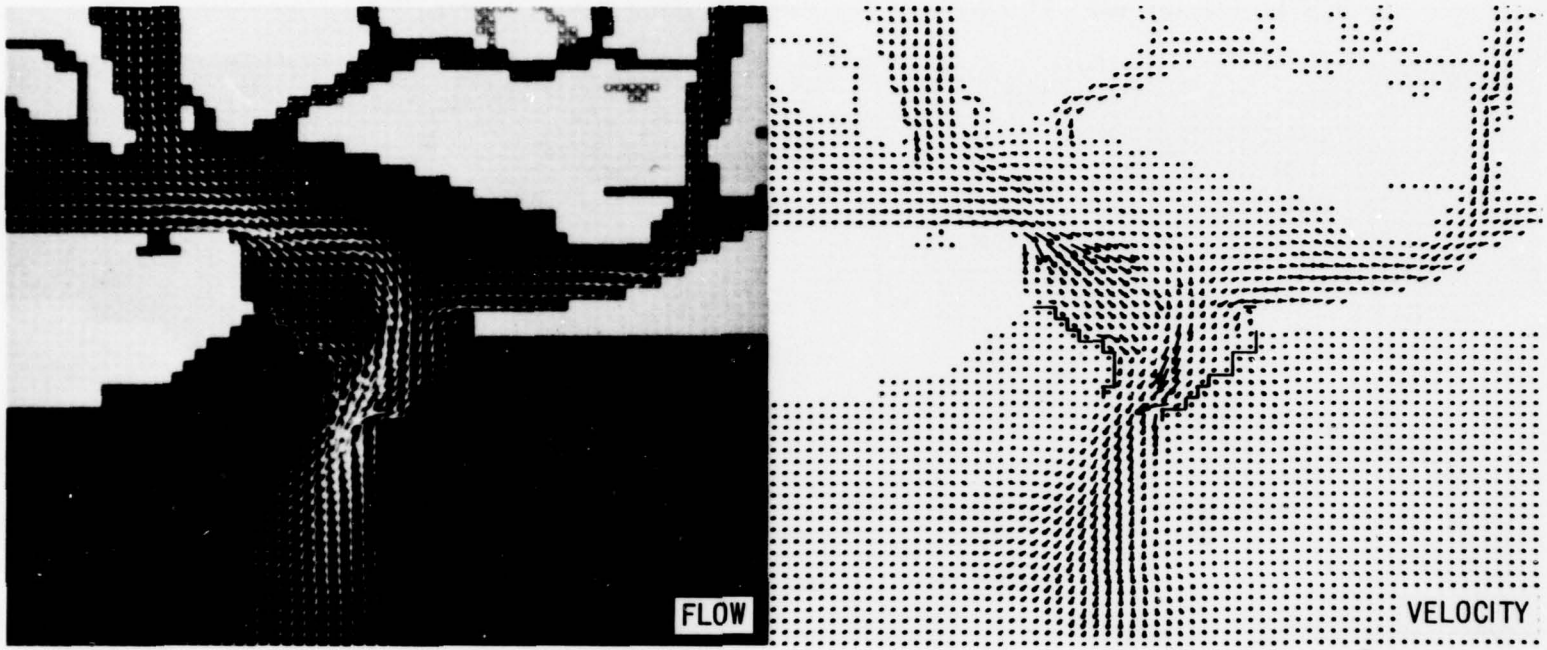

Figure 67. Comparison of unit flow and velocity patterns at 1100 EST for Plan B

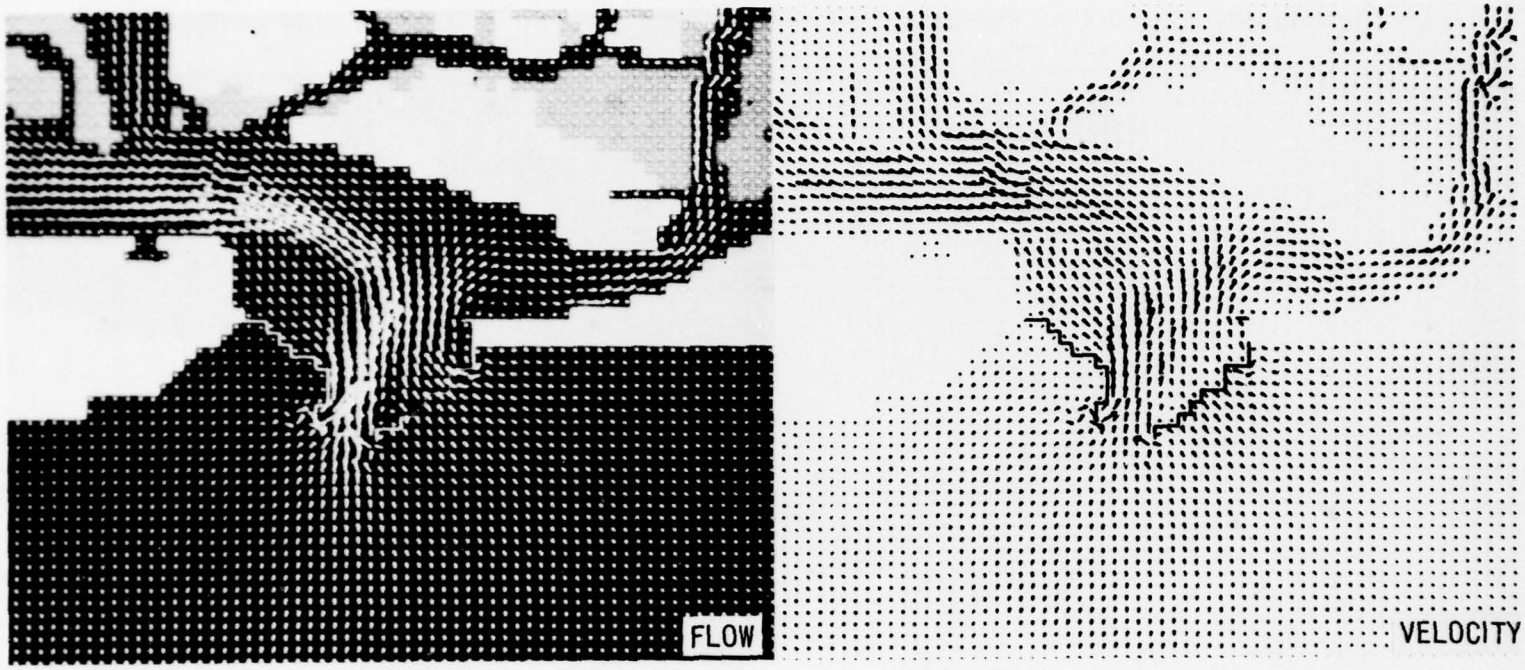

Figure 68. Comparison of unit flow and velocity patterns at 1900 EST for Plan B

the simulation for each plan consisted of a multiple number of runs and successive runs used restart data saved in the previous run, a special damping filter was applied in the shoal area only during the second flood stage. Thus, the flow patterns for Plan B during hours 16 through 18 EST show a smoother pattern in the shoal area than that noted for hours 6 through 8 EST. Both flow and velocity plots for Plan B conditions at every 1/2 hour of the computation are available in microfiche form in Appendix E. The ebb flow was directed toward the deposition basin and the comments on Plan A relative to this problem are valid for Plan B as well. The eddy forming at the seaward end of the downcoast jetty was more prominent for Plan B.

70. Table 4 also includes a tabulation of volumetric discharge results for Plan B. The net flood flow through the inlet was slightly greater than that for Plan A. Plan B had a greater effect than Plan A in altering the mean tide level at various locations through the system. The mean tide was slightly reduced throughout the backbay system. Time history plots of discharge are given in Figure 64 for those ranges used in presenting similar Plan A results. These results demonstrate that a small phase lag was experienced for Plan B which could explain why the mean tide for this plan was lower.

Plan B1

71. Plan B1 consisted of the upcoast structures only and was tested to determine if the flow observed in other plans toward the deposition basin during ebb stage was caused by the downcoast structures. Plan B1 per se is not a proposed improvement plan. Tidal elevations at the Ocean City gage are plotted in Figure 56 and current velocity comparisons at the verification gages are given in Figures 57 and 58. The results are very similar to those for the base conditions. What this test indicated was that the tidal and velocity changes observed for Plans A and B were caused by the two-jetty system rather than by the upcoast jetty alone. The velocity increase in the entrance channel area (Figure 59) was significantly less than that for Plans A and B. As shown in Table 4, the mean tide levels for Plan B1 were generally closer to base conditions than were those for Plans A and B. The same was true

for discharges across the various ranges throughout the model (Figure 64).

72. Flow patterns for Plan B1 are given in Figures 69-72 for the same times in the tidal cycle used for displaying results from other plans. These figures, as well as the full set of circulation patterns available in microfiche form in Appendix E, indicate that the natural path of the main channel funneled the ebb flow toward the upcoast structure. This was also obvious from inspection of base condition flow patterns (Figures 33 and 34) relative to corresponding flow patterns for Plans A, B, and B1.

73. Difference plots of unit flow vectors for the three plans tested are given in Figures 73-76. As for Corson Inlet, the differences were determined by subtracting plan results from base calculations. In general, the effects of all plans are noted to be confined to the localized area near the improvement structures. The effects do extend relatively farther into the back bay area than those noted for the Corson Inlet modifications. The unit flow difference plots for all plans at 1-hour intervals are available in microfiche form in Appendix E.

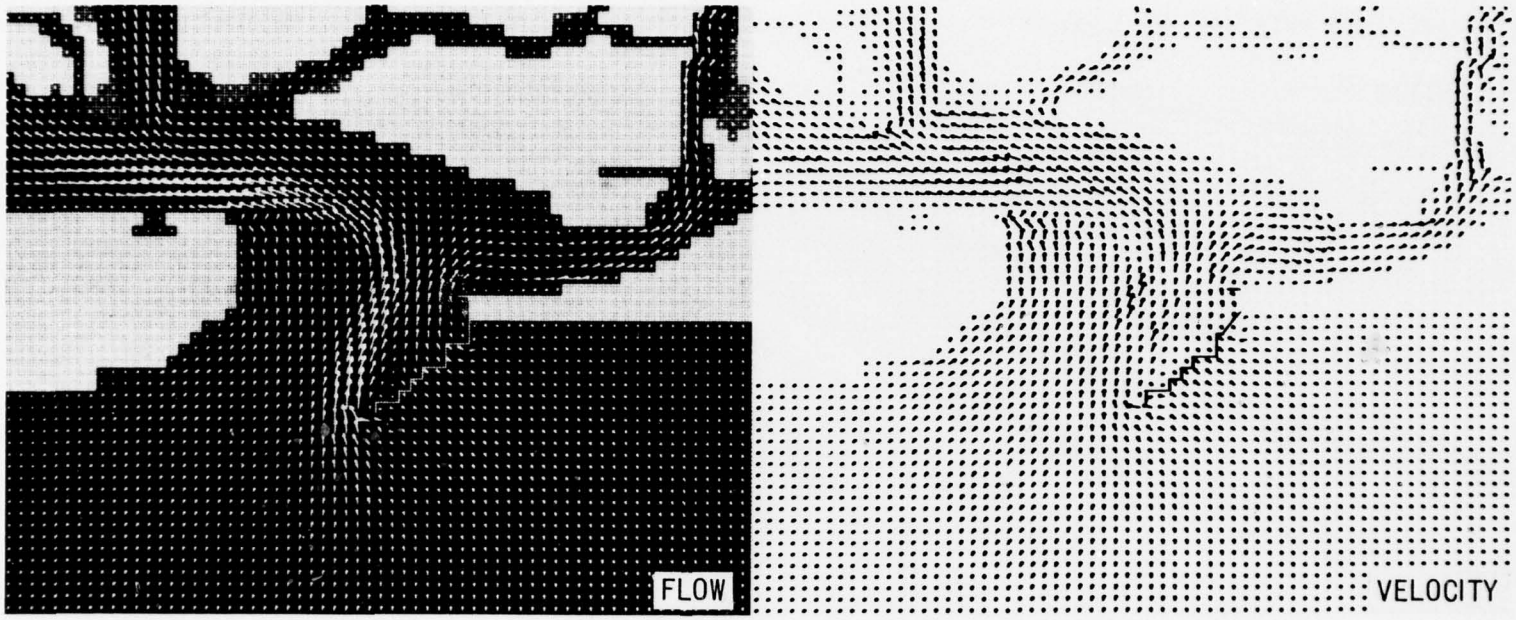

Figure 69. Comparison of unit flow and velocity patterns at 0500 EST for Plan B1

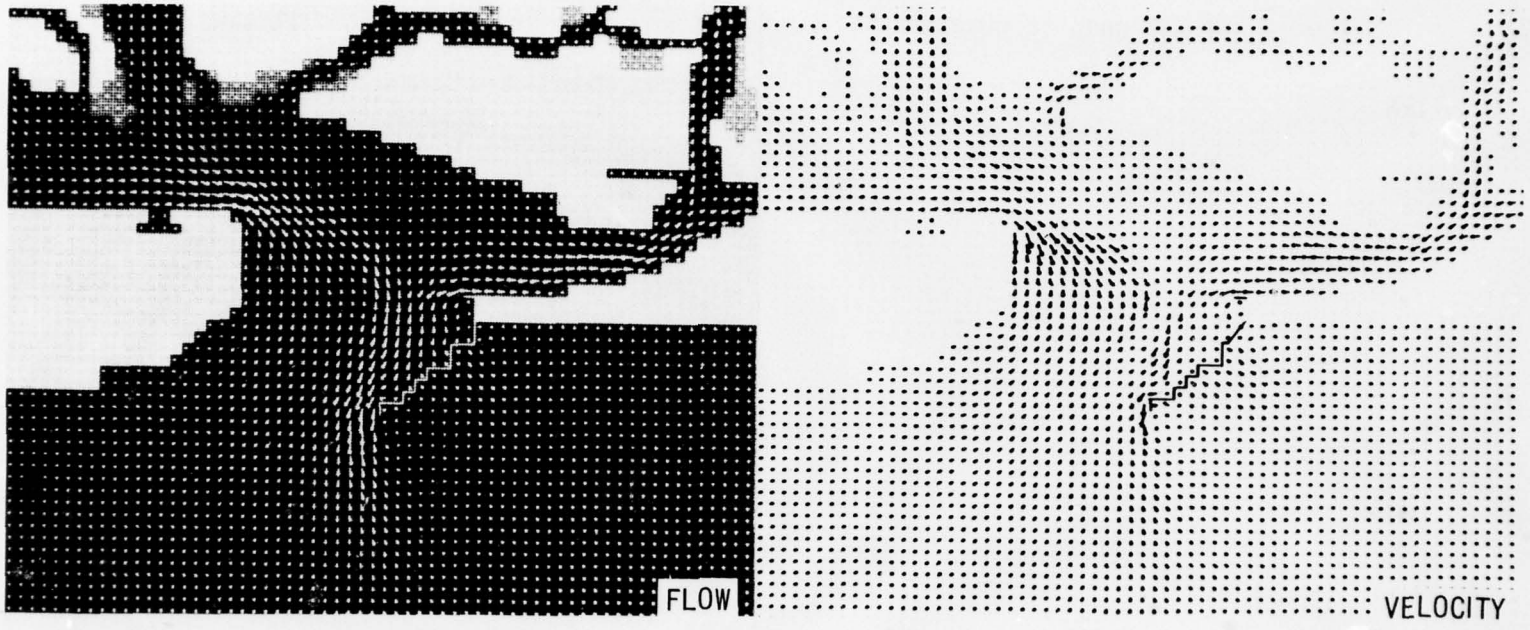

Figure 70. Comparison of unit flow and velocity patterns at 0900 EST for Plan B1

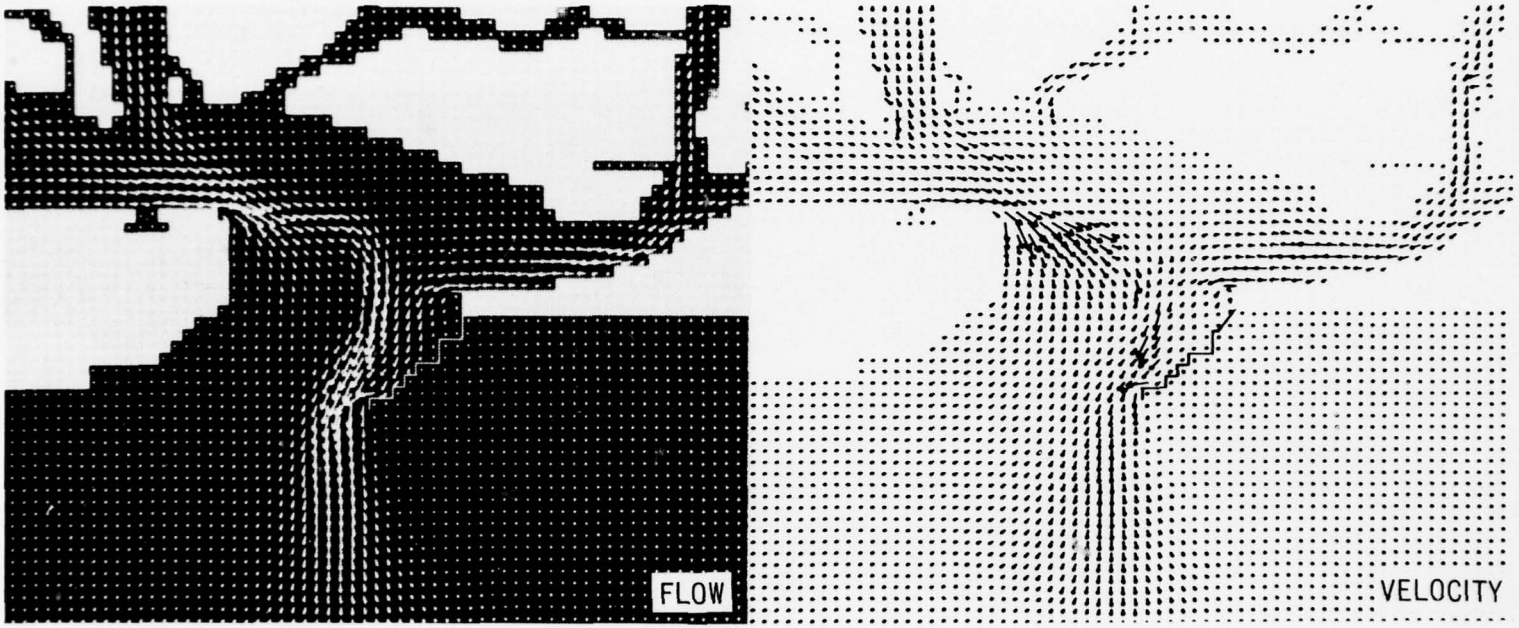

Figure 71. Comparison of unit flow and velocity patterns at 1100 EST for Plan B1

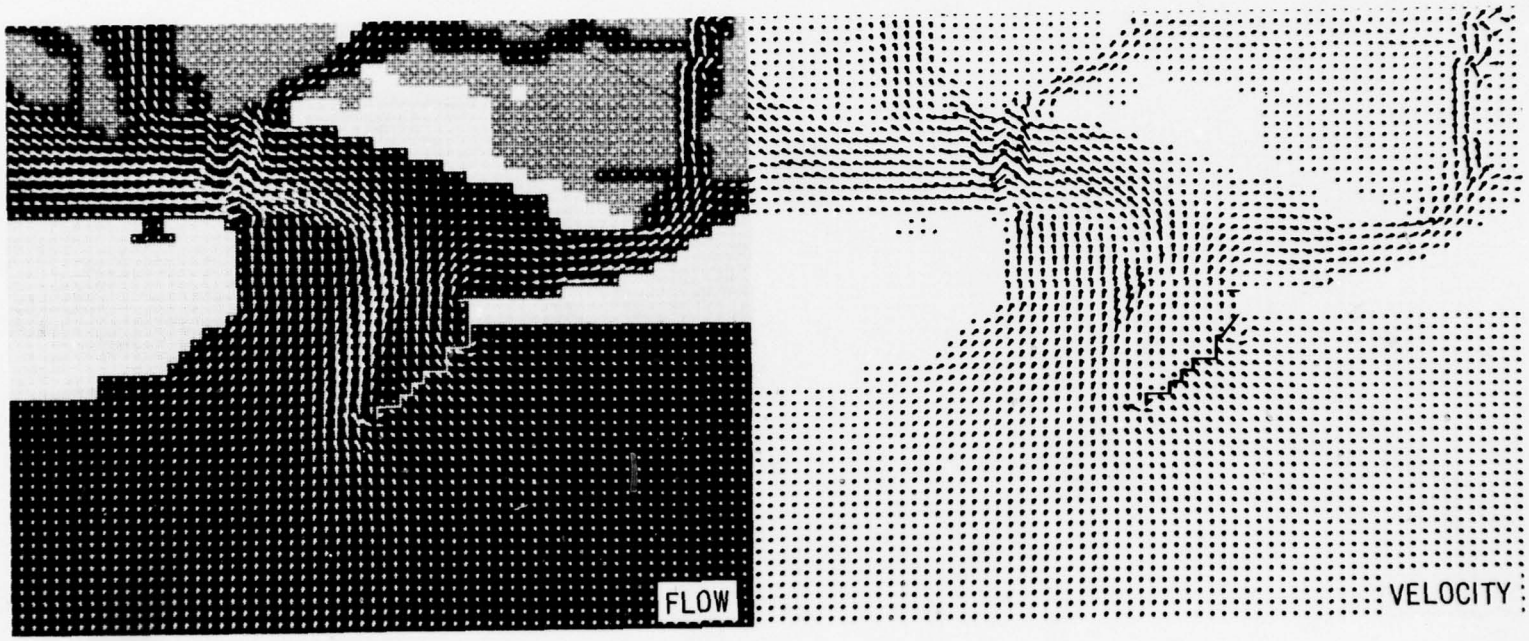

Figure 72. Comparison of unit flow and velocity patterns at 1900 EST for Plan B1

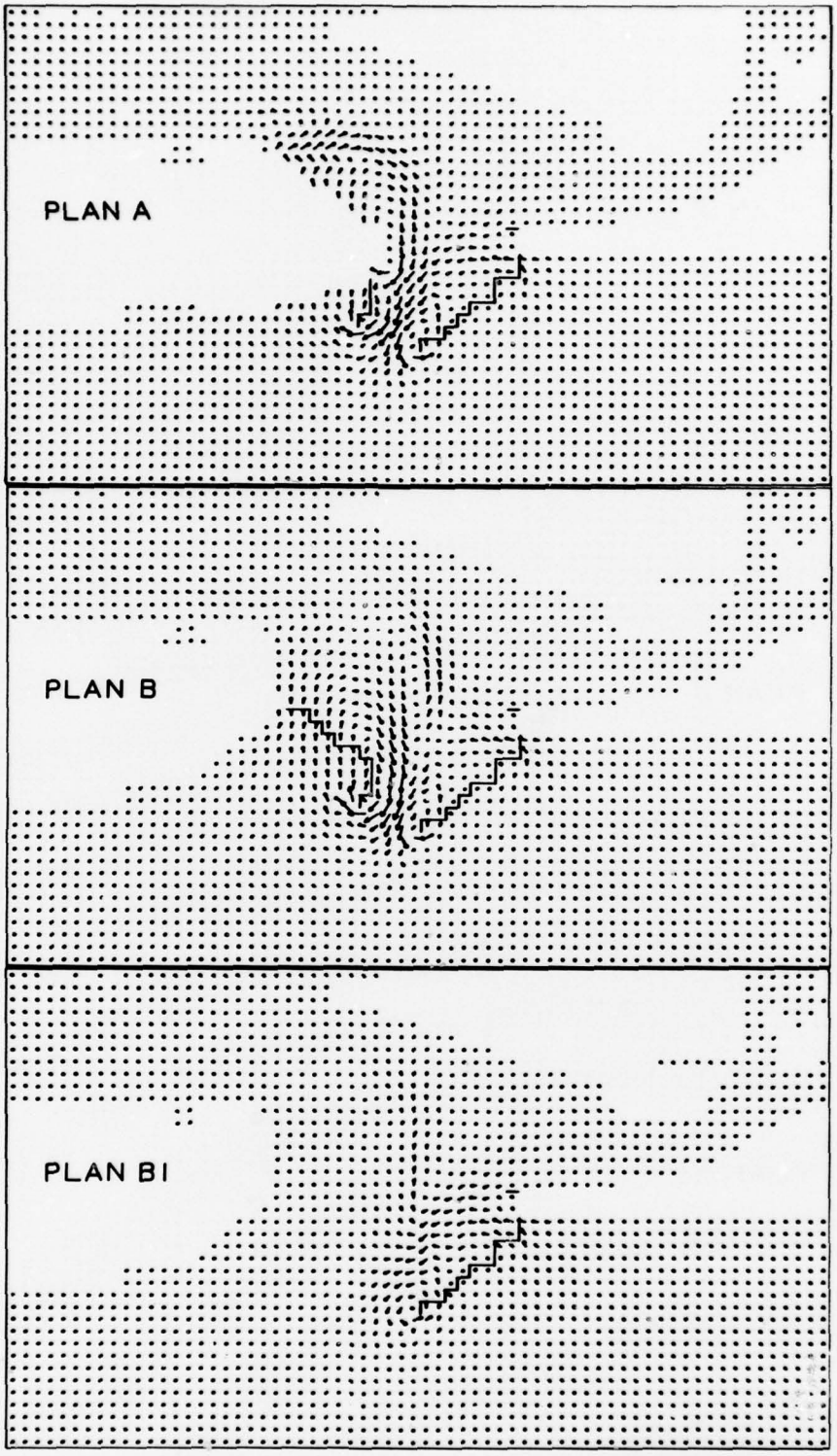

Figure 73. Comparison of unit flow difference patterns for Great Egg Inlet Plans A, B, and B1 at 0500 EST

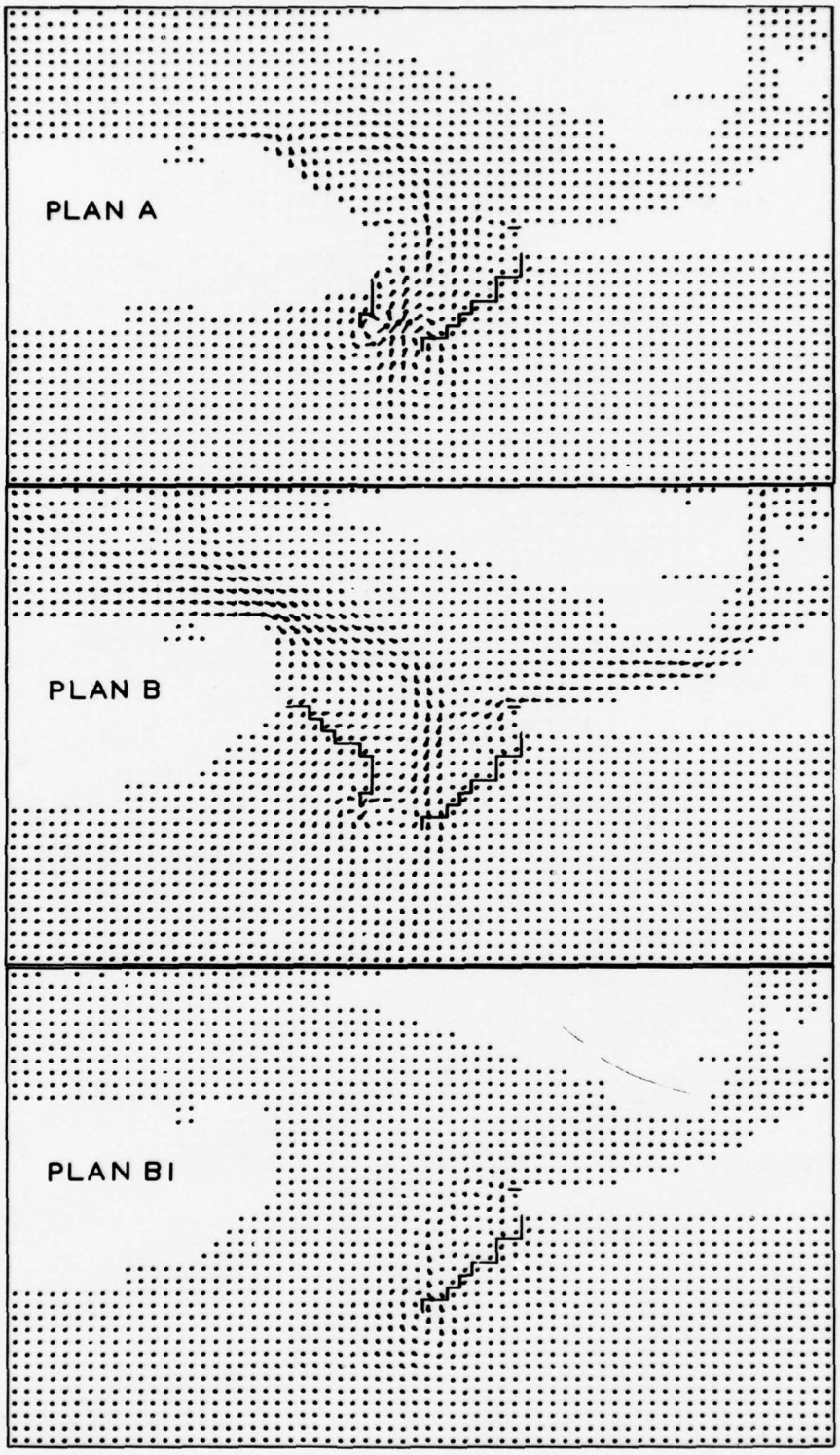

Figure 74. Comparison of unit flow difference patterns for Great Egg Inlet Plans A, B, and B1 at 0900 EST

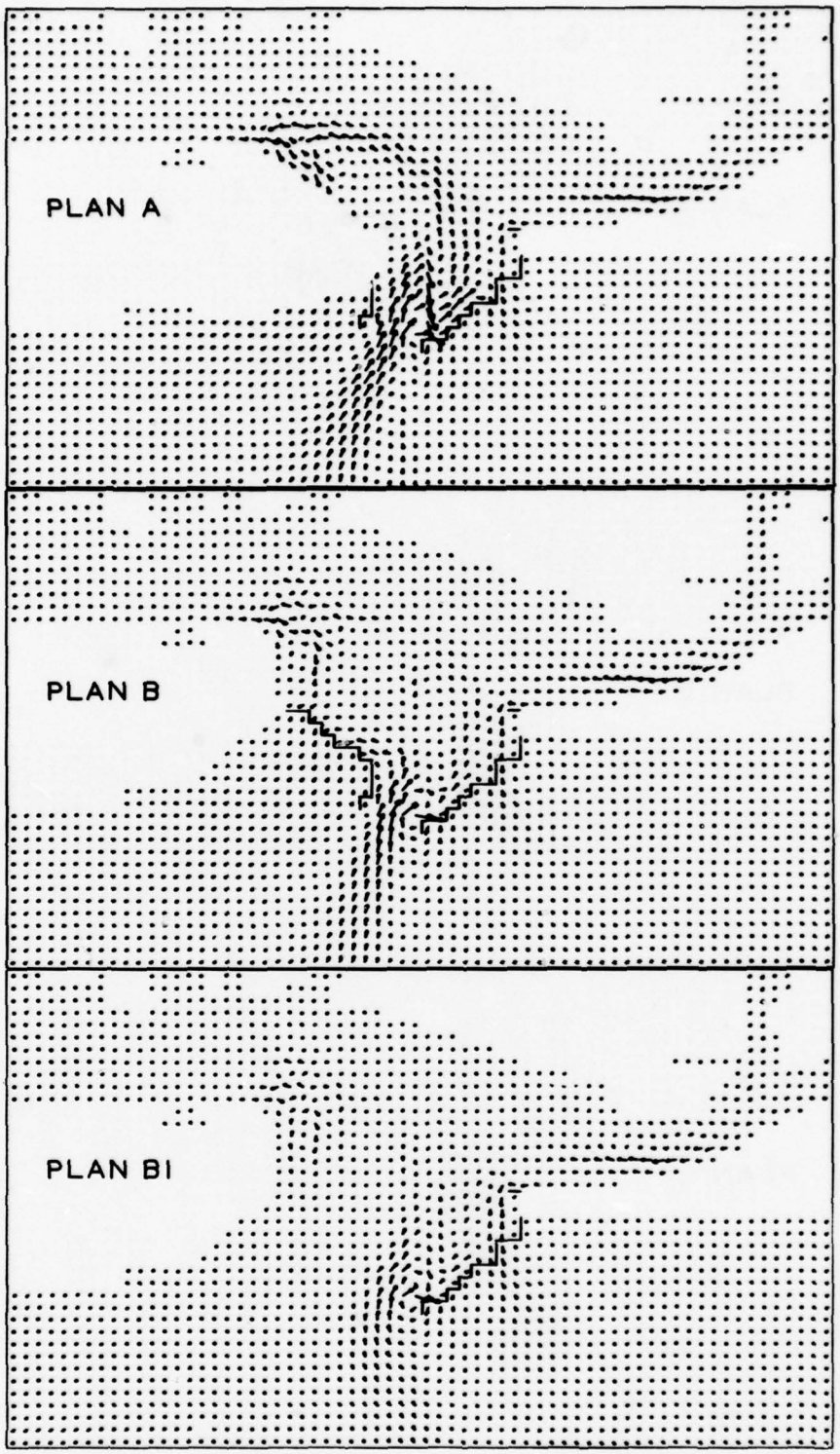

Figure 75. Comparison of unit flow difference patterns for Great Egg Inlet Plans A, B, and B1 at 1100 EST

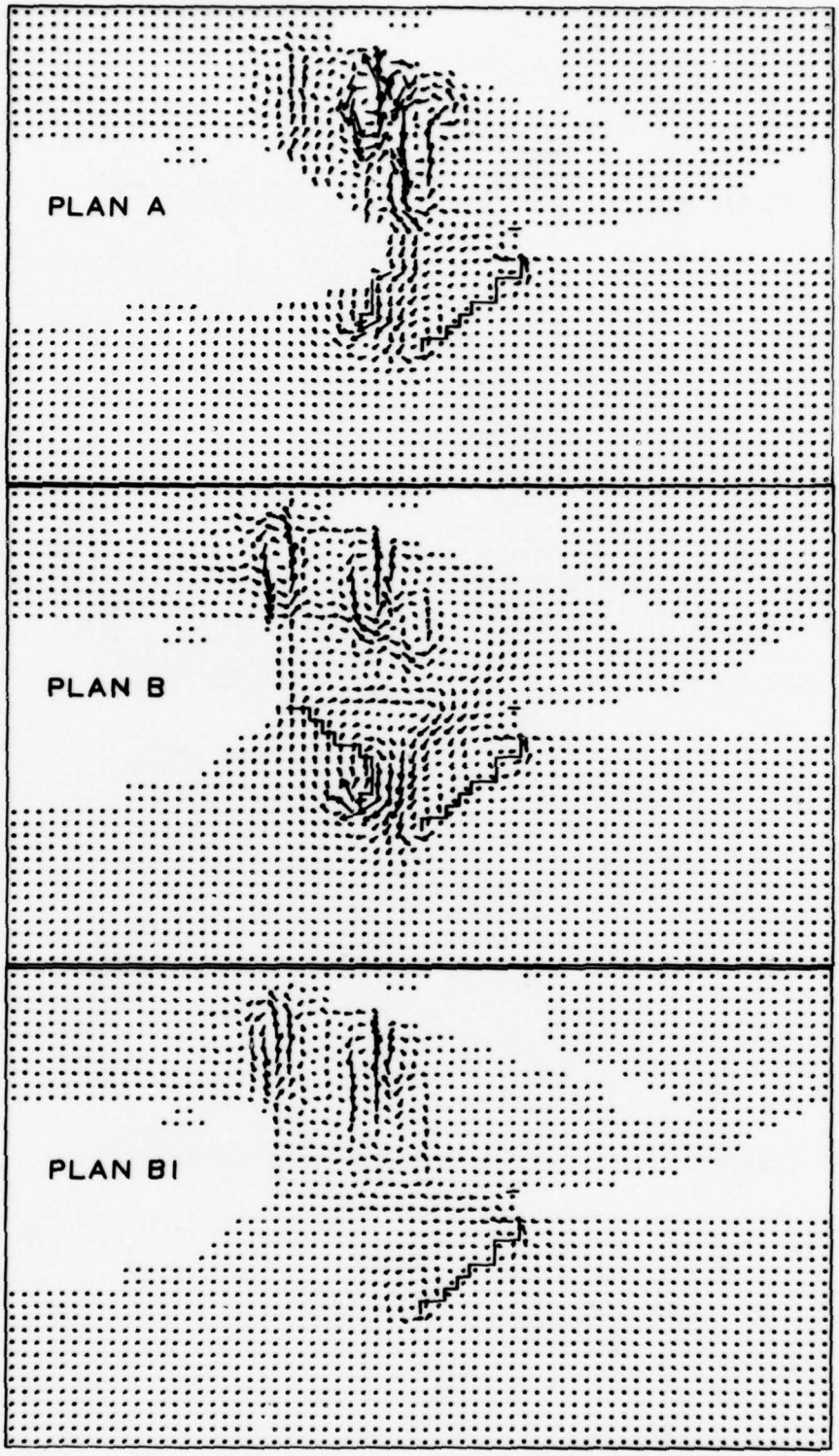

Figure 76. Comparison of unit flow difference patterns for Great Egg Inlet Plans A, B, and B1 at 1900 EST

PART VIII: CONCLUSIONS

74. Both Great Egg Harbor and Corson Inlet models were verified to reproduce satisfactorily the hydrodynamic response of the inlet system to specified astronomical tides. The verification procedure substantiates the model's ability to reliably predict the effect of the proposed modifications to each inlet on tidal elevations, current velocities, and circulation within the study area. Although numerical difficulties occurred in the back bay area of Corson Inlet during a portion of the tidal cycle, the flow patterns and hydrodynamic data obtained in the local area of the modifications are valid.

75. The Corson Inlet model results indicate that relative to base conditions, both plans caused greater ebb flow rates in the entrance channel while maintaining the same flood flow rates.

76. Greater success was met in the simulation of Great Egg Harbor Inlet. The concentration of ebb flow toward the upcoast deposition basin and structure suggests a potential problem with the proposed plans. A separate test with only the upcoast elements of the proposed improvements installed indicated that the problem was associated with the upcoast modifications together with the natural alignment of the main channel.

77. Now that the models are formulated, the testing of additional plans will require only the necessary changes in the code's input data. Future testing should include an update of the bathymetry data in the back bay areas of GECI. Such testing also should include a parameter study of the weir-deposition basin characteristics once a basic plan is selected. The results presented herein are sufficient for advance planning purposes. Detailed design studies would have to be conducted separately, including a wave refraction analysis to assist in design for final jetty alignment.

78. Results of the comparison application at Masonboro Inlet, North Carolina, demonstrate that the WI model can reliably and economically simulate tidal hydrodynamics of a complicated inlet system. This conclusion is substantiated by successful application of the model to

Great Egg Harbor and Corson Inlets. Statistics on computer run time for the application of the WI model are summarized in Table 5. Success of the Corson Inlet application was limited due to a lack of sufficient bathymetric data in the back bay area to resolve the proper flow communication between some of the interior channels. A few numerical problems did develop in some of the plan applications and various filtering techniques were used to overcome the difficulties.

REFERENCES

1. U. S. Army Engineer District, Philadelphia, "Study of the New Jersey Coastal Inlets and Beaches - Interim Report on Great Egg Harbor Inlet to Stone Harbor," 30 Nov 1966, Philadelphia, Pa.; also presented as House Document No. 91-160.

2. Reid, R. O. and Bodine, B. R., "Numerical Model for Storm Surges in Galveston Bay," Journal, Waterways and Harbors Division, American Society of Civil Engineers, Vol 94, No. WW1, Feb 1968.

3. Masch, F. D., Brandes, R. J., and Reagan, J. D., "Simulation of Hydrodynamics in a Tidal Inlet," Feb 1973, Water Resources Engineers, Inc., Austin, Tex.; Technical Report prepared for U. S. Army Coastal Engineering Research Center, Fort Belvoir, Va.

4. Butler, H. L. and Durham, D. L., "Applications of Numerical Modeling to Coastal Engineering Problems," 1975 Army Numerical Analysis and Computers Conference, St. Louis, Mo., Feb 1975.

5. Leendertse, J. J., "A Water-Quality Simulation Model for Well-Mixed Estuaries and Coastal Seas; Volume I, Principals of Computation," The Rand Corporation, RM-6230-RC, Feb 1970, Santa Monica, Calif.

6. _____, "A Water-Quality Simulation Model for Well-Mixed Estuaries and Coastal Seas; Volume II, Computational Procedures," R-708-NYC, Apr 1971, The Rand Corporation, Santa Monica, Calif.

7. Ahlert, R. C., Harlukowicz, T. J., and Nordstrom, K. F., "Hydrodynamic Surveys of Corson and Great Egg Harbor Inlets," TR 76-1 WRE, 1976, Rutgers University, New Brunswick, N. J.

8. Dronkers, J. J., Tidal Computations in Rivers and Coastal Waters, Wiley, New York, 1964.

9. Leendertse, J. J., "Aspects of a Computational Model for Long-Period Water-Wave Propagation," RM-5294-PR, May 1967, The Rand Corporation, Santa Monica, Calif.

10. Wang, J. D. and Connor, J. J., "Mathematical Modeling of Near Coastal Circulation," TR 200, Apr 1975, R. M. Parsons Laboratory for Water Resources and Hydrodynamics, Massachusetts Institute of Technology, Cambridge, Mass.

11. Vreugdenhil, C. B., "Secondary-Flow Computations," Publication No. 114, Nov 1973, Delft Hydraulics Laboratory, Delft, Netherlands.

12. Deardorff, J. W., "On the Magnitude of the Subgrid Scale Eddy Coefficient," Journal of Computational Physics, Vol 7, No. 1, 1971.

13. Sager, R. A. and Seabergh, W. C., "Physical Model Simulation of the Hydraulics of Masonboro Inlet, North Carolina," GITI Report 15 (in preparation), program of research conducted jointly by U. S. Army Coastal Engineering Research Center, Fort Belvoir, Va., and

U. S. Army Engineer Waterways Experiment Station, CE, Vicksburg, Miss., and published by U. S. Army Engineer Waterways Experiment Station, CE, Vicksburg, Miss.

14. U. S. Department of Commerce, "National Oceanic and Atmospheric Administration - National Ocean Survey Tide Tables 1975 - High and Low Water Predictions - East Coast of North and South America," 1975, U. S. Government Printing Office, Washington, D. C.

15. Otnes, R. K. and Enochson, L., Digital Time Series Analysis, Wiley, New York, 1972.

Table 1

Comparison Statistics for

Masonboro Inlet Application

Grid			
	Dimensions		41 x 57
	Number of water points		1721
	Spatial step size, ft		300
Solution			
		Δt sec	Run Time* min
	RB-Explicit	3	60
	WI-Implicit	90	4

* Based on 18-hour (prototype) simulation on a CDC 7600.

Table 2

Wind Field During Prototype Survey

EST Time	Wind Speed, knots, and Direction 6-9-75	6-10-75	EST Time	Wind Speed, knots, and Direction 6-9-75	6-10-75
0100	E 5	SE 6	1300	N 8	SSE 11
0200	C*	SSE 4	1400	NE 14	SE 8
0300	C	SSE 5	1500	EWE 15	SE 8
0400	C	SSE 4	1600	ENE 11	S 10
0500	W 5	C	1700	EWE 12	S 8
0600	C	C	1800	E 12	SSW 9
0700	WSW 5	E 6	1900	E 13	SSW 10
0800	W 8	E 6	2000	E 10	S 10
0900	WNW 7	ESE 6	2100	SE 9	SSW 9
1000	NW 8	E 8	2200	SE 11	S 9
1100	WNW 10	ESE 8	2300	E 8	S 8
1200	NW 8	SE 10	2400	SE 9	SSW 9

* C = Calm.

Table 3

Model Mean Tide Levels and Discharges at Corson Inlet for 10 June 1975 Between 0730 EST and 2000 EST

Range No.	Mean Tide Level, ft, SLD	Q_{IN}* $ft^3 \times 10^6$	Q_{OUT}* $ft^3 \times 10^6$	Q_{TOTAL}** $ft^3 \times 10^6$
1	0.88	872	616	256
2	0.84	215	166	49
3	0.90	20	22	-2
4	0.96	553	358	195
5	0.95	227	182	45
6	0.91	112	92	20
7	0.91	81	65	16
8	0.92	193	118	75
9	0.90	84	57	27
10	0.89	123	106	17

* For ranges 1, 2, and 3, Q_{IN} and Q_{OUT} refer to flow into and out of the back bay system; for all other ranges, they refer to flow under flood and ebb stage.

** A negative sign for Q_{TOTAL} indicates net flow out of the back bay system or a net ebb flow.

Table 4

Model Mean Tide Levels and Discharges at Great Egg Harbor Inlet (Base and Plan Conditions)

for 6-9-75 Between 0700 and 1930 Hours EST

Range No.	Mean Tide Level, ft, SLD				Q_{IN}, $ft^3 \times 10^6$*				Q_{OUT}, $ft^3 \times 10^6$*				Q_{TOTAL}, $ft^3 \times 10^6$**			
	Base	A	B	B1	Base	A	B	B1	Base	A	B	B1	Base	A	B	B1
1	1.360	1.364	1.305	1.398	3819	3489	3533	3816	2774	2443	2515	2593	1045	1046	1018	1223
2	1.621	1.602	1.562	1.614	505	544	487	502	0.3	0.1	1.5	0.7	505	544	485	501
3	1.251	1.250	1.206	1.251	435	260	269	388	1579	1395	1303	1498	-1143	-1153	-1034	-1110
4	1.120	1.118	1.067	1.117	0.2	0	0	0.4	195	182	172	175	-195	-182	-172	-175
5	1.277	1.276	1.226	1.276	48	72	69	51	62	55	38	29	-14	17	31	22
6	1.282	1.297	1.229	1.279	16	32	22	14	85	109	57	62	-69	-77	-35	-48
7	1.456	1.452	1.401	1.455	283	218	203	243	143	51	47	132	140	167	156	111
8	1.323	1.332	1.274	1.318	2646	2441	2391	2591	1682	1431	1501	1615	964	1010	890	976
9	1.553	1.500	1.413	1.422	186	169	154	176	159	146	140	119	27	23	14	57
10	1.399	1.404	1.347	1.405	237	150	140	222	363	284	284	319	-126	-134	-144	-97
11	1.362	1.364	1.297	1.359	445	443	439	461	374	343	305	304	71	100	134	157
12	1.281	1.270	1.223	1.275	273	227	203	248	68	38	42	55	205	189	161	193
13	1.322	1.323	1.268	1.310	769	731	737	776	684	575	599	653	85	156	138	123
14	2.788	2.787	2.745	2.787	320	244	217	252	18	23	15	15	302	221	202	237

* For ranges 1-7, Q_{IN} and Q_{OUT} refer to flow into and out of the back bay system; for all other ranges, they refer to flow under flood and ebb stage.

** A negative sign for Q_{TOTAL} indicates a net flow out of the back bay system or net ebb flow.

Table 5

Computer Run Times for Tidal Simulation Code

Inlet	Grid Dimensions	Spatial Step, ft	Runtime/Δt sec*	Runtime/18PH min**
Masonboro	41 × 57	300	0.167	4.0
Corson	110 × 91	300	0.89	21.4
Great Egg	152 × 106	300	1.43	34.2

* All computer runs were executed on the LASL CDC 7600 using the CROS operating system.

** Run time per 18-hour prototype simulation.

APPENDIX A: FORMULATION OF THE WI MODEL

1. To form the finite difference approximations of the differential equations given in Part II of main text, a space-staggered scheme is used wherein flows and water levels are defined at different locations in the grid (Figure A1). The technique used is defined as a

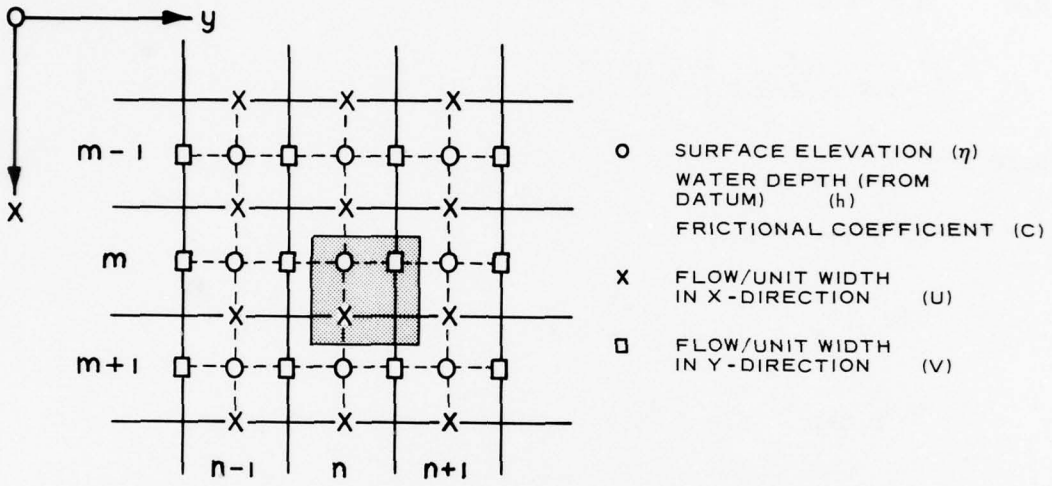

Figure A1. Space-staggered scheme

multioperational, alternating direction implicit method. The first operation (1/2 cycle) computes η and U implicitly, advancing the time from $k\Delta t$ to $(k + 1/2)\Delta t$. The following equations for the first 1/2 cycle are applied columnwise (along lines parallel to the x-axis):*

$$U^{k+\frac{1}{2}}_{n,m+\frac{1}{2}} = U^{k-\frac{1}{2}}_{n,m+\frac{1}{2}} + \Delta t \left[f \overline{V} - \frac{U^{k+\frac{1}{2}}_{n,m+\frac{1}{2}} \left(U^{k-\frac{1}{2}}_{n,m+3/2} - U^{k-\frac{1}{2}}_{n,m-\frac{1}{2}} \right)}{2\Delta S d^*} \right.$$

$$\left. - \frac{\overline{V}}{2\Delta S d^*} \left(U^{k-\frac{1}{2}}_{n+1,m+\frac{1}{2}} - U^{k-\frac{1}{2}}_{n-1,m+\frac{1}{2}} \right) - g d^* \left\{ \left(\eta^{k+\frac{1}{2}}_{n,m+1} \right. \right. \right.$$

---

* Additional notation used within this appendix is defined in the text and is not included in the list of general notations given in Appendix D.

$$- \eta^{k+\frac{1}{2}}_{n,m} + \eta^{k-\frac{1}{2}}_{n,m+1} - \eta^{k-\frac{1}{2}}_{n,m})/2\Delta S + \frac{U^{k+\frac{1}{2}}_{n,m+\frac{1}{2}} + U^{k-\frac{1}{2}}_{n,m+\frac{1}{2}}}{2(d^*)^3 \overline{C}^2} \cdot$$

$$\cdot ((U^{k-\frac{1}{2}}_{n,m+\frac{1}{2}})^2 + \overline{V}^2)^{\frac{1}{2}}\} + F^k_x \Big] \qquad \text{(A1)}$$

$$\eta^{k+\frac{1}{2}}_{n,m} = \eta^k_{n,m} - \frac{\Delta t}{2\Delta S} \Big[U^{k+\frac{1}{2}}_{n,m+\frac{1}{2}} - U^{k+\frac{1}{2}}_{n,m-\frac{1}{2}} + V^k_{n+\frac{1}{2},m} - V^k_{n-\frac{1}{2},m} \Big] + \frac{\Delta t}{2} \xi^k_{n,m} \qquad \text{(A2)}$$

where

$$\overline{C} = \tfrac{1}{2}(C^k_{n,m+1} + C^k_{n,m})$$

$$\overline{V} = \tfrac{1}{4}(V^k_{n-\frac{1}{2},m} + V^k_{n+\frac{1}{2},m} + V^k_{n-\frac{1}{2},m+1} + V^k_{n+\frac{1}{2},m+1})$$

$$d^* = \tfrac{1}{2}(\eta^k_{n,m+1} + \eta^k_{n,m} - h_{n,m+1} - h_{n,m})$$

Gathering terms to be computed along line n at time level $(k + 1/2)\Delta t$, Equations A1 and A2 can be written as

$$-a_m \eta^{k+\frac{1}{2}}_{n,m} + \overline{a}_{m+\frac{1}{2}} U^{k+\frac{1}{2}}_{n,m+\frac{1}{2}} + a_{m+1} \eta^{k+\frac{1}{2}}_{n,m+1} = B_{m+\frac{1}{2}} \qquad \text{(A3)}$$

$$-a_{m-\frac{1}{2}} U^{k+\frac{1}{2}}_{n,m-\frac{1}{2}} + \eta^{k+\frac{1}{2}}_{n,m} + a_{m+\frac{1}{2}} U^{k+\frac{1}{2}}_{n,m+\frac{1}{2}} = A_m$$

where

$$A_m = \eta^k_{n,m} - \frac{\Delta t}{2\Delta s} \Big[V^k_{n+\frac{1}{2},m} - V^k_{n-\frac{1}{2},m} \Big] + \frac{\Delta t}{2} \xi^k_{n,m}$$

$$B_{m+\frac{1}{2}} = U^{k-\frac{1}{2}}_{n,m+\frac{1}{2}} + \Delta t \Big[\{ f - \frac{1}{2\Delta S d^*} (U^{k-\frac{1}{2}}_{n+1,m+\frac{1}{2}} - U^{k-\frac{1}{2}}_{n-1,m+\frac{1}{2}}) \} \overline{V}$$

$$- \frac{g d^*}{2\Delta S} (\eta^{k-\frac{1}{2}}_{n,m+1} - \eta^{k-\frac{1}{2}}_{n,m}) + (F_x)^k_{n,m}$$

$$- \frac{g\, U^{k-\frac{1}{2}}_{n,m+\frac{1}{2}}}{2\bar{C}^2 (d^*)^2} \left\{ (U^{k-\frac{1}{2}}_{n,m+\frac{1}{2}})^2 + \bar{V}^2 \right\}^{\frac{1}{2}} \Bigg]$$

The coefficients are defined as follows:

$$a_{m-\frac{1}{2}} = a_{m+\frac{1}{2}} = \frac{\Delta t}{2\Delta S}$$

$$a_m = a_{m+1} = \frac{g\Delta t d^*}{2\Delta S}$$

$$\bar{a}_{m+\frac{1}{2}} = 1 + \frac{\Delta t}{2\Delta S d^*} \left(U^{k-\frac{1}{2}}_{n,m+3/2} - U^{k-\frac{1}{2}}_{n,m-\frac{1}{2}} \right)$$

$$+ \frac{g\Delta t}{2\bar{C}^2 (d^*)^2} \left[(U^{k-\frac{1}{2}}_{n,m+\frac{1}{2}})^2 + \bar{V}^2 \right]^{\frac{1}{2}}$$

Assuming that $\eta_M^{k+\frac{1}{2}}$ is a given water level at the lower boundary and $U^{k+\frac{1}{2}}_{L+\frac{1}{2}}$ is a given flow at the upper boundary, the matrix form of the equations for line n can be written as follows:

$$\begin{bmatrix} \bar{a}_{M+1/2} & a_{M+1} & 0 & 0 & \cdots & 0 \\ -a_{M+1/2} & 1 & a_{M+3/2} & 0 & \cdots & 0 \\ 0 & -a_{M+1} & \bar{a}_{M+3/2} & a_{M+2} & \cdots & 0 \\ \bullet & \bullet & \bullet & \bullet & \cdots & \cdot \\ \bullet & \bullet & \bullet & \bullet & \cdots & \cdot \\ \bullet & \bullet & \bullet & \bullet & \cdots & \cdot \\ 0 & 0 & 0 & \cdots & -a_{L-1/2} & 1 \end{bmatrix} \begin{bmatrix} U_{M+1/2} \\ \eta_{M+1} \\ U_{M+3/2} \\ \bullet \\ \bullet \\ \bullet \\ \eta_L \end{bmatrix}^{k+1/2} = \begin{bmatrix} \hat{B}_{M+1/2} \\ A_{M+1} \\ B_{M+3/2} \\ \bullet \\ \bullet \\ \bullet \\ \hat{A}_L \end{bmatrix}^k$$

2. The system of equations obtained above is noted to be tridiagonal and can be solved with a minimum number of operations by defining the process of elimination as a set of recursive formulas. Starting with the first equation

$$U_{m+\frac{1}{2}}^{k+\frac{1}{2}} = -R_m \eta_{m+1}^{k+\frac{1}{2}} + S_m \tag{A5}$$

where

$$R_m = \frac{a_{m+1}}{\bar{a}_{m+\frac{1}{2}}} \; ; \; S_m = \frac{\hat{B}_{m+\frac{1}{2}}}{\bar{a}_{m+\frac{1}{2}}}$$

and

$$\hat{B}_{m+\frac{1}{2}} = B_{m+\frac{1}{2}} + a_m \eta_M^{k+\frac{1}{2}}$$

Substitution of Equation A5 into the second equation gives

$$-a_{m+\frac{1}{2}} \left[-R_m \eta_{m+1}^{k+\frac{1}{2}} + S_m \right] + \eta_{m+1}^{k+\frac{1}{2}}$$

$$+ a_{m+3/2} U_{m+3/2}^{k+\frac{1}{2}} = A_{m+1}$$

or

$$\eta_{m+1}^{k+\frac{1}{2}} = -P_{m+1} U_{m+3/2}^{k+\frac{1}{2}} + Q_{m+1} \tag{A6}$$

where

$$P_{m+1} = \frac{a_{m+3/2}}{1+a_{m+\frac{1}{2}} R_m} \; ; \; Q_{m+1} = \frac{A_{m+1} + a_{m+\frac{1}{2}} S_m}{1+a_{m+\frac{1}{2}} R_m}$$

Again, the flow rate can be expressed as a function of the next water level:

$$U_{m+3/2}^{k+\frac{1}{2}} = -R_{m+1}\ \eta_{m+2} + S_{m+1} \tag{A7}$$

where

$$R_{m+1} = \frac{a_{m+2}}{\bar{a}_{m+3/2} + a_{m+1} R_{m+1}} \quad ; S_{m+1} = \frac{B_{m+3/2} + a_{m+1} Q_{m+1}}{\bar{a}_{m+3/2} + a_{m+1} R_{m+1}}$$

In general, the recursion formulas can be written as:

$$\eta_m^{k+\frac{1}{2}} = -P_m\ U_{m+\frac{1}{2}}^{k+\frac{1}{2}} + Q_m \tag{A8}$$

$$U_{m-\frac{1}{2}}^{k+\frac{1}{2}} = -R_{m-1}\ \eta_m^{k+\frac{1}{2}} + S_{m-1} \tag{A9}$$

where

$$T1 = 1 + a_{m-\frac{1}{2}} R_{m-1} \qquad T2 = \bar{a}_{m+\frac{1}{2}} + a_m P_m$$

$$P_m = \frac{a_{m+\frac{1}{2}}}{T1} \qquad Q_m = \frac{A_m + a_{m-\frac{1}{2}} S_{m-1}}{T1}$$

$$R_m = \frac{a_{m+1}}{T2} \qquad S_m = \frac{B_{m+\frac{1}{2}} + a_m Q_m}{T2}$$

3. In the FORTRAN code, fractional subscripts are not permitted. For use in the program a new index system is adopted, whereby water levels, flows, etc., appearing in the shaded area of Figure A1 have the same coordinate index (N,M). Using this notation, the expanded form of the recursion formulas for the first 1/2 cycle can be expressed as:

Coefficients

$$P_M = \frac{\tau}{\Delta S} / \left(1 + \frac{\tau}{\Delta S} R_{M-1}\right) \tag{A10}$$

$$Q_M = \left(A_M + \frac{\tau}{\Delta S} S_{M-1}\right) / \left(1 + \frac{\tau}{\Delta S} R_{M-1}\right) \tag{A11}$$

$$D1 = 1 + \frac{\tau}{d^*\Delta S}\left(U^{k-\frac{1}{2}}_{N,M+1} - U^{k-\frac{1}{2}}_{N,M-1}\right) + \frac{4g\tau}{\left(d^*\left(C_{N,M+1} + C_{N,M}\right)\right)^2} \cdot$$

$$\cdot \left(\left(U^{k-\frac{1}{2}}_{N,M}\right)^2 + \overline{V}^2\right)^{\frac{1}{2}} + \frac{g\tau}{\Delta S} d^* P_M \tag{A12}$$

$$R_M = \frac{gd^*\tau}{\Delta S} / D1 \tag{A13}$$

$$S_M = \left(B_M + \frac{g\tau}{\Delta S} d^* Q_M\right) / D1 \tag{A14}$$

where

$$A_M = \eta^k_{N,M} - \frac{\tau}{\Delta S}\left(V^k_{N,M} - V^k_{N-1,M}\right) + \tau\xi^k_{N,M} \tag{A15}$$

$$B_M = U^{k-\frac{1}{2}}_{N,M} + \tau\{\overline{V}\left[2f - \frac{1}{d^*\Delta S}\left(U^{k-\frac{1}{2}}_{N+1,M} - U^{k-\frac{1}{2}}_{N-1,M}\right)\right]$$

$$- \frac{gd^*}{\Delta S}\left(\eta^{k-\frac{1}{2}}_{N,M+1} - \eta^{k-\frac{1}{2}}_{N,M}\right) + 2\left(F_x\right)^k_{N,M}$$

$$- \frac{4g\, U^{k-\frac{1}{2}}_{N,M}}{\left(d^*\left(C_{N,M} + C_{N,M+1}\right)\right)^2}\left[\left(U^{k-\frac{1}{2}}_{N,M}\right)^2 + \overline{V}^2\right]^{\frac{1}{2}}\} \tag{A16}$$

$$d^* = \tfrac{1}{2}\left(\eta^k_{N,M+1} + \eta^k_{N,M} - h_{N,M+1} - h_{N,M}\right)$$

$$\overline{V} = \tfrac{1}{4}\left(V^k_{N-1,M} + V^k_{N,M} + V^k_{N-1,M+1} + V^k_{N,M+1}\right)$$

$$\tau = \frac{\Delta t}{2}$$

Solution

$$\eta_{N,M}^{k+\frac{1}{2}} = -P_M \, U_{N,M}^{k+\frac{1}{2}} + Q_M \tag{A17}$$

$$U_{N,M-1}^{k+\frac{1}{2}} = -R_{M-1} \, \eta_{N,M}^{k+\frac{1}{2}} + S_{M-1} \tag{A18}$$

The recursion coefficients, P , Q , R , and S , can be computed in succession between boundaries on line N . Depending upon the types of boundary conditions that are applied, various approximations of these coefficients are required. Having calculated the set of coefficients, the solution equation can be solved for all surface elevations and flows in descending order.

4. The second operation (½ cycle) computes η and V implicitly, advancing the time from $(k+\frac{1}{2})\Delta t$ to $(k+1)\Delta t$. The development of the recursion formulas for this ½ cycle is very similar to that just described. The equations for the second ½ cycle, applied row-wise along a line m , are:

$$V_{n+\frac{1}{2},m}^{k+1} = V_{n+\frac{1}{2},m}^{k} + \Delta t \left[-f \, \overline{U}^{k+\frac{1}{2}} - \frac{\overline{U}^{k+\frac{1}{2}}}{2\Delta S \hat{d}} \left(V_{n+\frac{1}{2},m+1}^{k} - V_{n+\frac{1}{2},m-1}^{k} \right) \right.$$

$$- \frac{V_{n+\frac{1}{2},m}^{k+1}}{2\Delta S \hat{d}} \left(V_{n+3/2,m}^{k} - V_{n-1/2,m}^{k} \right) - g\hat{d} \left\{ \frac{1}{2\Delta S} \left(\eta_{n+1,m}^{k+1} - \eta_{n,m}^{k+1} \right. \right.$$

$$\left. + \eta_{n+1,m}^{k} - \eta_{n,m}^{k} \right) + \frac{V_{n+\frac{1}{2},m}^{k+1} + V_{n+\frac{1}{2},m}^{k}}{2\hat{d}^3 \, \overline{C}^2} \cdot$$

$$\left. \left. \cdot \left[\overline{U}^2 + \left(V_{n+\frac{1}{2},m}^{k} \right)^2 \right]^{\frac{1}{2}} \right\} + F_y^{k+\frac{1}{2}} \right] \tag{A19}$$

$$\eta^{k+1}_{n,m} = \eta^{k+\frac{1}{2}}_{n,m} - \frac{\Delta t}{2\Delta S}\left[U^{k+\frac{1}{2}}_{n,m+\frac{1}{2}} - U^{k+\frac{1}{2}}_{n,m-\frac{1}{2}} + V^{k+1}_{n+\frac{1}{2},m} - V^{k+1}_{n-\frac{1}{2},m}\right] + \frac{\Delta t}{2}\,\xi^{k+\frac{1}{2}}_{n,m} \qquad \text{(A20)}$$

where

$$\overline{C} = \tfrac{1}{2}(C^{k+\frac{1}{2}}_{n+1,m} + C^{k+\frac{1}{2}}_{n,m})$$

$$\overline{U} = \tfrac{1}{4}(U^{k+\frac{1}{2}}_{n+1,m+\frac{1}{2}} + U^{k+\frac{1}{2}}_{n+1,m-\frac{1}{2}} + U^{k+\frac{1}{2}}_{n,m-\frac{1}{2}} + U^{k+\frac{1}{2}}_{n,m+\frac{1}{2}})$$

$$\hat{d} = \tfrac{1}{2}(\eta^{k+\frac{1}{2}}_{n+1,m} + \eta^{k+\frac{1}{2}}_{n,m} - h_{n+1,m} - h_{n,m})$$

5. Using the same notation as that for Equations A10-A18, the recursion formulas for the second ½ cycle can be written in expanded form as:

Coefficients

$$P_N = \frac{\tau}{\Delta S} \,/\, \left(1 + \frac{\tau}{\Delta S} R_{N-1}\right) \qquad \text{(A21)}$$

$$Q_N = \left(A_N + \frac{\tau}{\Delta S} S_{N-1}\right) \,/\, \left(1 + \frac{\tau}{\Delta S} R_{N-1}\right) \qquad \text{(A22)}$$

$$D2 = 1 + \frac{\tau}{\hat{d}\Delta S}\left(V^k_{N+1,M} - V^k_{N-1,M}\right) + \frac{4g\tau}{\left(\hat{d}\left(C_{N+1,M} + C_{N,M}\right)\right)^2} \cdot$$

$$\cdot \left[\overline{U}^2 + \left(V^k_{N,M}\right)^2\right]^{\frac{1}{2}} + \frac{g\tau\hat{d}}{\Delta S} P_N \qquad \text{(A23)}$$

$$R_N = \frac{g\tau\hat{d}}{\Delta S} \,/\, D2 \qquad \text{(A24)}$$

$$S_N = \left(B_N + \frac{g\tau\hat{d}}{\Delta S} Q_N\right) \,/\, D2 \qquad \text{(A25)}$$

where

$$A_N = \eta^{k+\frac{1}{2}}_{N,M} - \frac{\tau}{\Delta S}\left(U^{k+\frac{1}{2}}_{N,M} - U^{k+\frac{1}{2}}_{N,M-1}\right) + \tau\,\xi^{k+\frac{1}{2}}_{N,M} \qquad \text{(A26)}$$

$$B_N = V^k_{N,M} - \tau\{\bar{U}\left[2f + \frac{1}{\hat{d}\Delta S}\,(V^k_{N,M+1} - V^k_{N,M-1})\right]$$

$$+ \frac{g\hat{d}}{\Delta S}\,(\eta^k_{N+1,M} - \eta^k_{N,M}) - 2(F_y)^{k+\frac{1}{2}}_{N,M}$$

$$+ \frac{4g\,V^k_{N,M}}{(\hat{d}(C_{N+1,M} + C_{N,M}))^2}\left[\bar{U}^2 + (V^k_{N,M})^2\right]^{\frac{1}{2}}\} \qquad \text{(A27)}$$

$$\hat{d} = \tfrac{1}{2}(\eta^{k+\frac{1}{2}}_{N+1,M} + \eta^{k+\frac{1}{2}}_{N,M} - h_{N+1,M} - h_{N,M})$$

$$\bar{U} = \tfrac{1}{4}(U^{k+\frac{1}{2}}_{N+1,M} + U^{k+\frac{1}{2}}_{N+1,M-1} + U^{k+\frac{1}{2}}_{N,M-1} + U^{k+\frac{1}{2}}_{N,M})$$

Solution

$$\eta^{k+1}_{N,M} = -P_N\,V^{k+1}_{N,M} + Q_N \qquad \text{(A28)}$$

$$V^{k+1}_{N-1,M} = -R_{N-1}\,\eta^{k+1}_{N,M} + S_{N-1} \qquad \text{(A29)}$$

APPENDIX B: IMPLEMENTATION OF BOUNDARY CONDITIONS FOR THE WI MODEL

1. Boundary conditions used in the WI model include the following types: open, closed, barrier, and moving boundaries. To implement these conditions, approximations to the recursion formulas presented in Appendix A are necessary. Computations are made along segments of a grid line with boundary conditions defined at both ends of the line segment. The term "lower bound" is used to denote that end of the computational line segment which corresponds to the smaller spatial index value. The higher indexed line segment end is referred to as the upper bound.

Closed Boundaries

2. In the approximation of an impermeable boundary, it is assumed that the flow normal to the boundary is zero. This forces the assumption that the coastline must pass along cell faces where flows are defined. At a lower boundary, I, a closed condition is computed by setting the recursion coefficients, R and S, to zero, namely,

$$R_I = S_I = 0$$

At an upper boundary, I, closure is accomplished by setting

$$U_I = 0 \quad \text{or} \quad V_I = 0$$

before computing the set of solution equations.

Open Boundaries

3. At open boundaries, water levels are given as functions of time (in tabular form), thus forcing these boundaries to pass through the center of the cells (where the water level, $d = \eta - h$, is defined). To implement an open condition at a lower bound, for a boundary parallel

to the y-axis at line N and row M, the following approximations are made to the recursion coefficients:

$$P_M = 0$$

$$Q_M = \eta_{N,M}^{k+\frac{1}{2}} + \xi_{N,M}^{k}$$

$$\left(\frac{\partial U}{\partial X}\right)_M^{k-\frac{1}{2}} = 0$$

Using these approximations, R_M and S_M are defined accordingly. Note that the computation of the advective term would require values of U outside the computational field. This problem is solved by using a linear approximation of the differential equation in such a case. The treatment of lower open boundaries parallel to the x-axis is similar.

4. At an upper open boundary parallel to the y-axis at (N,M), the normal flow rate at the first interior cell is approximated and written as

$$U_{N,M-1}^{k+\frac{1}{2}} = R_{M-1}\,\eta_{N,M}^{k+\frac{1}{2}} + S_{M-1} \qquad \text{(B1)}$$

where R and S include the approximation

$$\left(\frac{\partial U}{\partial X}\right)_M^{k+\frac{1}{2}} = 0$$

The treatment of upper open boundaries parallel to the x-axis is similar.

Barriers

5. Exposed barriers interior to the system are impermeable boundaries and are treated in the same manner as that indicated for closed boundaries.

6. Submerged barriers may be approximated in two ways: A Chezy formulation or weir formulation. The weir formulation is similar to that used by Reid and Bodine.[2] The flow over a submerged barrier can

be taken as that for a submerged weir, namely,

$$Q_N = \pm C_s D_b (g|H_1 - H_2|)^{\frac{1}{2}} \tag{B2}$$

where Q_N is the flow normal to the barrier;* D_b is the depth of water over the crest of the barrier; H_1 and H_2 are the water levels on the two sides of the barrier (both of which exceed the barrier crest elevation, Z_b); and C_s is an appropriate nondimensional discharge coefficient. In the weir formula, D_b is taken as

$$D_b = \tfrac{1}{2}(H_1 + H_2) - Z_b \tag{B3}$$

and the sign is such that the flow is directed toward the low-head side of the barrier. In the computational scheme, the flow across a submerged barrier is not specified directly; instead, a term incorporating the effect of weir control is introduced into the momentum difference equation. If the barrier is broad and parallel to the y-axis then $Q_N^2 \simeq U^2$. Noting that

$$gd\,\frac{|H_2 - H_1|}{\Delta x} = \frac{d|U|U}{\Delta S (C_s D_b)^2} \tag{B4}$$

from inspection of B3, the frictional effect in the difference equation is replaced by the right-hand side of B4. The implementation of this scheme is accomplished by substituting

$$\frac{\tau d^*}{\Delta S}\,\frac{|U_{N,M}^{k-\frac{1}{2}}|}{(C_s D_b)^2}$$

for the frictional term in D1 (see Equation A12).

7. The Chezy formulation is accomplished by defining a special coefficient at the barrier face. When the appropriate momentum equation is applied at the designated barrier cell, a special value for the

---

* Additional notation used within this appendix is defined in the text and is not included in the list of general notations given in Appendix D.

frictional coefficient ($C = C_W$) is used. In this scheme, C_W is taken as a function of the water depth over the barrier crest.

8. Overtopping barriers are taken as those which can dynamically change from a totally exposed barrier to a submerged barrier and vice versa. Due to the larger time step used in the implicit scheme, the short duration of overtopping is not simulated. Flags are set within the code to change the type of computation at the barrier face when the water level on either side of the barrier face reaches a designated height.

Moving Boundaries

9. Moving boundaries allowed by the code are used to simulate a flooding coastline. At the beginning of a simulation run, a small amount of water (ε_d) is placed on areas which are dry initially, but designated as possible flood cells. When the water level at a cell, adjacent to a "dry" flood cell, is rising and reaches a height greater than ($h + \varepsilon_d$), the closed boundary condition defined at the interface is removed and the appropriate flow quantity is computed. For a cell to dry, the reverse process is performed. A cell will "dry up" if the flows through all four cell faces are zero. It is assumed that when a cell dries, a thin level of water (of height ε_d) is allowed to remain on the cell.

APPENDIX C: METHODS OF ELIMINATING NONLINEAR INSTABILITIES

1. Due to computational considerations, the advective terms are not approximated completely by centered differences in time. Complete centered differences are preferable for accuracy, but the computational effort would be excessive. Thus, a lower order approximation is taken, whereby the spatial derivatives in the advective terms are evaluated at an earlier time level. As discussed in PART III of this report, oscillations may develop due to these lower order approximations. Thus far, there has been no conclusive theory regarding the physical explanation of these instabilities. In the development of the WI code, two schemes were used to eliminate this problem.

Digital Filtering

2. As mentioned previously, results compiled during the development of the code indicated that the advective terms introduce a high-frequency noise of period $4\Delta t$ in the computation of the surface elevations. The use of digital filtering techniques was suggested by the nature of the problem, namely, the construction of a "low-pass" smoothing filter to damp the higher frequencies. For ease of computation, a second-order recursive filter of the form

$$\eta^{k+\frac{1}{2}} = a\tilde{\eta}^{k+\frac{1}{2}} + b\eta^{k} + c\eta^{k-\frac{1}{2}} \tag{C1}$$

was adopted as discussed in PART III. A parameter study was performed which resulted in selection of values for coefficients a, b, and c,* namely

$$a = 0.6 \ , \ b = 0.3 \ , \ c = 0.1 \tag{C2}$$

---

* Additional notation used within this appendix is defined in the text and is not included in the list of general notations given in Appendix D.

The associated transfer function (reduction factor for tidal amplitude) for this selection is

$$H(f) = \frac{a}{1 - bz^{-1} - cz^{-2}} \tag{C3}$$

where

$$z = e^{j2\pi\Delta tf} \tag{C4}$$

The filter is stable according to the criterion given in Otnes and Enochson;[15] if the denominator of the transfer function is in the form

$$z^2 - h_1 z - h_2 \tag{C5}$$

and the point h_1 , h_2 lies in the triangle shown below the filter is stable.

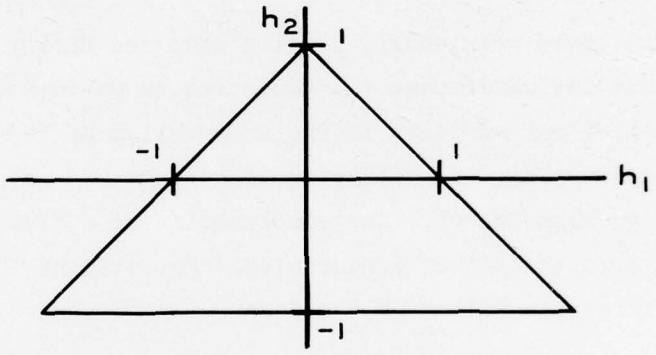

It also can be shown that if r is a real number and

$$\eta^{k+p} = r^p \eta^k \tag{C6}$$

with

$$|r| \leq 1 \ , \tag{C7}$$

the filter is stable.

Since

$$\eta^k - br^{-1}\eta^k - cr^{-2}\eta^k = 0$$

or

$$r^2 - br - c = 0 \qquad \text{(C9)}$$

The conditions relating to the filter defined by the coefficients in Equation C2 are

$$|r| = \left|\frac{.3 \pm \sqrt{.49}}{2}\right| < 1$$

Thus, both conditions are satisfied and the filter is stable.

3. The frequency response of the selected filter is given by the graph

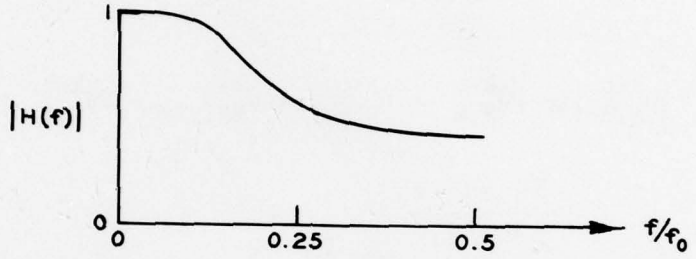

where $f_o = 1/\Delta t$ is the sampling frequency. Since the oscillations are of period $4\Delta t$, and the sampling period is Δt, then the reduction factor at $f/f_o = 1/4\Delta t/1/\Delta t = 0.25$ is 0.526 percent. The effect on the amplitude of the input signal (tide) is given in the above figure for $f/f_o = 0.001$ (corresponding to a 12.5-hour tidal cycle) to be a reduction of 0.037 percent. A similar curve for the phase response indicates an effect of 0.166 percent. Shorter period components of the signal can be introduced by folding the tidal input at 12.5 hours. The percentile effects on amplitude and phase are 0.077 percent and 0.35 percent, respectively. Results obtained by running a linearized system with and without the filter show no discernible differences in surface elevations or flows throughout a 12.5-hour prototype simulation.

Eddy-Viscosity Terms

4. The inclusion of terms to abate instabilities caused by a "secondary flow" phenomenon was discussed in PART III. These terms

are added to the right-hand side of the momentum equations (see PART II, Equations 1 and 2) and may be written as

Equation 1

$$\ldots + \varepsilon \left[\frac{\partial^2 U}{\partial x^2} + \frac{\partial^2 U}{\partial y^2}\right] \tag{C10}$$

Equation 2

$$\ldots + \varepsilon \left[\frac{\partial^2 V}{\partial x^2} + \frac{\partial^2 V}{\partial y^2}\right] \tag{C11}$$

The finite difference approximations for these terms are:

Equation 1

$$\ldots + \frac{\varepsilon}{\Delta S^2}\left[U^{k-\frac{1}{2}}_{N,M+1} - 2U^{k-\frac{1}{2}}_{N,M} + U^{k-\frac{1}{2}}_{N,M-1} + U^{k-\frac{1}{2}}_{N+1,\,M} - 2U^{k-\frac{1}{2}}_{N,M} + U^{k-\frac{1}{2}}_{N-1,M}\right]$$

Equation 2

$$\ldots + \frac{\varepsilon}{\Delta S^2}\left[V^{k}_{N,M+1} - 2V^{k}_{N,M} + V^{k}_{N,M-1} + V^{k}_{N+1,M} - 2V^{k}_{N,M} + V^{k}_{N-1,M}\right]$$

Since such terms involve flows only at earlier time levels, they appear in the computation of B_M or B_N as given in Appendix A. The relation

$$\varepsilon \simeq 6\sqrt{g(U^2 + V^2)}/C \tag{C12}$$

gives an approximation of the value of ε to use in running the code. For the entrance channel area at Great Egg Inlet where instabilities occurred, the following orders of magnitude were noted for the parameters appearing in Equation C12:

$$g \simeq 32.2 \text{ ft/sec}^2$$

$$C^2 \simeq 10^4 \text{ ft/sec}^2 \rightarrow \varepsilon \simeq 5 \text{ ft}^2/\text{sec}$$

$$U,V \simeq 100 \text{ ft}^2 \text{ sec}$$

Computer runs were made varying ε (over a range of 2 to 20), and the results were noticeably affected in both amplitude and phase as ε was increased beyond $\varepsilon = 5$. It is important to choose the smallest value of ε such that the instability problem is cured with minimal effect on the accuracy of the computations.

APPENDIX D: NOTATION

C	Chezy frictional coefficient
d	Total water depth
d_{max}	Maximum water depth at any location and time in the system
f	Coriolis parameter
F_x, F_y	External forcing functions
g	Acceleration due to gravity
h	Land-surface elevation
k	Time increment counter
M,N	Indices denoting spatial increments in the x and y direction
n	Manning's frictional coefficient
n_x, n_y	Averaged Manning's coefficient
t	Time
U,V	Vertically integrated horizontal transport (flow) components
x,y,z	Cartesian coordinates
Δx, Δy	Spatial increment
ΔS	General spatial increment (grid size)
Δt	Time increment
ε	Eddy-viscosity coefficient
η	Water-surface elevation with respect to given datum
ξ	Rainfall minus evaporation

In accordance with letter from DAEN-RDC, DAEN-ASI dated 22 July 1977, Subject: Facsimile Catalog Cards for Laboratory Technical Publications, a facsimile catalog card in Library of Congress MARC format is reproduced below.

Butler, H Lee
Numerical simulation of tidal hydrodynamics, Great Egg Harbor and Corson Inlets, New Jersey / by H. Lee Butler. Vicksburg, Miss. : U. S. Waterways Experiment Station ; Springfield, Va. : available from National Technical Information Service, 1978.
114, [24] p. : ill. ; 27 cm. (Technical report - U. S. Army Engineer Waterways Experiment Station ; H-78-11)
Prepared for U. S. Army Engineer District, Philadelphia, Philadelphia, Pennsylvania.
Appendix E on microfiche in pocket.
References: p. 113-114.
1. Corson Inlet. 2. Erosion. 3. Finite difference method. 4. Great Egg Harbor Inlet. 5. Hydrodynamics. 6. Inlets (Waterways). 7. Mathematical models. 8. Navigation channels. 9. Navigation conditions. 10. Numerical simulation. 11. Tidal hydraulics. 12. Tidal models. I. United States. Army. Corps of Engineers. Philadelphia District. II. Series: United States. Waterways Experiment Station, Vicksburg, Miss. Technical report ; H-78-11.
TA7.W34 no.H-78-11